BRNO UNIVERSITY OF TECHNOLOGY

VYSOKÉ UČENÍ TECHNICKÉ V BRNĚ

CENTRAL EUROPEAN INSTITUTE OF TECHNOLOGY

STŘEDOEVROPSKÝ TECHNOLOGICKÝ INSTITUT VUT

SINGLE-MOLECULE MAGNETS WITH TRIGONAL SYMMETRY OF THE COORDINATION POLYHEDRON: STRUCTURE, MAGNETIC PROPERTIES AND DEPOSITION ON SURFACES

JEDNOMOLEKULÁRNÍ MAGNETY S TRIGONÁLNÍ SYMETRIÍ KOORDINAČNÍHO POLYEDRU: STRUKTURA, MAGNETICKÉ VLASTNOSTI A DEPOZICE NA POVRCHY

DOCTORAL THESIS

DIZERTAČNÍ PRÁCE

AUTHOR   **Mgr. Lubomír Havlíček**

AUTOR PRÁCE

SUPERVISOR   **doc. Dr. Ing. Petr Neugebauer, Ph.D.**

ŠKOLITEL

CO-SUPERVISOR   **Dr. Ing. Ivan Nemec, Ph.D.**

KONZULTANT

BRNO 2022

Abstract

This thesis focusses on synthesis, structure and magnetization study of Single Ion Magnets with trigonal symmetry and their deposition on surfaces. The first part outlines the introduction into State of the art of the Single Molecule magnets. Followed by description of methods used to perform all discussed characterizations and theoretical background of these methods. In the next part are discussed all the obtained results and it is concluded by discussion about the achieved aims of this thesis. The last part of this thesis provides references and author's published results.

Keywords

Single-Molecule Magnets, Coordination chemistry, Organic chemistry, Trigonal symmetry.

Abstrakt

Tato práce se zaměřuje na syntézu, strukturu a magnetické vlastnosti Jedno Iontových Magnetů s trigonální symetrií a jejich depozici na povrchy. První část se zabývá úvodem do tématiky Jedno Molekulových magnetů. Následuje část věnovaná metodám použitým k provedení charakterizací studovaných vzorků, následně je kapitola doplněná o teoretickou část. Dále jsou diskutovány připravené vzorky a následuje diskuze o získaných datech a o dosažení cílů této práce. Závěrečná část obsahuje použitou literaturu a seznam autorových činností v průběhu studia.

Klíčová slova

Jedno-Molekulové Magnety, Koordinační chemie, Organická chemie, Trigonální symetrie

I hereby declare that I have written my doctoral thesis topic on the theme SINGLE-MOLECULE MAGNETS WITH TRIGONAL SYMMETRY OF THE COORDINATION POLYHEDRON: STRUCTURE, MAGNETIC PROPERTIES AND DEPOSITION ON SURFACES independently, under the guidance of the thesis supervisor doc. Dr. Ing. Petr Neugebauer, PhD. and co-supervisor Dr. Ing. Ivan Nemec, PhD., and using literature and other sources of information which are all properly quoted in the thesis and detailed in the list of literature at the end of the thesis.

Contents

List of used abbreviations

SMM – Single Molecule Magnet

SIM – Single Ion Magnet

SCM – Single Chain Magnet

SOC – Spin-Orbit Coupling

EPR – Electron Paramagnetic Resonance

PPMS – Physical Properties Measurement System

SQUID – Superconducting Quantum Interference Device

CASSCF – Complete Active Space Self Consistent Field

DFT – Density Function Theorem

XPS – X-ray Photoelectron Spectroscopy

Raman – Raman Spectroscopy

UV/VIS – Ultra-Violet/Visible Light Spectroscopy

IR/FTIR – Infra-Red/Fourier Transform Infra-Red Spectroscopy

SEM – Scanning Electron Microscopy

AFM – Atomic Force Microscopy

XMCD – X-Ray Magnetic Circular Dichroism

EA – Elemental Analysis

XRPD – X-Ray Powder Diffraction

VSM – Vibrating Sample Measurement

AC – Alternating Current

DC – Direct Current

SCO – Spin Crossover

ZFS – Zero Field Splitting

QTM – Quantum Tunnelling of Magnetization

MPMS – Magnetic Properties Measurement System

TBY – Trigonal Bipyramid

SPY – Square Pyramid

MOTeS – Magneto-Optical and Terahertz Spectroscopy Research Group

1. Introduction

Utilization of magnetic phenomena in devices allowed humanity to explore the Earth during the previous centuries. Since that, this research area enormously expanded and due the practical utilization of magnetism in e.g., information and transportation technologies the society profited from unprecedent level of economic globalization based on quantum properties of the nano-world leading to discovery of new kinds of materials with exciting properties. Most of the modern technology, such as transportation, communication, and data storage, is based on the magnetic materials originating in transition and rare-earth metals or their alloys[1]. Nowadays, technological devices' miniaturization and energy efficiency led scientific focus towards materials that can be sufficiently small while preserving their magnetic properties – single-molecule magnets (SMMs). Such molecules exhibit slow relaxation of magnetization of purely molecular origin and are able to preserve direction of its magnetic dipole from changing its orientation due to presence of intrinsic spin-reversal barrier. Such compound is a coordination compound with transition/inner transition ion as a central atom and with spin larger than ½ and axial magnetic anisotropy. The first SMM, famous complex $[Mn_{12}O_{12}(O_2CCH_3)_{16}(H_2O)_4]\cdot 4H_2O\cdot 2CH_3CO_2H$ (abbreviated as Mn_{12}) was synthesized in 1980[2] and its magnetic properties were published more than decade later in 1993[3]. This discovery opened a new field of research and new possibilities for future technology as the first samples showed magnetic hysteresis – an essential phenomenon for creation of magnetic nano-devices. The size on molecular (nm) scale of the newly discovered compounds suggested a potential for significant miniaturisation or great increase in density (in ideal model scenario the area density can reach up to hundreds of thousands of $Tbit/m^2$ compared to current solid-state drives reaching lower thousands of $Tbit/m^2$) of magnetic entities in possible devices[4]. As well as the first SMM (Mn_{12}) also the other new SMMs were based on manganese coordination compounds, which reached very high number of the central atoms. The first iron based SMM was discovered in 1996[5] (abbreviated as Fe_8) expanded the family of SMM by another element and other transition metals based SMM were sure to follow. This was achieved in 2002[6] by discovery of the first cobalt based SMM (abbreviated as Co_4). Another transition metal SMMs followed (Ni, V, etc.).
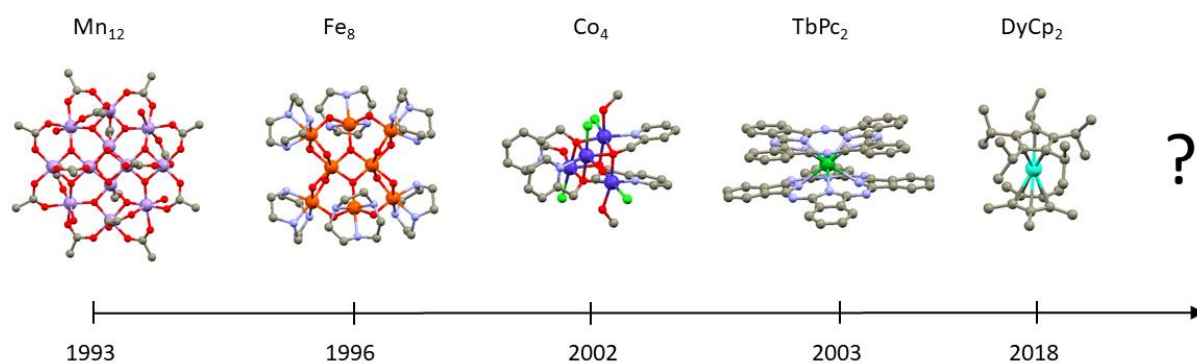
Figure 1: Overview of development of milestones of SMM/SIM. Purple (Co), dark green (Tb), azure (Dy), grey (C), light blue (N), green (Cl), red (O), dark orange (Fe). The hydrogen atoms are omitted for clarity.

These first discovered SMMs unfortunately failed to reach desirable magnetic performance at high temperatures. The change came with the discovery of a system containing one lanthanide centre 2003[7], such system gave foundation to new category of SMMs in only one ion centre called Single Ion Magnets (SIMs) by preparation of terbium double-decker (abbreviated as TbPc$_2$)[8]. Interesting discovery was achieved in 2012 by preparing iron-based SIM and is described in the beginning of section 3.1. This new compound additionally exhibited spin crossover (SCO) phenomenon allowing it to exist in two spin states with the possibility of switching in between them. Such a combination of phenomena promises a great potential for magnetic and optical sensors or for switchable magnetic devices. Next important milestone was set by discovery of two organometallic SIMs containing Dy(III) centre. The first one was published in 2016 and it pushed the blocking temperature up to 60 K. In 2018, this great discovery was followed by report on its derivate with the blocking temperature increased up to 80 K in Dy double-decker (abbreviated as DyCp2) (these milestones are more discussed in the final part of section 3.1), which is above the boiling point of the liquid nitrogen. These results brought the whole research of SMMs closer to application in real life and to forefront of current research with various possible applications as high-density data storage, quantum bits, and molecular spintronics[9,10].

The new challenge for scientists is to create real life devices. To achieve this, it is necessary to have control over the respective molecules. To gain such control, the SIMs have to be deposited on functional surfaces capable e.g. to conduct electric current. This important topic is discussed in the section 3.2 of this thesis. The successful deposition could be a challenging due to a need for balance between rational design of the molecules (ligand field symmetry, capability to attach to the surface or to self-assembly on the surface), their physical properties (solubility, sublimation temperature or thermal stability) and deposition techniques. Moreover, the

5

magnetic properties of deposited SMMs/SIMs can greatly differ from a bulk material as their geometry and intra/intermolecular interactions can be significantly modified upon deposition. Carefully designed organic ligands allow coordination of ion and interactions with the substrate via chemical bonds (e.g. S-Au) or via weaker non-covalent interactions (e.g. π-π) to form self-assembled SIMs as hybrid materials devices. Some of the newly prepared hybrid materials show slow relaxation of magnetization with record blocking temperature of 28 K[11]. This field of study is highly uncharted, and carries a great potential for further discoveries.
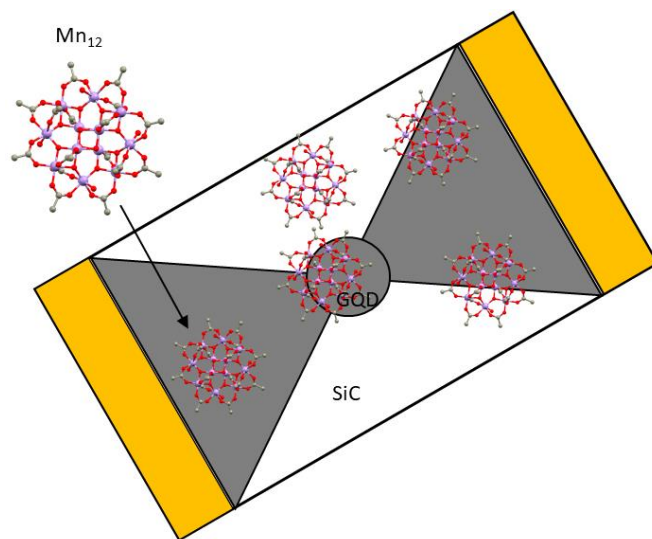

Figure 2: Artistic view of graphene bolometer chip with Quantum Graphene Dot (GQD) and with Mn$_{12}$ molecules deposited on the bolometer.

2. Aims of thesis

Aim of this thesis was to prepare various coordination compounds with trigonal symmetry of their coordination polyhedral, study their crystal structure, investigate their magnetic properties with various techniques (PPMS, SQUID, EPR) and to characterize them as Single Ion Magnets. Selected SIMs with suitable structural and magnetic parameters would be deposited on surfaces such as graphene, gold, silicon or transition metal dichalcogenides. This hybrid materials would be characterized by XPS, Raman spectroscopy, SEM and HF-EPR.

1. The first objective was to prepare coordination compounds with Co(II) and additionally Dy(III). The aim was to synthetize or search for available organic ligands, perform series of chemical reactions and grow high quality single crystals of obtained coordination compounds. Upon design successful synthesis experiments and obtaining crystals this compounds were elementally (XPS, EA), spectroscopically (IR, Raman, UV/VIS) and structurally studied (XRPD, Single crystal X-Ray diffraction).

2. The second objective was to study the magnetic parameters of coordination compounds prepared in Objective 1 and to characterize them as SMMs/SIMs. To complete this objective samples were by VSM in form of powder sample under high magnetic fields and low temperature to obtain information about magnetic susceptibility of prepared samples. VSM was followed by HF-EPR measurements to fine tune the previously gathered magnetic data. These measurements were complemented by theoretical calculations providing complex insight into the studied magnetic properties.

3. The third objective was to deposit selected coordination compounds on various surfaces mainly by thermal deposition using custom-made Sublimation chamber followed by analysis of created hybrid material by SEM, Raman spectroscopy and XPS. The substrates with surfaces were modelled to fit the HF-EPR sample holder so the magnetic properties of such hybrid materials could be studied and compared to bulk materials.

3. State of the Art of Magnetism of Coordination Compounds

This chapter is introduction to the research of molecular magnetism with special attention dedicated to Single Molecule Magnets, which are coordination compounds of the transition or inner transition metals. The chapter aims to briefly introduce history of SMMs and to highlight the most important milestones in this field with major focus on coordination compounds of Dy(III) and Co(II) with trigonal symmetry of ligands or ligand field. This chapter also briefly discuss methodology used for characterization of these compounds. In the end of this chapter the previously reported results on depositions of SMMs on various surfaces (with focus on graphene) are discussed.

3.1 Magnetic Materials

Based on the interaction of the material with magnetic field, two types of magnetic materials can be distinguished – diamagnetic (repulsed from magnetic field) and paramagnetic (attracted by the magnetic field). It is possible to describe these two types using a parameter called magnetic susceptibility (χ). The magnetic susceptibility is defined as a change of magnetization with a function of magnetic field. The molar susceptibility is related to one mole (given by Avogadro's number N_A) of the matter (**Equation 1**)

$$\chi = \mu_0 \left(\frac{\partial M_{mol}}{\partial M} \right) = \mu_0 N_A k_B \frac{\partial^2 \ln Z}{\partial B^2} \tag{1}$$

where μ_0 is the magnetic permeability of vacuum($4\pi 10^{-7}$ J·A^{-2}·m^{-1}), N_A is the Avogadro's number ($6.022045 \cdot 10^{23}$mol^{-1}), k_B is the Boltzmann constant ($1.380662 \cdot 10^{-23}$ J·K^{-1}), T is the thermodynamic temperature, Z is the partition function, M is the magnetization, B is magnetic field
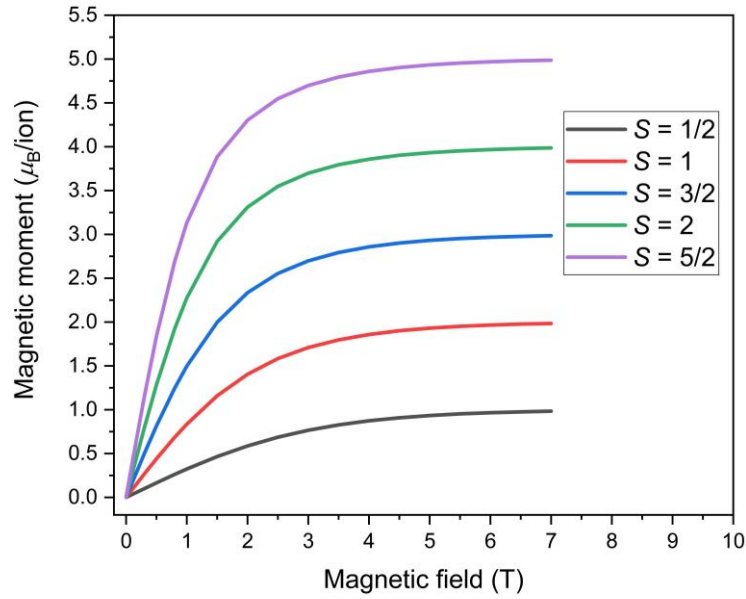
Figure 3: Brillouin function calculated for different values of S at 2K.

All magnetic materials show a specific interaction with the magnetic field *B*. Diamagnetism is the most common magnetic phenomenon, being present in every material. Such material when exposed to an external magnetic field, the electron pairs start to precess around the vector of the applied field, which is causing an induction of a magnetic force oriented in opposition to the external magnetic field. This is in the agreement with the Lenz law[12], however, it must be noted that correct description of the diamagnetism is quantum mechanical. Therefore, the diamagnetic material is expelled from the magnetic field. The diamagnetic susceptibility is usually very small, always negative (as the material is expelled from magnetic field) and independent from the temperature or magnetic field. As it was mentioned above, diamagnetism is present in all materials, so it must be taken into account during analysis of magnetic data, and it is usually expressed by using Pascal's constants χ_D.

When a material contains unpaired electrons in its structure, their orbital movement together with the spin precession produces magnetic moment. This magnetic dipole aligns with the external magnetic field and due to its orbital nature, it precesses around an axis of the applied magnetic field. This field induces magnetization in the material, which aligns parallel with the inducing field resulting into weak attractive force and this phenomenon is known as paramagnetism. After removing an external magnetic field, the magnetic moment of a paramagnetic material becomes zero again as individual moments are oriented randomly. Their susceptibility is positive (as the material is attracted by magnetic field) and small, magnetic field independent, but temperature-dependent since temperature is disrupting orientation of the

dipoles in the external field. The magnetization of ideal paramagnetic material in the magnetic field is described by Brillouin function (**Figure 3**) (**Equation 2**).

$$B = \frac{2J+1}{2J}\coth\left(\frac{2J+1}{2J}x\right) - \frac{1}{2J}\coth\left(\frac{1}{2J}x\right) \qquad x = \frac{g\mu_B JB}{k_B T} \qquad (2)$$

where *J* is angular momentum of an electron.

The pure paramagnetic susceptibility can be obtained by subtraction of diamagnetic susceptibility (Pascal's constants) from the molar susceptibility of material. Curie (**Equation 3**) and Curie-Weiss (**Equation 4**) (**Figure 4**) law describe the temperature dependence of paramagnetic materials.

$$\chi = \frac{C}{T} = C_0 \frac{S(S+1)}{3}\frac{g^2}{T} \qquad (3)$$

$$\chi = \frac{C}{T-\theta} \qquad \frac{1}{\chi} = \frac{T-\theta}{C} \qquad (4)$$

C is the Curie constant, C_0 the reduced Curie constant, Θ the Weiss constant, *S* is the electronic spin, *g* is the *g*-factor.
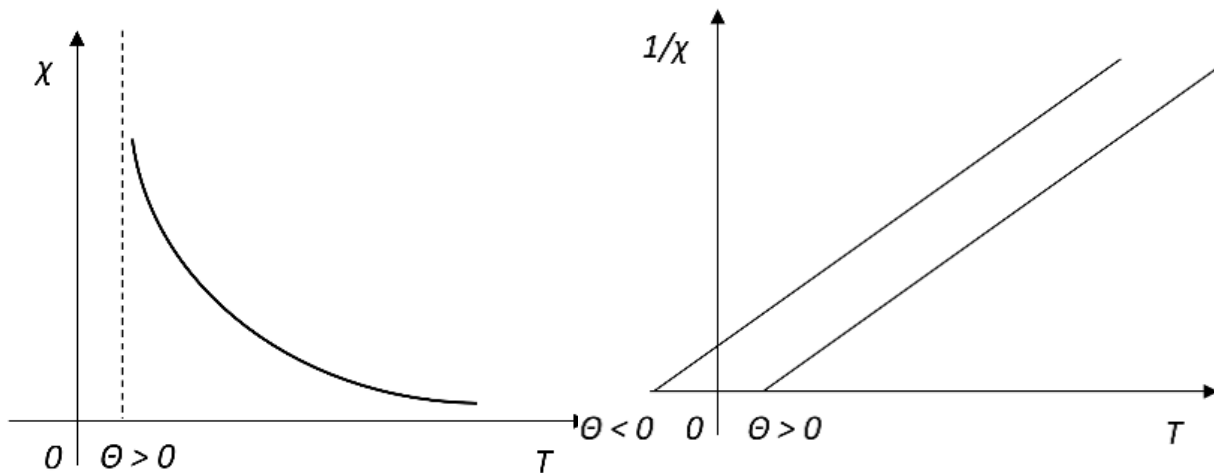
Figure 4: Plot of the Curie-Weiss law (left) and it's linearized version (right).

When a material preserves the orientation of magnetic moments even after removing an external magnetic field it means such a material is magnetically orders, which can refer to ferromagnetism, ferrimagnetism or antiferromagnetic. Upon decreasing the size of the studied material from bulk to nanosized particles another magnetic phenomenon called superparamagnetism may emerge. The classes of ordered magnetic materials differs from each other due to the orientation of the magnetic moments in the small volumes of matter– magnetic domains. Ferri- ferro- and antiferromagnetic materials have ordered magnetic moments below the critical temperature (Curie temperature T_C for ferro and ferrimagnetic and Néel

temperature T_N for antiferromagnetic) above which the domains cease to exist and orientation of magnetic moments changes into chaotic paramagnetic behaviour (**Figure 5**)[13]. Antiferromagnetic materials have magnetic moments oriented antiparallelly in the domain and the net magnetization is thus zero. Ferrimagetic materials have magnetic moments oriented in a similar manner to antiferromagnetic, only the magnetic moments are of different size and they do not cancel each other and their net magnetization is not zero. On the other hand, in the domains of a ferromagnetic materials the moments are oriented in parallel manner, although the moments of individual domains are oriented randomly and thus the overall magnetic moment of bulk material moment in absence of external magnetic field is zero.
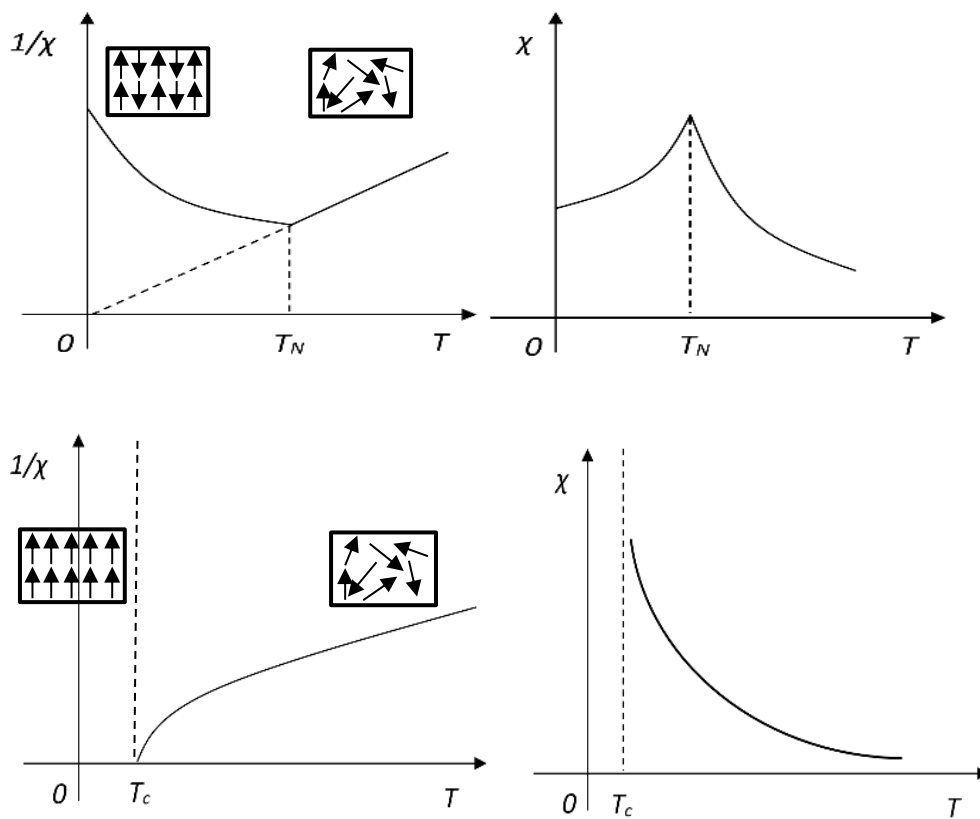

Figure 3: Dependence of molar susceptibility (top left) and reciprocal (top right) on temperature with defined Néel temperature T_N in antiferromagnetic material Dependence of reciprocal (down left) and molar susceptibility (down right) on temperature with defined Curie temperature T_C in ferromagnetic material.
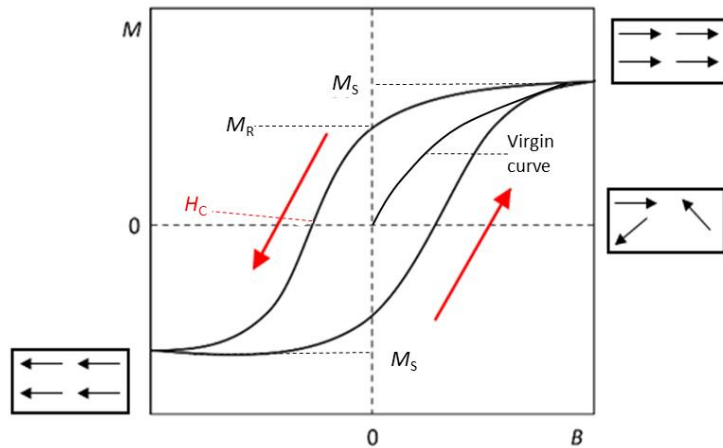
Figure 4: Example of magnetic hysteresis loop of a bulk material (up) highlighting the change of magnetic moment orientation (black arrows) in respect to the changing magnetic field. Red arrows show the change of magnetic coercive field.
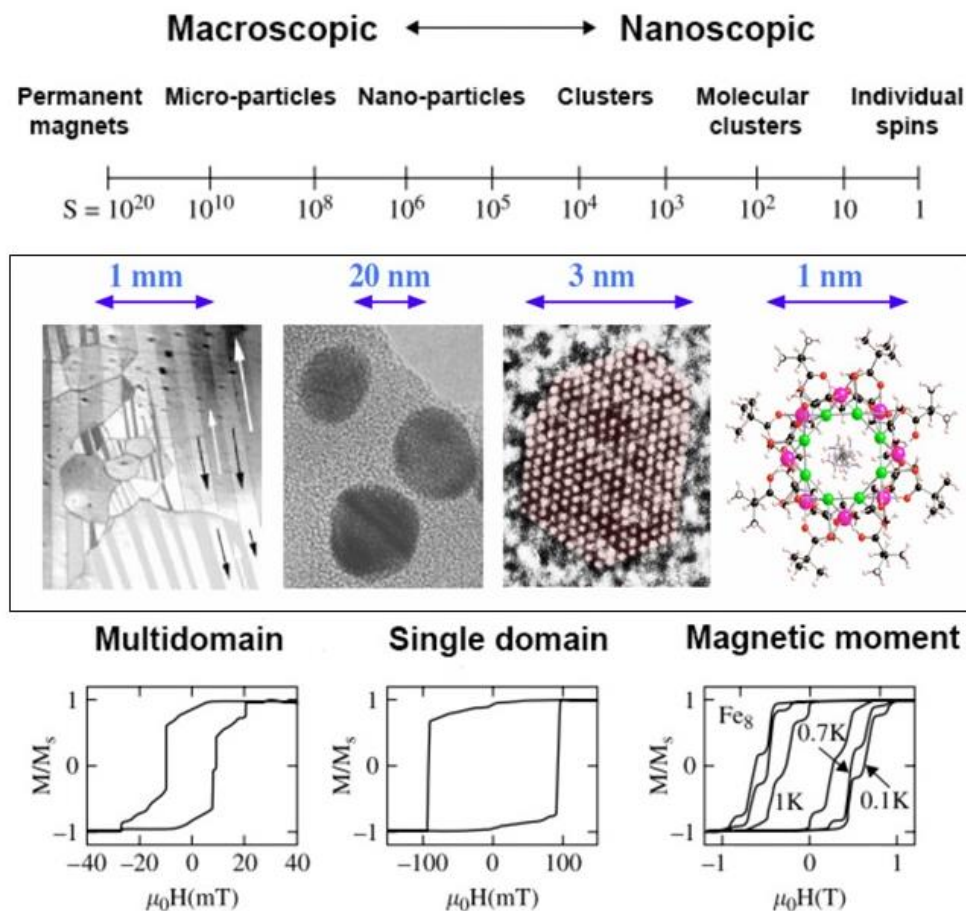
Figure 5: Examples of magnetic materials, the figure shows their typical properties linked to their size. Adapted from [14,15].

The ferro- and ferrimagnetic materials have a characteristically big and positive susceptibility. Their typical and important property is that they show magnetic hysteresis. With applied external magnetic field, the magnetic moments of domains are being oriented along the magnetic field (virgin curve) and it increases the resulting magnetization. The stronger the field

the more moments are aligned with the field. When the moments are aligned maximally (parallelly), and the magnetization is maximal, the saturation magnetization M_s is reached. The magnetization curve follows a different path with an increasing field than with decreasing. At zero applied magnetic field, the magnetization is non-zero – and it is called remanent magnetization M_r (**Figure 6**). The applied magnetic field necessary to change magnetization back to zero is called coercive field - H_c. This principle creates the magnetic hysteresis loop, which is essential for data storing (**Figure 7**).

Different from the above-mentioned types are superparamagnetic materials. With decreasing size of the bulk ferro- , ferrimagnetic or antiferromagnetic materials, the magnetic domains start to disappear until the point that whole particle gets one-domain character, but still all the magnetic moments are oriented in one directio. Such particle produce very large magnetic moment. Further decrease in size of the particle has an impact on the magnetic coercivity (an ability to withstand external magnetic field without being demagnetized) of this material as the coercivity increases to the critical point where the coercivity starts to decrease. Upon coercivity disappears the material is called superparamagnetic. In superparamagnetic materials the magnetic moment of particle fluctuates in between two orientations and remains in each for relaxation time τ. Anisotropic energy of the nanoparticle defines an energy barrier preventing the change in orientation of the magnetic moment (**Figure 8**). The energy of the barrier is close to the energy of thermal fluctuations equal to $k_B \cdot T$ (where k_B is Boltzman constant and T is temperature).

Inevitably thermal fluctuations cause the change of orientation of magnetic moment in direction (parallel and antiparallel) of the easy anisotropy axis of the nanoparticle. Superparamagnetic materials have two thermal states – high temperature and low temperature state which are distinguished by blocking temperature T_B. In the high temperature state have thermal fluctuations higher energy that the barrier E_A (**Equation 5**) and the magnetic moment changes its orientation freely[16].

$$E_A = KV sin^2\theta \tag{5}$$

Where K is the magneto-crystalline anisotropy constant and can be treated as the anisotropy energy per unit volume, V is the volume of the nanoparticle, θ is the angle between magnetization direction and the easy axis of the nanoparticle

13

Single-Molecule Magnets (SMMs) exhibit behaviour typical of superparamagnets with magnetic hysteresis below their blocking temperature T_B. A very important parameter of SMMs is their spin-reversal barrier (U_{eff}), which allows them to exist in two spin states $\pm M_s$ (**Figure 8 and 10**). This energy separating those two levels comes from the total spin of compound S and zero-field splitting (ZFS) parameter of axial magnetic anisotropy D and it can be represented by two equations (**Equations 6**).

$$U_{eff} = |D|S^2 \text{ for integer } S \text{ and } U_{eff} = |D|(S^2 - 1/4) \text{ for non-integer } S \qquad (\textbf{6})$$
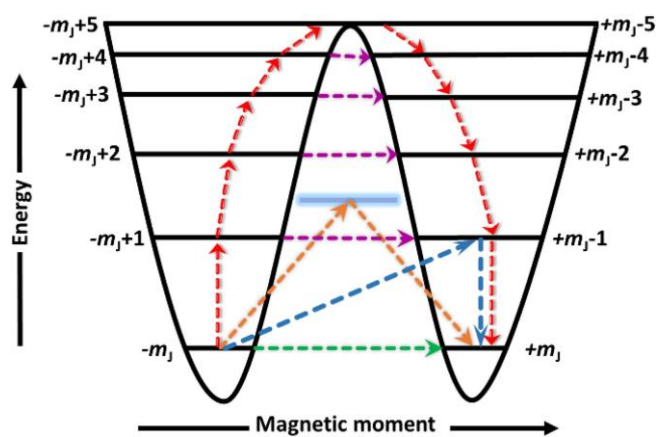

Figure 6: Depiction of different relaxation processes. Red and blue arrows represent Orbach process, green represents QTM and purple thermally assisted QTM, orange represents Raman process. Adapted from[17].

D could be either negative (axial, easy axis) or positive (equatorial, easy-plane) and it has a significant impact on SMM properties. Compounds possessing negative D have $Ms = \pm S$ levels lowest in energy and thus are the most stable and contribute to the spin-reversal barrier (**Figure 10**). In compounds with positive D value, spin-reversal barrier usually does not exist. Therefore, slow relaxation of magnetization does not occur. Although there are more and more exceptions from this rule being published, especially for 3d based SIMs. An explanation can be found in different type of relaxation than Orbach or specific combination of ZFS parameters (E/D) (**Figure 10**). In the Orbach relaxation process (**Figure 8** – red arrows) the magnetic moment overcomes the spin-reversal barrier and gradually follows the Ms levels given by the system. However, also the other relaxation processes can take a place, and these will be briefly described below. Direct process can occur between the nondegenerate $\pm M_S$ levels. During the Raman process (**Figure 8** – orange arrows) the virtual states are used to overcome the spin-reversal barrier. The **Q**uantum **t**unnelling of **m**agnetisation (QTM) (**Figure 8** - green arrow) occurs when the orientation of the moments tunnels through the barrier between two degenerated states. The later relaxation moment can be avoided by placing the studied system into a small external magnetic field which breaks the degeneration of levels and prohibits QTM

as it is not desired phenomenon. Majority of the systems start to show slow relaxation of magnetization only after applying such an external field and they are called field-induced SMMs (or field-induced SIMs).

The above-mentioned key parameter of SMMs/SIMs – slow relaxation of magnetization can be studied by SQUID (Superconducting Quantum Interference Device – discussed in chapter 4). The sample is placed into alternating magnetic field which is caused by applied alternating current (therefore it is called AC measurements or Dynamic magnetic measurements). The response of the sample (AC susceptibility) changes with the alternating field. This response can be delayed behind the alternating magnetic field, and it is caused by presence of energy barrier and slow relaxation of magnetization. The SQUID allow the study of both the barrier and relaxation. The output of the measurements the AC susceptibility is composed of two parts – in-phase susceptibility χ' and out-of-phase susceptibility χ'' (**Equation 10 and Figure 9**).
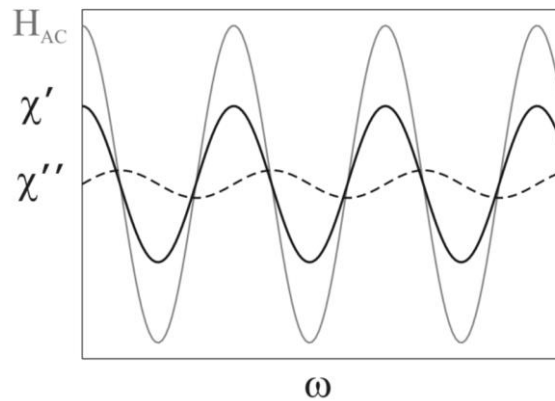
Figure 7: Depiction of dependence of response of in-phase susceptibility χ'(black line) and out-phase susceptibility χ''(dashed line) response to the alternating magnetic field (grey line). Adapted from[18]

This method strongly depends on temperature and the magnetic field. The maximum of χ'' is changing position with changing frequency and so for each frequency can be obtained relaxation time τ and using Arrhenius law (**Equation 7**) can be obtained value of energy barrier.

$$\tau = \tau_0 \exp(-\frac{U}{kT}) \qquad (7)$$

In compounds with negative D, the magnetic anisotropy is axial and so-called easy-axis magnetization is found (oriented along one axis). When D is positive, the observed magnetization is of in-plane type (energy barrier is not present). Once the D values are positive

and E values are big enough (maximal value is $E/D = 1/3$), the anisotropy is axial and easy-axis magnetization is present together with presence of energy barrier (**Figure 10**) [19,20].
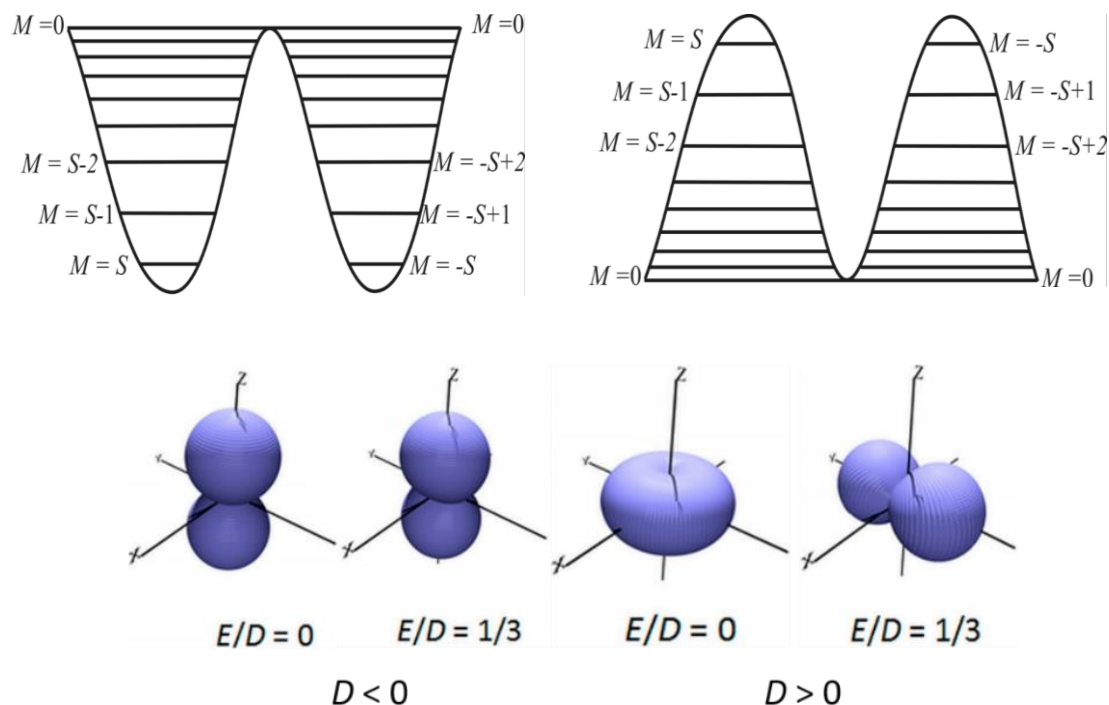
Figure 8: The depiction of spin-reversal barrier and MS states distribution for D<0 (left up) and D>0 (right up) and orientation of magnetization depending on E/D and D sign (bottom). Adapted from[21].

3.2 Single Molecule Magnets

After the first SMM Mn$_{12}$ (D = -0.46 cm^{-1}, S = 10) was reported by R. Sessoli et al. in 1993 [22] a quick increase of investigated polynuclear SMMs was observed in the next decade after the discovery. This was not successful research target, because later was proved that S^2 inversely contributes to D, opposite to expectations deduced from the energy barrier equation. Furthermore, magnetic moments (and thus orientation of anisotropy axes) of individual paramagnetic centres are not parallel to each other, and thus overall anisotropy (originating in sum of all components) is small (**Figure 11**) [23,24].

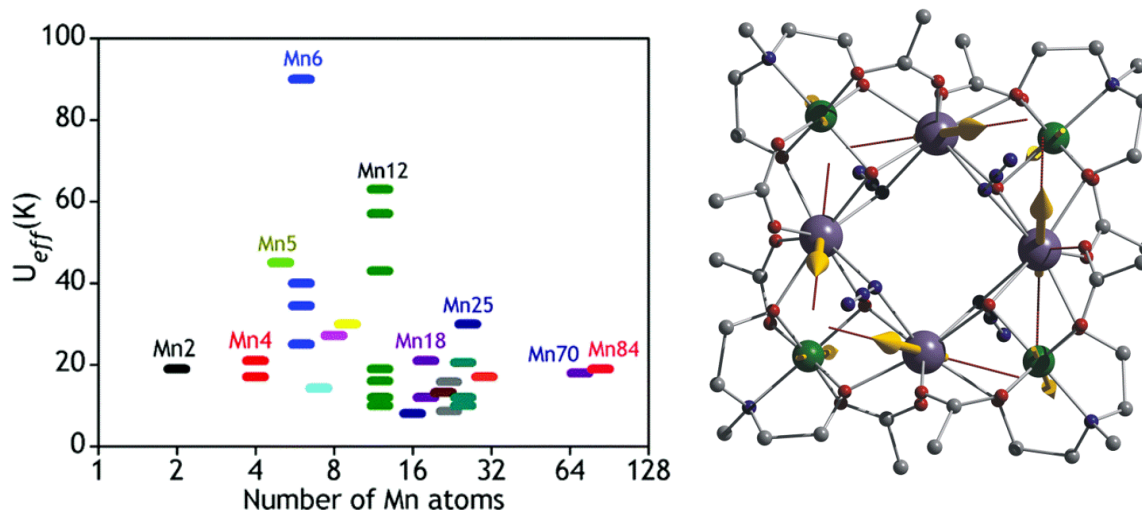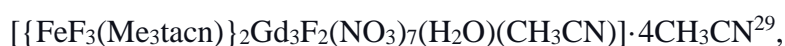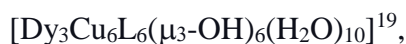*Figure 9: Values of energy barrier dependent of number of Mn paramagnetic centres (left)[25] and magnetic moments of individual paramagnetic centres pointing against each other (right).*

In 2003, for the very first time, it was shown by N. Ishikawa et al. [7] that coordination compounds containing only one paramagnetic centre (Tb^{3+}) can exhibit slow relaxation of magnetization. Such compounds are called Single-Ion Magnets (SIMs). Ihikawa's findings were quickly followed by 3d-based SIMs. The first 3d based SIM was Co^{2+} complex published by S. Karasawa et al., even though it is noteworthy that the cobalt atom is not the sole source of magnetic moment in this compound (as the Co^{2+} is coordinated by four carbene ligands each having two unpaired electrons)[26]. The cobalt compounds were soon followed by the Fe^{2+} SIM by D. E. Freedman and many others followed shifting focus towards SIMs[27].

The orientation of the magnetic moment in SMMs and SIMs can be controlled by the application of external magnetic field *B* and this orientation will prevail even after *B* is removed. As above-mentioned majority of published SMMs are actually a field-induced and so the presence of external magnetic field is necessary to break the energy degeneration of *Ms* levels and to observe slow relaxation of magnetization. SMMs/SIMs which are exhibiting slow relaxation of magnetization without the presence of an external magnetic field are often called zero-field SMMs/SIMs.

First, the scientists focused on the synthesis of coordination compounds with high *S*. Such an approach seemed logical concerning the equations (**Equations 6**), and several Zero-field SMMs were indeed prepared [19,20,25]. As was explained above systems as Mn_{12} have not brought expected results and attempts focused on 3d-4f systems. Several of them were prepared – $[Dy_3Cu_6L_6(\mu_3-OH)_6(H_2O)_{10}]$[19], $[Ni(\mu-L)(\mu-OAc)Dy(NO_3)_2]$[28], $[\{FeF_3(Me_3tacn)\}_2Gd_3F_2(NO_3)_7(H_2O)(CH_3CN)]\cdot 4CH_3CN$[29],

$[Mn_{21}DyO_{20}(OH)_2(ButCO_2)_{20}(HCO_2)_4(NO_3)_3(H_2O)_7]$[30] which in the year 2011 created new record for blocking temperature at 77 K, other examples followed[23–25,31–34].

The first of 3d row-based SIMs was $[Co(ppc)_4(SCN)_2]$ where ppc = (4-pyridyl)phenylcarbene published in 2003 by Karasawa et al.[26] as mentioned above. It possesses coordination number 6. It is necessary to mention that the crystal structure containing carbene ligands was not successfully obtained and the magnetic properties do not come purely from Co(II), but also from other interactions with the carbene unpaired electrons. This octahedral compound consists of cobalt in oxidation state 2+ coordinated by six nitrogen atoms, four coming from ppc ligands, and two from thiocyanate, the crystal structure is available only for precursor $[Co(dpp)_4(SCN)_2]$ where dpp = (α-diazobenzyl)pyridine (**Figure 26a**). The dynamic magnetic measurements revealed two peaks at each frequency and especially at 1 Hz, this suggested the presence of two components A and B. Relaxation time $\tau_0 = 2.3 \cdot 10^{-10}$s for component A and $3.2 \cdot 10^{-10}$s for component B was obtained from Arrhenius plot. Energy barrier was determined to be $U_{eff} = 89$ cm^{-1}. Blocking temperature was below 3.5 K. The DC magnetic properties show a narrow magnetic hysteresis in the range from 1.9-3.4 K (**Figure 12**).

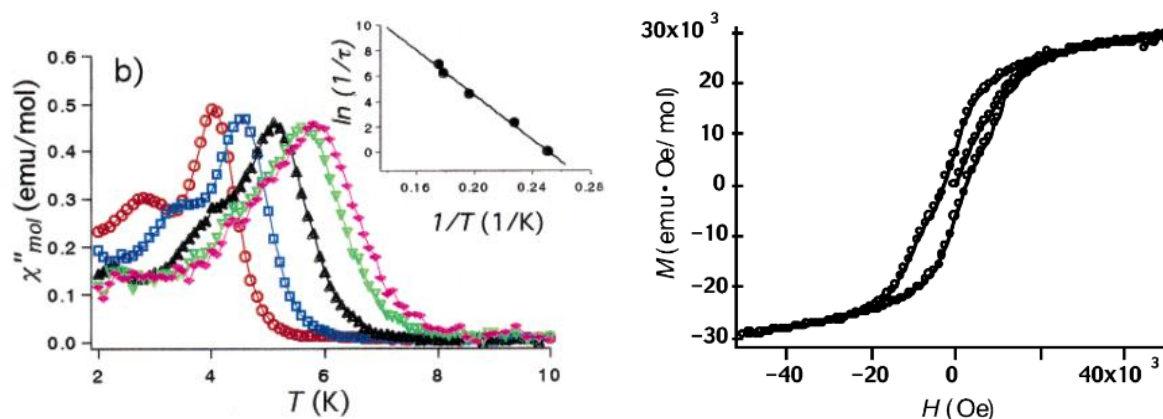*Figure 10: Dependence of out-of.phase AC susceptibility on temperature (left), magnetic hysteresis (right) measured for $[Co(ddp)_4(SCN)_2]$.*

Another record for the 3d SIMs family was reported by Zadrozny et al. in 2011 and it was coordination compound $(Ph_4P)_2[Co(SPh)_4]$[35] (**Figure 26b**). Complex anion is a simple molecule with coordination number 4 and an approximate D_{2d} symmetry, which exhibited remarkable magnetic relaxation in zero applied magnetic field. Authors assumed that quantum tunnelling is possible thanks to the mixing of $\pm Ms$ spin states via hyperfine interaction, dipolar interaction. Due to a large separation between molecules and utilization a non-integer spin, the mixing of spin states by E is prohibited by Kramer's theorem (**Figure 13**).

In DC magnetic measurements the value of effective magnetic moment start to decrease at 80 K. The best fit of DC magnetic data afforded $D = -74$ cm^{-1}. Frequency dependent AC

measurement shows temperature dependent peaks appearing from 1.8 K to 7 K when the frequency limit of the magnetometer was reached. This compound is a zero-field SIM, but the application of small external field significantly improves AC data (**Figure 14**).

This compound was diluted by isostructural compound $(Ph_4P)_2[Zn(SPh)_4]$ to study intermolecular interactions and their influence on the magnetic properties. The dynamic magnetic behaviour under zero and applied field is different in this case, the

Figure 11: d-orbitals splitting calculated for $(Ph_4P)_2[Co(SPh)_4]$.

maxima are shifted to lower frequency instead of forming another peak. Arrhenius plot showed temperature independence in contrast with a temperature-dependent plot in case of application of an external field or dilution with zinc (**Figure 14**). Energy barrier was determined to be $U_{eff} =$ 21 cm^{-1} (relaxation time $\tau_0 = 1.0 \cdot 10^{-7}$ s), which is in contrast a value predicted by EPR was U_{eff} = 140 cm^{-1}.

Figure 12: Dependence of out-of-phase AC susceptibility on frequency of $(Ph_4P)_2[Co(SPh)_4]$ (left), Arrhenius plot of relaxation time of pure $(Ph_4P)_2$ and diluted in matrix of $(Ph_4P)_2[Zn(SPh)_4]$ (right).

$(Ph_4P)_2[Co(SPh)_4]$ was followed by other two related compounds $(Ph_4P)_2[Co(OPh)_4]$ and $(Ph_4P)_2[Co(SePh)_4]$ by Zadrozny in 2013 [36](**Figure 26c**). Although published compound $(Ph_4P)_2[Co(OPh)_4]$ (**Figure 26d**) is not zero field SIM its diluted form $K(Ph_4P)[Co_{0.06}Zn_{0.94}(OPh)_4]$ is. The symmetry of $(Ph_4P)_2[Co(OPh)_4]$ (**Figure 26e**) is C_1 due to significantly twisted geometry of the phenyl ligands. After substitution of Ph_4P^+ by K^+ cation the symmetry has changed to D_{2d} due to the $K^+\cdots O$ interactions (**Figure 15**).

DC magnetic measurements showed a decrease of magnetic moment starting at 100 K. The DC data were fitted to spin Hamiltonian to obtain D and E parameters, which resulted in $D = -83$ cm^{-1} for $(Ph_4P)_2[Co(SePh)_4]$. AC measurements showed slow relaxation of magnetization at 2 K under zero applied field. Arrhenius plot corresponds to Orbach relaxation whereas Raman relaxation produces deviations from the plot. The values of dynamic parameters were obtained for $K(Ph_4P)[Co_{0.06}Zn_{0.94}(OPh)_4]$, $U_{eff} = 34$ cm^{-1} and $\tau_0 = 1.0 \cdot 10^{-9}$ s and for $(Ph_4P)_2[Co(SePh)_4]$, $U_{eff} = 19$ cm^{-1} and $\tau_0 = 3.0 \cdot 10^{-6}$ s. The dipolar interactions of cobalt ions is
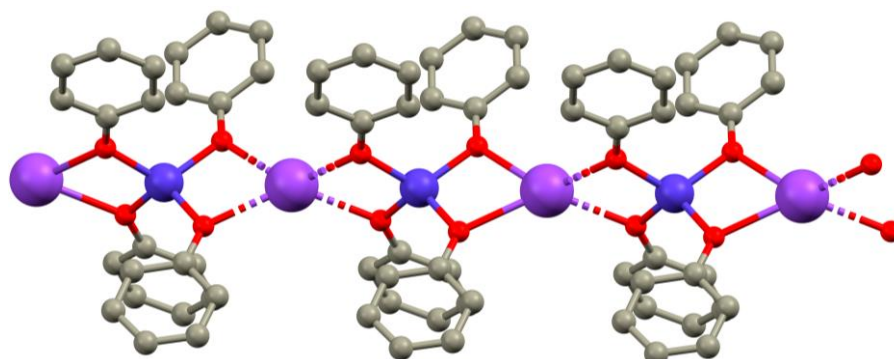
Figure 13: A perspective view on K$^+\cdots$O interaction in K[Co(OPh)$_4$]

partially responsible for lower barrier values than in the non-diluted compound.

Compound [(PNP)FeCl$_2$] is very rare example of SIM exhibiting also SCO (Spin-crossover) phenomenon, PNP = N[2-P(CHMe$_2$)2-4-methylphenyl]$_2$, published by Mossin et al. in 2012 [37] (**Figure 26f**). It possesses coordination number 5. SCO compounds can exist in two spin states, high and low-spin state. One-electron oxidation of precursor with Ph$_3$CCl was used to obtain coordination compound with iron in oxidation state +III. The compound was studied structurally by X-ray
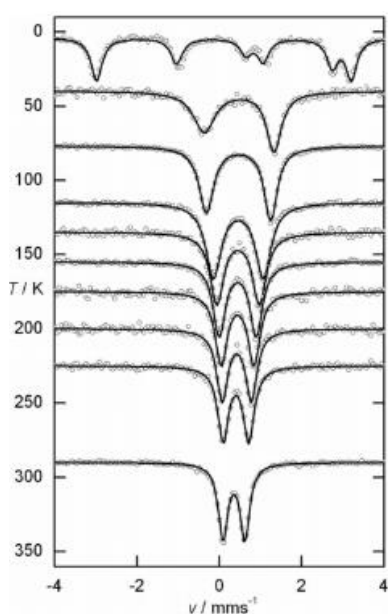
Figure 14: Mössbauer spectra of [(PNP)FeCl$_2$].
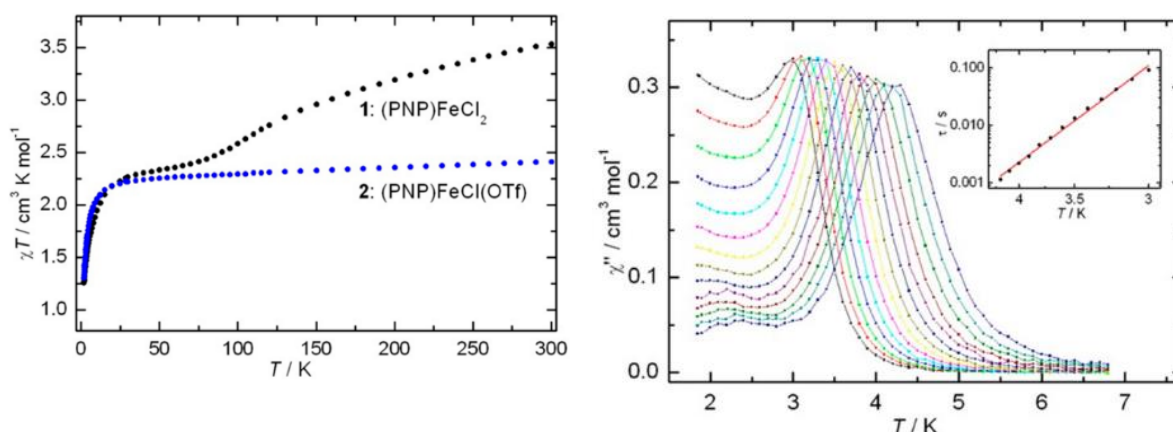
Figure 15: Temperature dependence of χT forDC (left) of [(PNP)FeCl₂] (black circles) and [(PNP)FeCl(OTf)] (blue circles) (left)and Dependence of out-of.phase AC susceptibility on temperature of [(PNP)FeCl₂] (right).

diffraction and it was found that the structure of coordination polyhedron is on the border between a square pyramid and trigonal bipyramid (Addison parameter $\tau = 0.55$). DC magnetic measurements were done also in solution, but better results were obtained for the measurement of microcrystalline phase. In a range from 2 to 300 K, the magnetic moment of K[(PNP)FeCl₂] shows significant temperature dependence over the entire region (**Figure 17**). The magnetization data were measured at three different temperatures showing significant deviation from Brillouine function and thus showing non-negligible anisotropy. Using the spin Hamiltonian parameters of ZFS were fitted to obtain $D = -11$ cm^{-1} and $E/D = 0.01$. No hysteresis was observed. AC measurements revealed frequency dependent maxima were observable under 5 K and under 3 K another relaxation process was observed (**Figure 17**). This second relaxation was not studied in detail and its origin is probably in weak intermolecular interactions. Data were processed into the Arrhenius plot showing thermally activated relaxation of the Orbach's type.

Relaxation time was determined to be $\tau_0 = 2 \cdot 10^{-8}$ s and barrier to $U_{eff} = 32$ cm^{-1}. Fitting only the high-temperature regime provided slightly different values $\tau_0 = 6 \cdot 10^{-9}$ s and spin reversal barrier of $U_{eff} = 36$ cm^{-1} were obtained. X-Band EPR spectra were measured for frozen CH₂Cl₂ at 4 K and broad resonance with *g* factor increasing with temperature until a maximum at 28 K was observed. Mössbauer spectroscopy was measured in a range from 4 to 298 K. At high temperatures, a doublet is observable, at about 77 K this doublet broadens, and at low temperatures doublet is split into six signals as an evidence of predominantly $S = 3/2$ ground state (**Figure 16).** This sextet was successfully fitted with data obtained from low-temperature SQUID and EPR so all those measurements are in a good match[37].
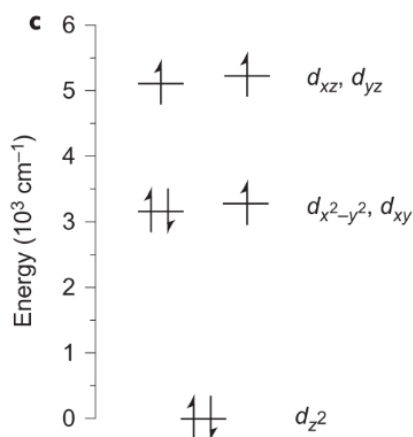
Figure 16: Splitting of d-orbitals and electronic configuration of [Fe(C(SiMe₃)₃)₂]⁻
.

The first iron-based zero-field SIM was followed by [Fe(C(SiMe₃)₃)₂]⁻ reported by Zadrozny et al. in 2013 [38]. This compound possesses coordination number 2. It contains two coordinate iron atom in oxidation state +I, this linear organometallic coordination compound shows both SIM and SCO properties. Authors used their experience from earlier publication [35] and applied prohibited mixing of spin states by Kramer's theorem with the spin of $S = 3/2$ (**Figure 18**). The reduction of iron atom in [Fe(C(SiMe₃)₃)₂]⁻ was studied by cyclic voltammetry and structure determined by X-ray diffraction revealing structure with cryptand cation [K(crypt-222)]⁺ [Fe(C(SiMe₃)₃)₂]⁻ and that ligand is coordinated by the C–Fe bond where the angle of C–Fe–C is almost linear (179.2°) (**Figure 26g**).

The DC magnetic measurements revealed that the effective magnetic moment was increasing upon cooling and reached maximum at 125 K, which was followed by a precipitous drop at 5.5 K, typical for transition metals complexes with the first-order orbital angular moment. AC data measurements showed a shift of maxima to higher frequencies with increasing temperature until it hits the limit of the instrument at 29 K. From Arrhenius plot it is obvious that major part of the relaxation goes through the Orbach process. Fitting of the AC data resulted in the following set of the parameters: $\tau_0 = 1.3 \cdot 10^{-9}$ s and $U_{eff} = 226$ cm⁻¹. This compound was also characterized by Mössbauer spectroscopy to confirm the oxidation state of the iron atom. At high temperature an asymmetrical doublet that changes to sharp sextet at 5 K is observable (**Figure 19**).
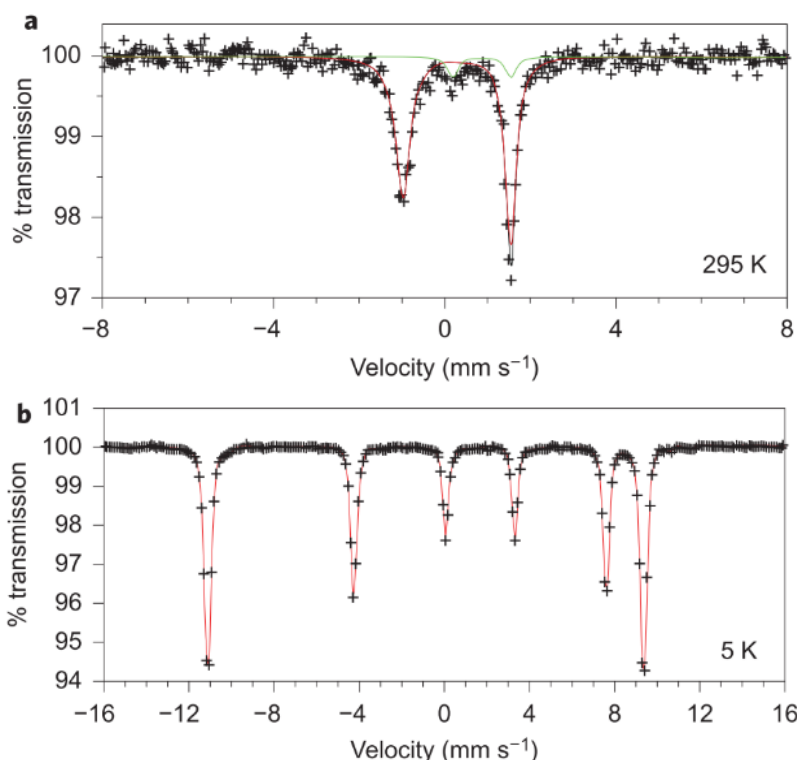
Figure 17: Mössbauer spectra of [Fe(C(SiMe₃)₃)₂]⁻ at 295 K (left) and 5 K (right).

Another zero-field SIM was published a year later by M. Fataftah et al. in 2014 [39]. The published
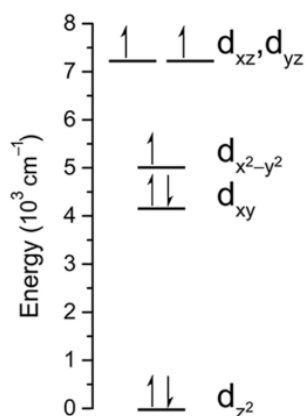
Figure 18: Splitting of d-orbitals and electronic configuration of [Co(C₃S₅)₂]²⁻.

compound $[Co(C_3S_5)_2]^{2-}$ (**Figure 26h**) possesses coordination number 4 and pseudo-tetrahedral coordination geometry (with deviation from ideal D_{2d} symmetry) and thus, the d-orbitals are split significantly off the typical splitting for the ideal tetrahedral geometry (**Figure 20**).

Decrease of magnetic moment in DC magnetic measurements decreases at 120 K down to 1.8 K, which is typical dependence for tetrahedral cobalt-based SIMs. Data were analyzed using spin Hamiltonian and fitted to D = -161 cm⁻¹ and zero rhombicity. From AC measurements a maximum at 2 K and 0.84 Hz is observable which rapidly shifts to higher frequencies with increasing temperature. Arrhenius plot is not linear in the whole range suggesting other types of relaxation giving values of U_{eff} = 33.9 cm⁻¹ and τ_0 = 4.5·10⁻⁶ s. The fit of barrier and relaxation type was changed only very little by application of an external field or dilution by diamagnetic zinc ion. Even after the application of a very high magnetic field of 45 T was not possible to obtain EPR spectra.
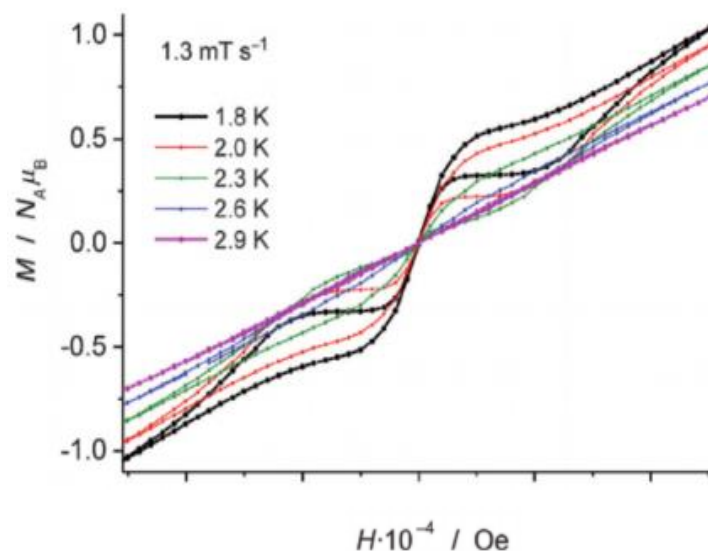
Figure 19: Magnetic hysteresis loop observed for [Co(paz)₃(PhB)]Cl.

Another zero-field SIM is compound [Co(paz)₃(PhB)]Cl, where paz = tris-pyrazolooximate and PhB = phenylboronic acid, with coordination number 6 and trigonal prismatic geometry. This was prepared for the first time by Varzatskii et al. in 2014 and magnetism was studied by Novikov et al. in 2015 [40,41] (**Figure 26i**). DC measurements in a broad range of temperatures showed a gradual decrease of effective magnetic moment upon decreasing temperature, which indicate large magnetic anisotropy. Using spin Hamiltonian the D and E parameters were fitted to obtain D = -82 cm⁻¹ and E/D = 0.003, indicating thus very large and axial anisotropy. No magnetic hysteresis was observed. Analysis of NMR spectra of [Co(paz)₃(PhB)]Cl via van Vleck equation was done to obtain D = -109 cm⁻¹, which is very similar to DC experiment and CASSCF calculations (D = -110 cm⁻¹, E/D = 0.004). Arrhenius plot shows non-linear dependence of relaxation time at temperature and significant deviation at higher temperatures. The value of the energy barrier was calculated to be U_{eff} = 102 cm⁻¹. A magnetic hysteresis was observed for this compound (**Figure 21**).

In the year 2015, a compound [Co((NtBu)₃SMe)₂] (**Figure 26j**) was published by Carl et al.[42] According to the X-ray experiment, this molecule has coordination number 4 and C_{2v} symmetry due to a distorted tetrahedral geometry of coordination polyhedron. The structure of bulky peripheral ligands secure that the cobalt ions are magnetically well isolated. The fit of DC magnetic data on spin Hamiltonian provided D = -58 cm⁻¹ and E/D = 0.15. From the Cole-Cole diagram and Arrhenius plot, the values of U_{eff} = 75 cm⁻¹ and τ_0 = 2.64·10⁻⁸ s were obtained.

In 2015 published Shao et al. [43] how anisotropy of trigonal Co(II) coordination compounds can be tuned by exchange of the donor atoms (**Figure 26p**). The authors prepared two compounds. First [Co(Me$_6$tren)Cl](ClO$_4$) with tetradentate ligand, where all the donor atoms of the organic ligand are nitrogen atoms. Second compound was [Co(NS$_3$^{iPr})Cl](BPh$_4$) with the same shape of coordination sphere (trigonal bipyramid with pseudo-C_{3v} symmetry) as the first type and also very similar tetradentate ligand, but with one axial nitrogen and three equatorial sulfur and donor atoms. DC and AC measurements were performed confirming SIM behavior. By the
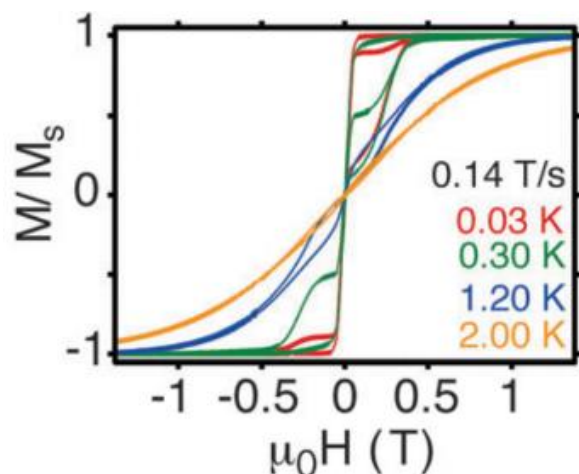
Figure 20: Magnetic hysteresis loop observed for [Co(NS$_3$^{iPr})Cl](BPh$_4$).

exchange of the donor atoms (S for N), the authors managed to increase the energy barrier from 16 cm^{-1} to 32 cm^{-1}. From magnetization measurements a magnetic hysteresis was observable for [Co(NS$_3$^{iPr})Cl](BPh$_4$) (**Figure 22**).

Another cobalt-based zero-field SIM (HNEt$_3$)$_2$[Co(L2)$_2$] (**Figure 26k**), where H$_2$L2 = 1,2-bis(methanesulfoamido)benzene, was published in 2016 by Rechkemmer et al. [44]. From X-ray diffraction experiments it is clear that cobalt ion is tetracoordinated (D_{2d} symmetry), although oxygen atoms are a rather close to the central atom (approximately 3.1 Å) and thereby possible
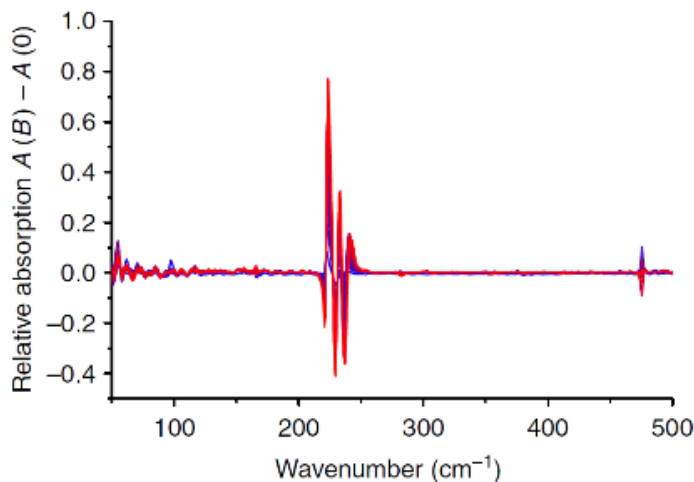
Figure 21: FTIR magneto-spectroscopy measurement of (HNEt$_3$)$_2$[CoL$_2$].

25

influence on the structure and magnetic properties of this compound cannot be excluded. The fit of DC magnetic measurements gave D = -115 cm^{-1}. A butterfly shape magnetic hysteresis was observed. Due to large magnetic anisotropy a FTIR magneto-spectroscopy was performed instead of HF-EPR. The measurements performed up to 11 T showed very large zero-field gap corresponding to $|D|$ = 115 cm^{-1} (**Figure 23**). The analysis of AC magnetic data give following values: U_{eff} = 118 cm^{-1} and τ_0 = 3.89 $\cdot 10^{-8}$ s.

The results on [Co(iPr$_2$P(Se)NP(Se)iPr$_2$)$_2$] were published in 2016 by Sottini et al. (**Figure 26l**) [45]. This publication demonstrated how a change of the donor atoms can influence magnetic properties since [Co(iPr$_2$P(Se)NP(Se)iPr$_2$)$_2$] is zero-field SIM and its isostructural analogue [Co(iPr$_2$P(S)NP(S)iPr$_2$)$_2$] is only field-induced SIM. Complex with the S-donor atoms possesses an S_4 symmetry axis and shows a dihedral angle of 90° in between S−Co−S endocyclic planes (ideal tetrahedron) whereas there was no high symmetry observed for the Se-donor atoms containing compound. From the DC magnetic measurements, the following ZFS parameters were obtained: D = -30.4 cm^{-1} and E/D = 0.0016. There is a significant difference between dynamic magnetic behaviors of pure and zinc diluted compounds, zinc diluted compound showed much more linear dependence of the relaxation time on temperature in comparison to the Arrhenius plot in zero external fields.

A cobalt-based SIM of mixed valence (HNEt$_3$)(Co(II)Co(III)$_3$L$_6$) was reported by Zhu et al. in 2013 [46] (**Figure 26y**). According to the X-Ray experiment the coordination number of a central atom Co(II) is 6 and is coordinated by six oxygen donor atoms which gives it geometry of slightly distorted trigonal prism of D_3 symmetry. The central atoms Co(III) also possess coordination number 6 with four oxygen donor atoms and two nitrogen donor atoms. The DC magnetic measurements give the ZFS parameters: D = -115 cm^{-1}, E = 2.8 cm^{-1} and g = 3.05. The AC magnetic measurements revealed presence of slow relaxation of magnetization even without the presence of external magnetic field and confirmed this compounds as zero-field SMM.

Many lanthanide-based SIMs have been prepared since discovery of first Ln based SIMs. Since this thesis is focused on SIMs with trigonal symmetry it is appropriate to discuss several examples of lanthanide-based zero-field SIMs with such symmetry.

Synthesis of [Dy(N(SiMe$_3$)$_2$)$_3$] was published in 1972 by Bradley et al. and it was structurally and magnetically studied together with [Dy(NHPhiPr$_2$)$_3$(THF)$_2$] in 2014 by Zhang et al. [47,48] (**Figure 26x**). The central Dy(III) ion in [Dy(N(SiMe$_3$)$_2$)$_3$] is coordinated by three nitrogen

donor atoms in the shape of the trigonal pyramid giving molecule C_{3v} symmetry. The central ion of [Dy(NHPhiPr$_2$)$_3$(THF)$_2$] is also coordinated by three nitrogen donor atoms but also by two axially coordinated THF molecules. From the AC magnetic measurement, a deviation from the linear behavior of relaxation time was observed due to QTM induced by the rhombic anisotropy. Fitting of the magnetic data provided U_{eff} = 85 cm^{-1} and τ_0 = 9.33·10^{-9} s. Compound [Dy(NHPhiPr$_2$)$_3$(THF)$_2$] showed the Arrhenius like resulted in the following parameters: U_{eff} = 23.6 cm^{-1} and τ_0 = 2.07·10^{-5} s.

Trigonal [Dy$_3$(L3)(μ_3-OMe)$_2$(NO$_3$)$_3$] with multidentate amino-bis(phenolate) ligand was published in 2014 by Hänninen et al.[49] (**Figure 26w**). This compound possess symmetry of biaugmented trigonal prism. Each Dy(III) atom has coordination number 8 and is coordinated by one L3 and one NO$_3^-$ ligand The ligand L3 also acts as a bridging ligand together with the molecules of methanol located at C$_3$ axis in the center of the triangle formed by the Dy atoms. DC magnetic data revealed sudden drop of effective magnetic moment bellow 35 K. The AC magnetic data showed slow relaxation of magnetization under zero applied magnetic field.

Several Dy(III) compounds with simple trigonal aliphatic ligand H$_3$tea = triethanolamine were published. [Dy$_2$(NO$_3$)$_4$(teaH$_2$)$_2$] was reported in 2017 by Margaritis et al.[50] (**Figure 26r**). The symmetry of the complex is close to D_{2h}. Each Dy(III) atom has coordination number 9 atom is coordinated by one tetradentate H$_3$tea ligand and two NO$_3^-$ ligands, each Dy is additionally coordinated by and O-donor atom from neighboring H$_3$tea. The AC magnetic measurements unfortunately did not revealed a slow relaxation of magnetization.

Another dimer [Dy$_2$(teaH$_3$)$_2$(MeCOO)$_4$] was published in 2018 by Koroteev et al.[51] (**Figure 26v**). In the complex molecule each the Dy(III) atom has coordination number 8 due to coordination of the central atom by tetradentate H$_3$tea and by one monodentate MeCOO$^-$ ligand. The geometry of coordination polyhedron is distorted trigonal dodecahedron. The DC magnetic measurements showed a sharp decrease of the effective magnetic moment below 6 K but AC magnetic measurements were not performed.

Compound [Dy$_4$(teaH$_2$)$_2$(teaH)$_2$(NO$_3$)$_6$]·2CH$_3$OH was reported by Li et al. in 2020 [52](**Figure 26q**). This chain-like coordination compound contains of four Dy(III) ions, two peripheral are coordinated each by one H$_2$tea and two NO$_3^-$ ligands and the remaining are coordinated each by one Htea ligand and one NO$_3^-$ ligand. The Htea^{2-} ligand serves as bridging ligands. The slow relaxation of magnetization was not observed even under the applied magnetic field.

Hexanuclear complexes [Dy$_6$(teaH)$_6$(NO$_3$)$_6$]·8MeOH (**Figure 26t**). and [Dy$_6$(pdeaH)$_6$(NO$_3$)$_6$] where pdeaH = 3- [bis(2-hydroxyethyl)amino]propan-1-ol were reported in 2009 by Langley et al. [53]. The structure of the first consists of six Dy(III) organizes into a ring with Htea acting as a bridging ligand and each Dy is additionally coordinated by one NO$_3^-$ ligand. The same structure has the latter complex only with Hpdea ligand. Both complexes exhibited field-induced slow relaxation of magnetization confirmed by the AC magnetic measurements and in the case of [Dy$_6$(pdeaH)$_6$(NO$_3$)$_6$], also under the zero applied magnetic field. The barrier and relaxation time were calculated for the latter compound: U_{eff} = 10 cm^{-1} τ_0 = 1.8·10^{-6} s.

The Dy(III) based coordination compounds with the Mannich type of ligand (a ligand formed by Mannich reaction – a three component organic reaction involving amino alkylation of acidic proton next to carbonyl functional group by formaldehyde and amine forming β-amino-carbonyl compound) with trigonal symmetry are remarkably rare. Complex [Zn$_3$Dy$_3$(μ_6-CO$_3$)(μ_3-OH)$_3$(L4)$_3$(H$_2$O)$_3$]·3(ClO$_4$)·NO$_3$, where L4 = 6,6'-{[2-(dimethylamino)ethylazanediyl]bis(methylene)}bis(2-methoxy-4-methylphenol) was reported in 2017 by Goura et al. [54] (**Figure 26u**). Each the Dy(III) atom is coordinated by four O-donor atoms from two L4 ligands, one hydroxyl ligand and one aqua ligand. Additionally, each Dy atom is coordinated by two O-donor atoms of CO$_3^-$ ligand positioned in the middle of Dy triangle with the C_3 axis (approximate C_{3h} symmetry) perpendicular to the CO$_3^-$ ligand plane. DC magnetic measurements revealed a sudden drop of the effective magnetic moment below 15 K. The AC magnetic measurements showed SMM behavior under zero applied magnetic field. The barrier and relaxation time were calculated: U_{eff} = 48 K τ_0 = 1.0(1)·10^{-6} s

Obviously, there were reported also SIMs with different symmetry than trigonal. Below, the summary of the Ln based SMMs with the most remarkable properties (highest blocking temperature of U_{eff}) is provided.

Two isostructural coordination compounds [Dy(Cy$_3$PO)$_2$(H$_2$O)$_5$]X$_3$·(Cy$_3$PO)·H$_2$O·EtOH, where X = Cl$^-$ and Br$^-$ (**Figure 26m**), were reported by Chen et al. [55] in 2016. Both compounds formed pentagonal bipyramid coordination polyhedron (D_{5h} symmetry). Besides the unusual shape of the coordination sphere, these compounds also showed remarkable stability to the water and oxygen, which is not common for this type of compounds. DC measurements revealed a sharp decrease of the effective magnetic moment below 11 K. The AC measurements showed typical SIM dynamic magnetic behaviour with the highest peaks at 28.5 K and 35 K

respectively. No significant QTM was observed in these molecules. Fitting of the AC data gives: $U_{eff} = 296.5$ cm^{-1}, $\tau_0 = 8.7 \cdot 10^{-12}$ s and $U_{eff} = 377.4$ cm^{-1}, $\tau_0 = 2.0 \cdot 10^{-10}$ s. A butterfly-shaped magnetic hysteresis for both the compounds was observed and there is a significant broadening of the loop after dilution with yttrium Dy:Y (1:19, **Figure 24**).

The noteworthy Ln-based SIMs with a sandwich-type structure were reported in the recent years. [(Pc(OEt)$_8$)$_2$Tb]$^-$ was published by Takamatsu in 2007 [56]. The authors showed how significant influence has the modification of ligand. In the original paper[7], Ishikawa used pure
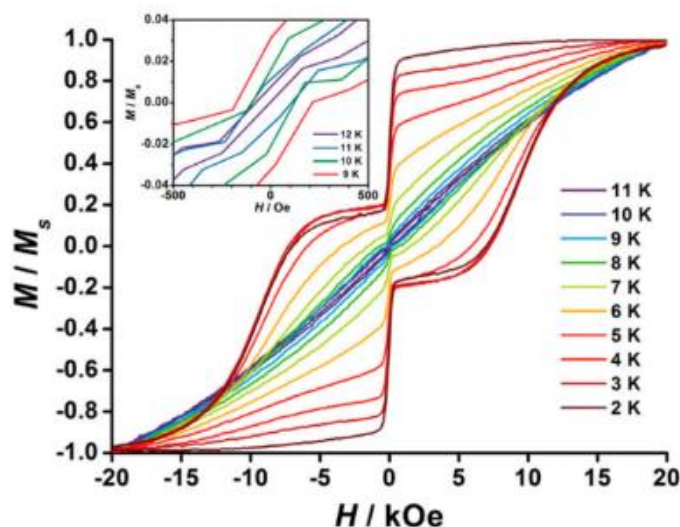
Figure 22: Magnetic hysteresis observed for yttrium diluted Cl$_3$ derivate.

phthalocyanine as ligand and in this publication, authors used 2, 3, 9, 10, 16, 17, 23, 24-octaethoxyphtalocyanine. This compound is a zero-field SIM.

Other two examples are very similar, the first one [(Cp^{ttt})$_2$Dy]$^+$ was reported by two groups simultaneously in 2017 [57,58] (**Figure 26n**). This compound was an important milestone in the research of SIMs because it showed a slow relaxation of magnetization up to 60 K with a very large barrier $U_{eff} = 1223$ cm^{-1}. The compound [(Cp^{iPr5})Dy(Cp*)]$^+$ was prepared by Guo et al. in 2018 [59] (**Figure 26o**) and it is a modification of the first one, but the modifications were so significant, that the blocking temperature shifted from 60 K to 80 K, which is above the boiling point of liquid nitrogen. This compound possesses remarkably high barrier $U_{eff} = 1541$ cm^{-1} and wide magnetic hysteresis (**Figure 25**).
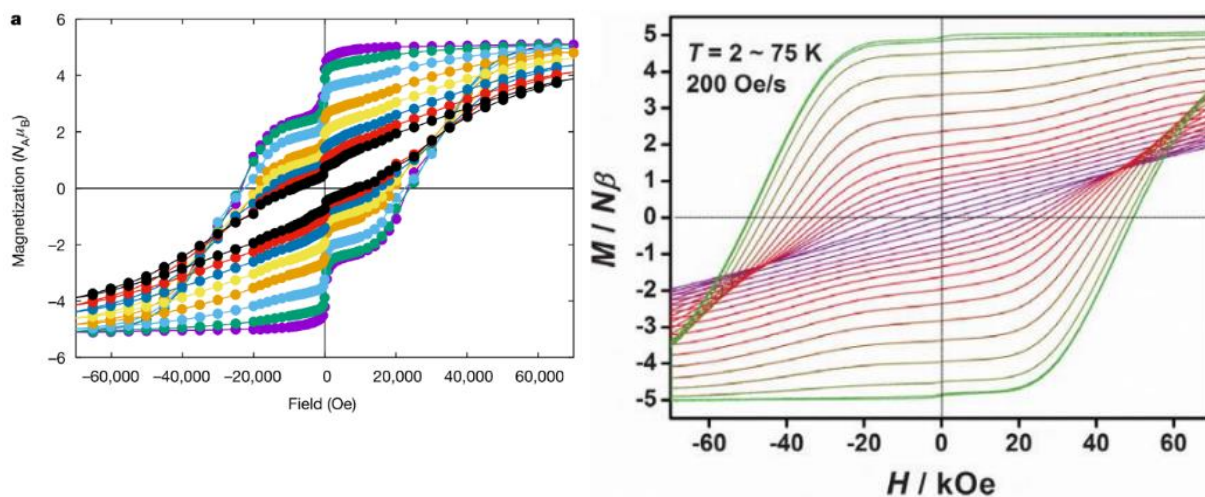
Figure 23: Magnetic hysteresis observed for [(Cp^{ttt})_2Dy]^+ (left), and for [(Cp^{iPr5})Dy(Cp)]^+ (right).*
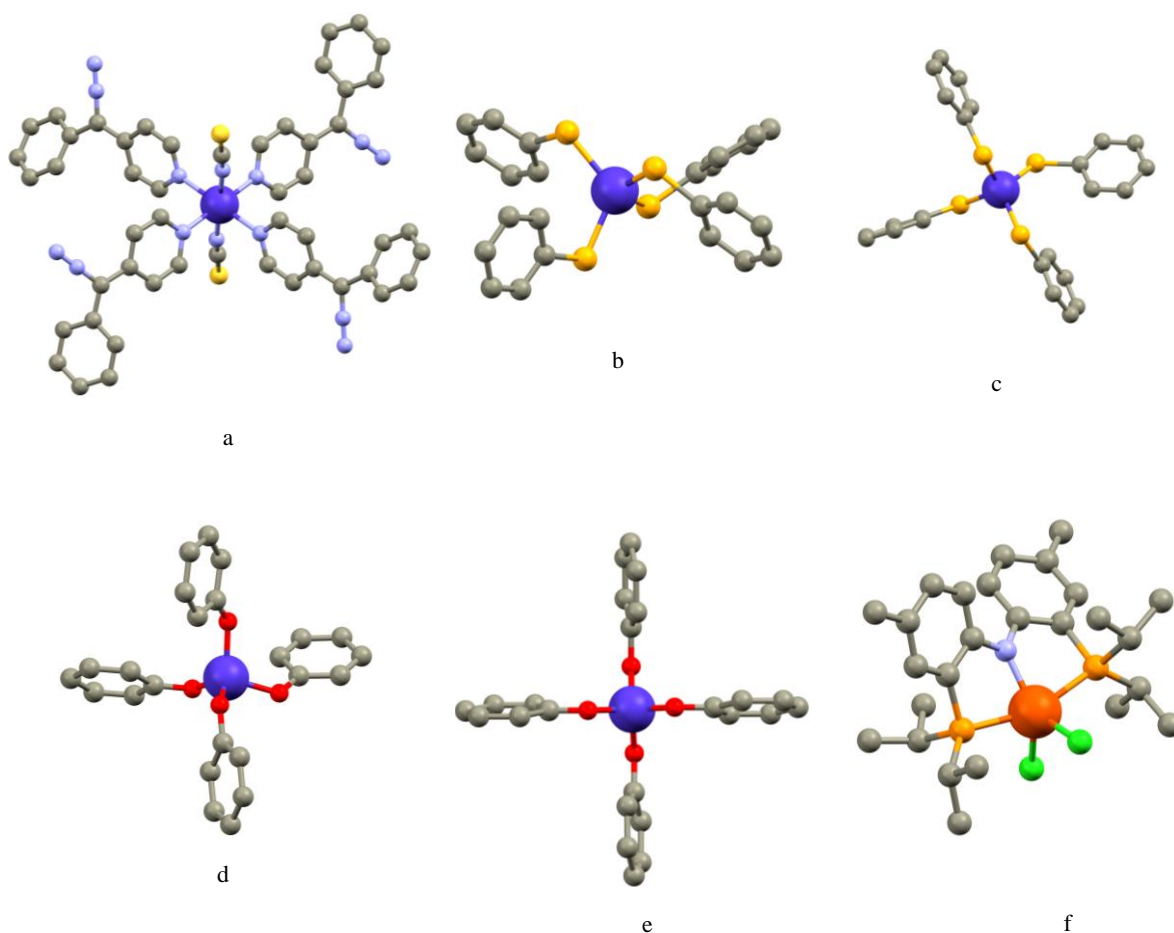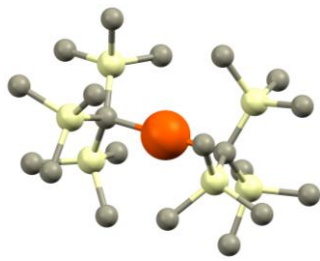
g
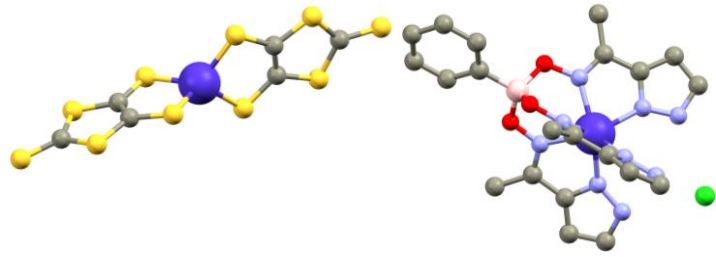
h

i
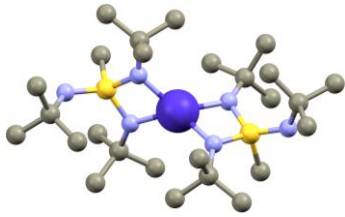
j
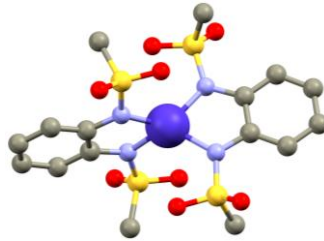
k
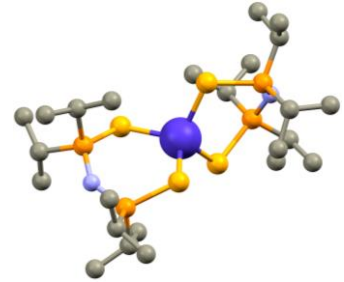
l
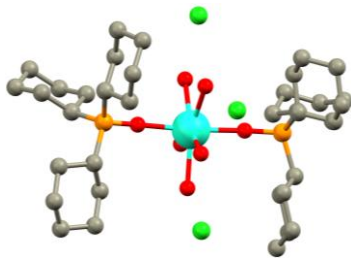
m
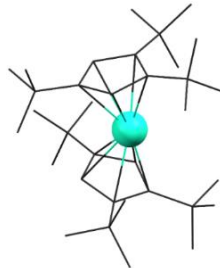
n
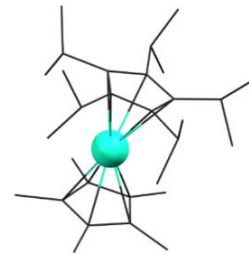
o
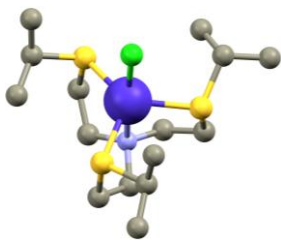
p
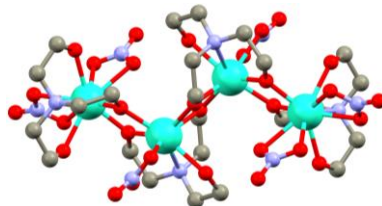
q
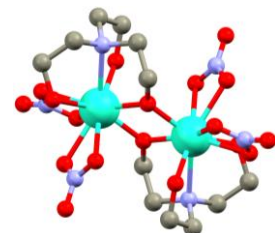
r
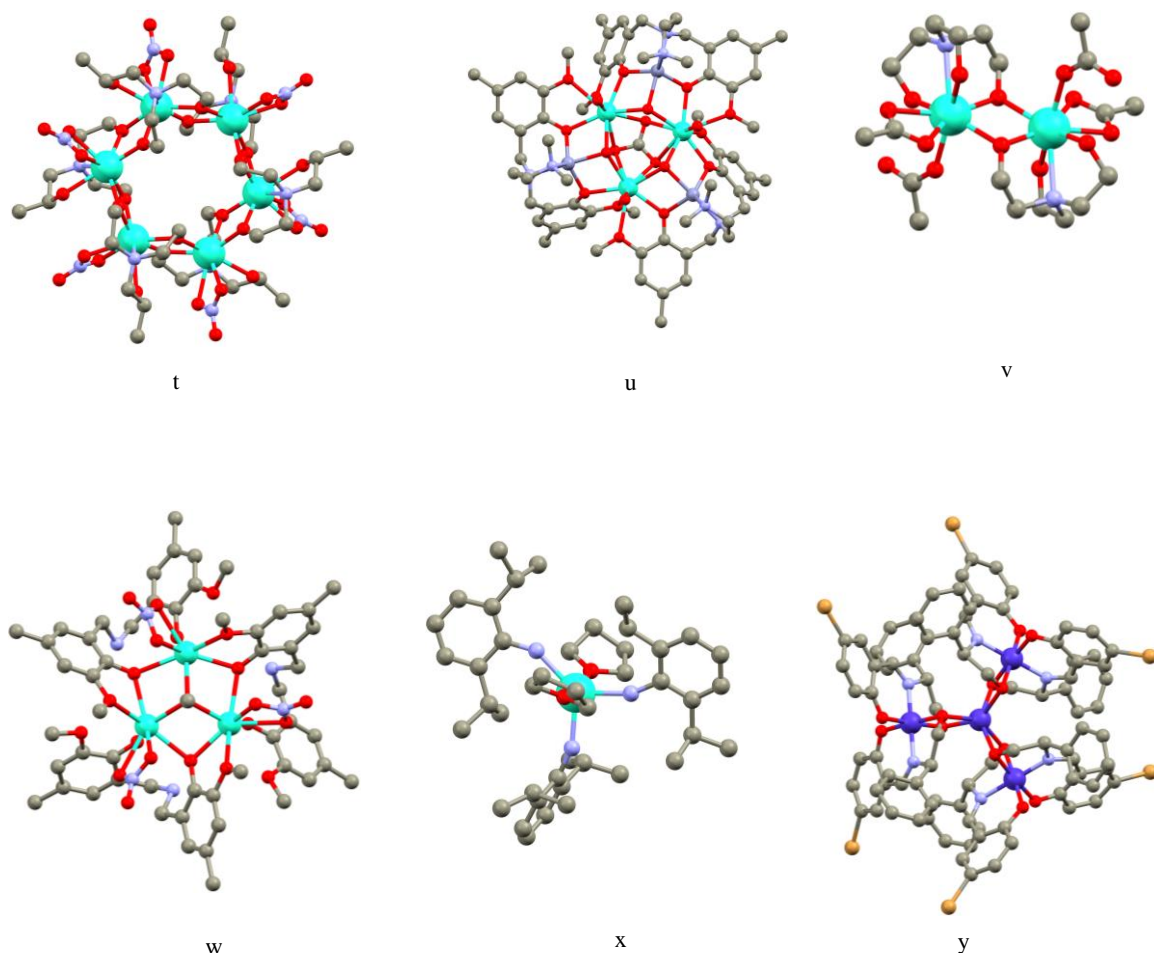
Figure 24: Crystal structures of discussed coordination compounds. Purple (Co), grey (C), light blue (N), yellow (S). dark yellow (Se), orange (P), green (Cl), red (O), dark orange (Fe), pink (B), light yellow (Si), azure (Dy). The hydrogen atoms are omitted for clarity.

3.3 Depositions of Single Molecule Magnets

To construct spintronic or data storage devices out of SMM/SIMs by conventional methods, it is necessary to create organized molecular arrays and to have a control over the individual molecules. One of the possible ways is to make addressable layers by deposition on the surfaces. This caused rising interest in fabrication and utilization of so-called 2D materials. The most studied is graphene, a single layer of the carbon atoms in hexagonal arrangement with interesting chemical and electrical properties that hold promise for a next generation of electronic devices. The goal is to combine 2D materials with well-designed SMMs and create hybrid materials with the defined layer of the SMMs molecules on the selected surface. The deposition can be strengthened by forming the covalent bonds between SIM/SMM and the surface (for example Au-S covalent bonds). For organized deposition of SMM on graphene the non-covalent interactions – alky-π, π-π, or halogen-π play a significant role. Coordination

compounds with long alkyl chains or aromatic rings will then form such interactions with graphene and self-assemble on a surface [60,61]. Ligands containing halogens can interact with graphene-based surfaces due to halogen electronegativity and affect the electronic transport in graphene, and thus magnetic properties of the prepared hybrid material [62]. Most of the reported results are based on phthalocyanine ligands forming a uniform layer as these compounds are planar and aromatic. These reports show that the magnetic moment of deposited SIMs remained unquenched, and thus these systems are good candidates for spintronics [63,64]. More variability in the type of the central atom and shape of the coordination sphere, crucial for magnetic properties, is offered by SIMs with the ligand in the shape of aromatic anchoring arms – such chemical modification offers a way for SIM/SMM to interact with a surface.

For the first time a magnetic hysteresis of the SMM deposited in a form of monolayer was observed in 2010 by Mannini et al[65]. Mannini took and advantage of chemical modification of already known Fe4 based SMM compound and prepared [Fe$_4$(L)$_2$(DPM)$_6$] (where H$_3$L is 7-(acetylthio)-2,2-bis(hydroxymethyl)heptan-1-ol and HDPM is dipivaloylmethane) in which the long aliphatic chain is terminated by the sulfur atoms. Molecules of this compound were deposited onto a gold surface as gold and sulfur has strong affinity and form together strong Au-S bonds. The magnetic hysteresis of such created hybrid material was studied by XMCD (**Figure 27**) which directly proved that the easy magnetization axis of the deposited complex molecule were oriented perpendicular to the surface. The magnetic properties have remained unchanged in comparison with the bulk material.
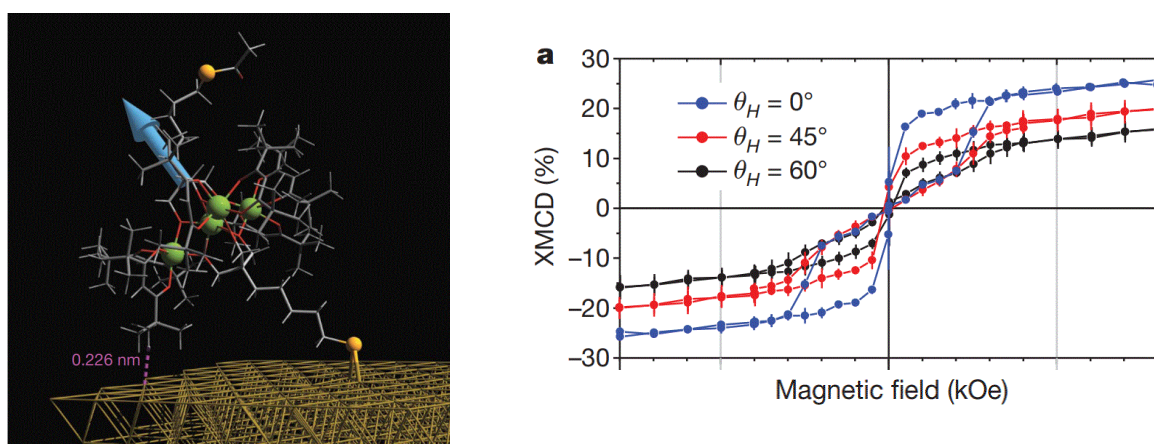
Figure 25: The periodic DFT optimized structure of [Fe$_4$(L)$_2$(DPM)$_6$] on the Au surface (left) and magnetic hysteresis from XMCD measurements (right)[65].

The properties of SMM/SIMs can change in combination with surfaces. Such a change can be positive as was reported by Wäckerlin et al. in 2016 [66] where authors deposited [TbPc$_2$],

where Pc = phthalocyanine, on nonmagnetic and insulating MgO surface on Ag. The SIM molecules were adsorbed on the surface by sublimation and scanning tunnelling microscopy revealed that they self-assembled themselves into the perfect 2D islands (**Figure 28**). This excluded the possibility of a magnetic contribution of the [TbPc$_2$] molecules tilted towards the surface. The XMCD revealed significant widening of magnetic hysteresis compared to the bulk material. Thermally dependent XMCD showed slow relaxation of magnetization bellow 8 K. The best results were obtained upon deposition on multilayer of MgO, even though that [TbPc$_2$] deposited on MgO monolayer still showed magnetic hysteresis. It was found out that upon deposition the [TbPc$_2$] retains its almost prefect D_{4d} symmetry, which contrasts with breaking symmetry of [TbPc$_2$] to C_{4v} and lower, upon its deposition on the metallic surfaces (such systems showed almost no or no hysteresis)[67,68].

(a)

(b)
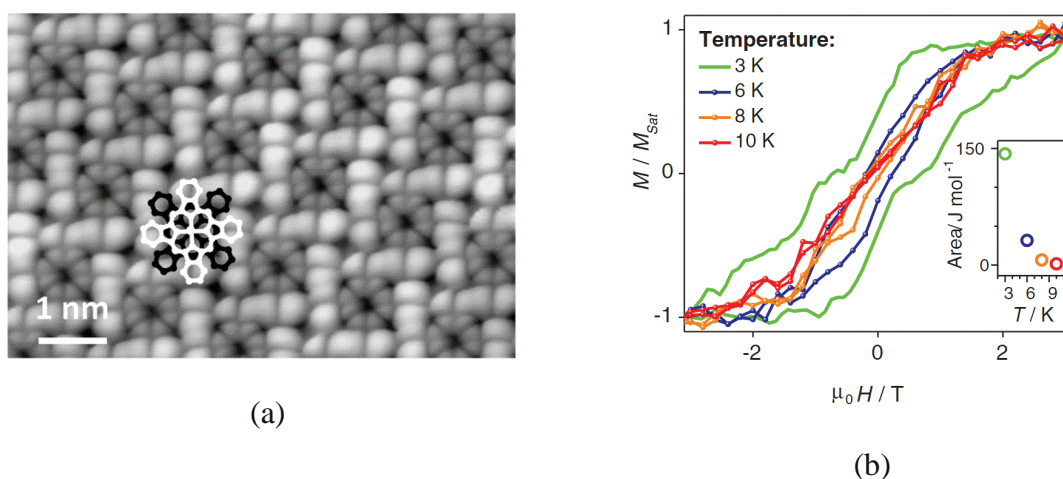
Figure 26: a) STM of [TbPc$_2$] forming self-assembly islands on MgO, b) temperature dependent magnetic hysteresis of the [TbPc$_2$]/MgO hybrid material

The magnetic properties can also worsen or even be suppressed upon deposition of SMMS on a surface. Bogani et al. published in 2007 a deposition of [Mn$_{12}$O$_{12}$(pCH$_3$SC$_6$H$_4$COO)$_{16}$(H$_2$O)$_4$] on the gold surface. The SMM was anchored to the surface in a form of monolayer by strong Au-S bonds. This hybrid material was studied by magnetic molecular dichroism and the absence of magnetic hysteresis was revealed suggesting dramatic change in magnetic properties upon deposition. Mannini et al. published deposition of [Mn$_{12}$O$_{12}$(RCO$_2$H)$_{16}$(H$_2$O)$_4$]·4H$_2$O·2CH$_3$CO$_2$H (where RCO$_2$H = 4-(methylthio)benzoic acid) on a gold surface in 2009. In this case the Mn$_{12}$ molecules were simply adsorbed on the surface as there is no anchoring functional group which could form a bond with the gold surface. The sample was deposited in form of few hundred nanometers thick film and was not investigated in more detail. The successful deposition was confirmed by X-ray absorption spectra. The

XMCD and μ-SQUID measurements showed no indication of slow relaxation of magnetization and thus, the SMM properties of bulk material were quenched by the deposition [69].

L. Spree et al published chemically derivatized $Tb_2@C_{80}(CH_2Ph)$ SMM where a pyrene function group served as an anchor for deposition on a graphene and graphite surface by forming π-π interaction between pyrene and the surface[11]. The comparison of magnetic hysteresis (obtained by XMCD) for bulk and hybrid material showed only slight worsening of the magnetic properties upon deposition and the hybrid material still showed magnetic hysteresis. The blocking temperature of the hybrid material was 28 K and for the bulk 29 K. The AFM showed thickness of the hybrid material to be 1.8-2 nm (**Figure 29**).
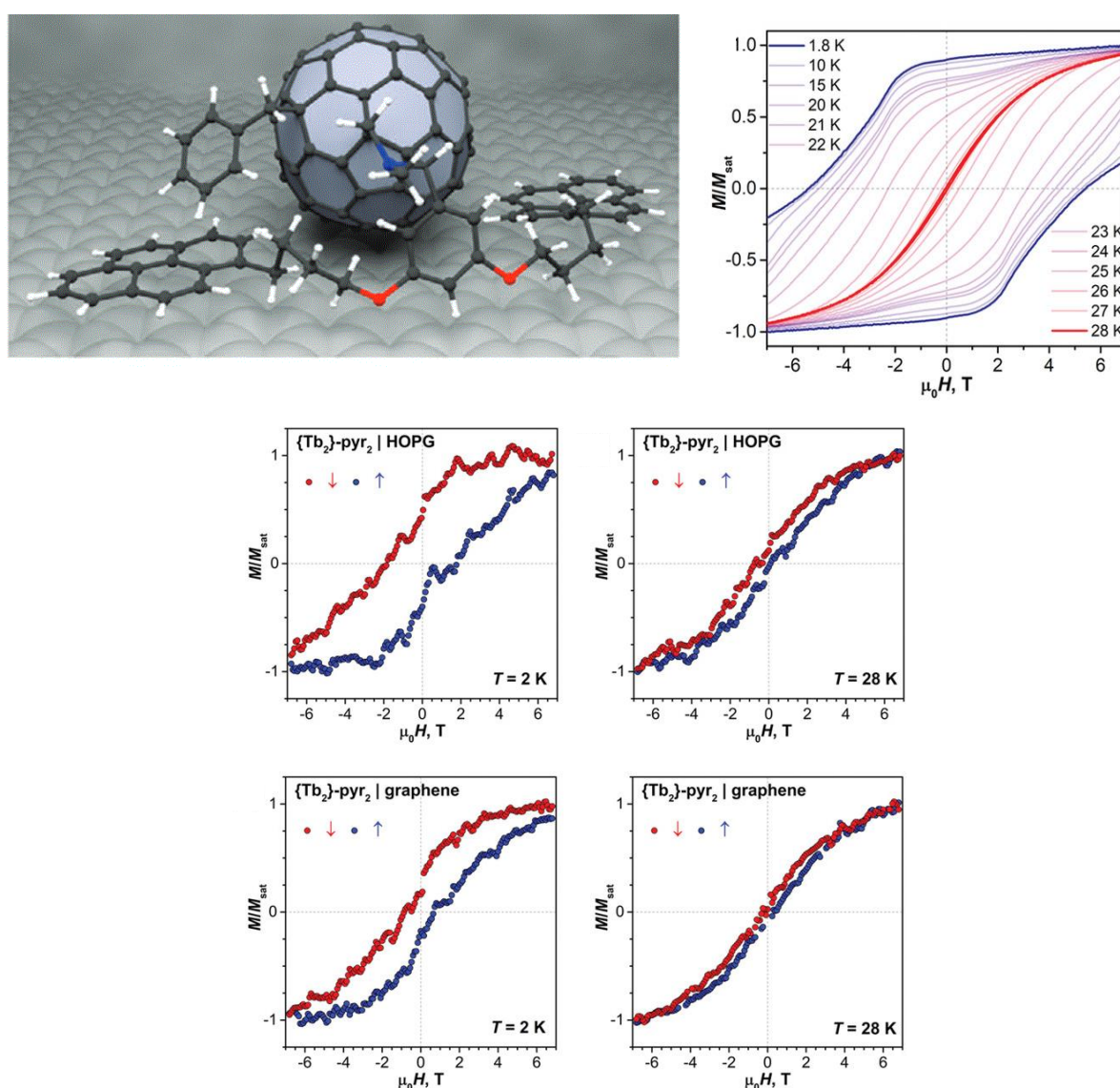
Figure 27: Molecular Dynamics simulation of possible way of deposition of $Tb_2@C_{80}(CH_2Ph)$ (up left), magnetic hysteresis at different temperatures in bulk $Tb_2@C_{80}(CH_2Ph)$ (up right), magnetic hysteresis measurements of $Tb_2@C_{80}(CH_2Ph)$ deposited on graphene or highly oriented pyrolytic graphite (HOPG) at 2 and 28 K[11].

Chemical tailoring is often used for modifying coordination compounds for depositions. As shown in the case of Spree above, introducing aromatic rings allows to induce formation of the π-π interactions of aromatic ring of ligand with graphene layer or carbon nanotubes and anchors the structure on the surfaces. Such an approach was also published by Klatskaya et al[60] who prepared modified derivate of the [TbPc2]. Authors modified the ligand with peripheral aliphatic chains and with functional group containing pyrene which serves as an anchor to a single walled carbon nanotubes via formation of π-π interactions. μ-SQUID measurements revealed that the hybrid material showed higher blocking temperature than bulk material and the magnetic hysteresis loop was more open for the hybrid material than for the bulk. (**Figure 30**). This improvement in magnetic properties was ascribed to significant decrease in intermolecular interactions upon deposition that were partially quenching the SMM properties in the bulk phase.
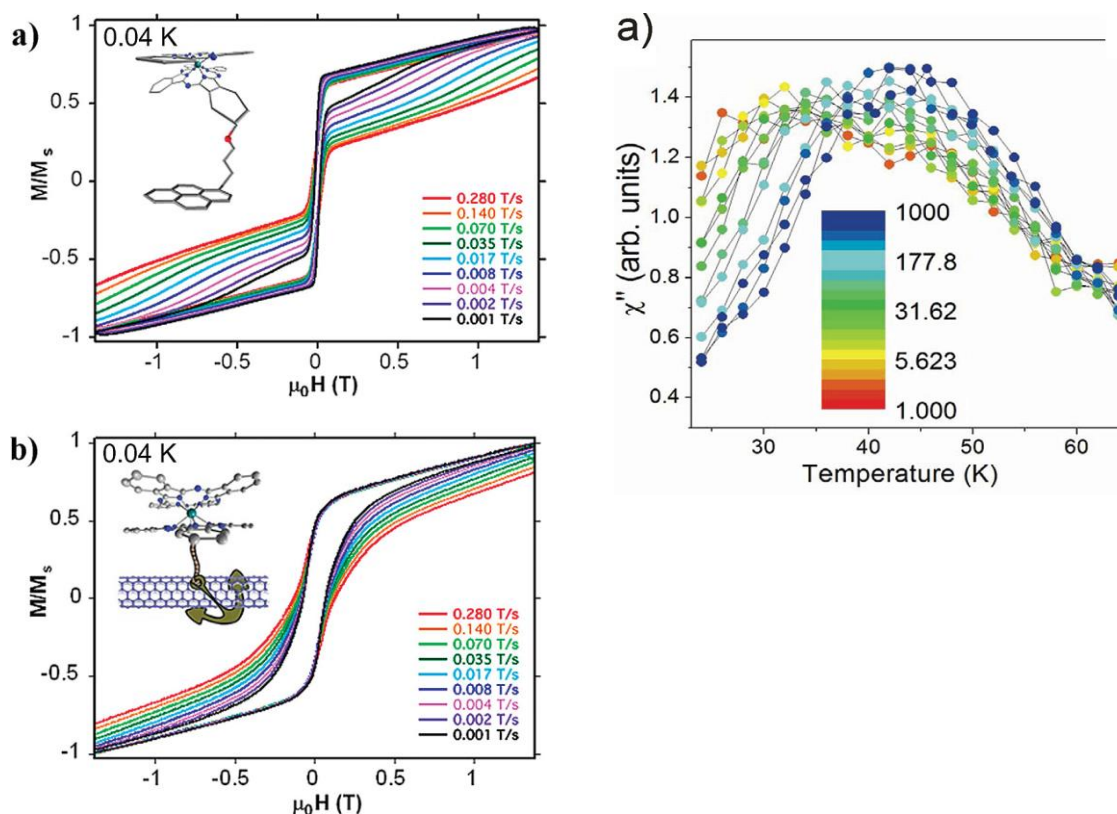
Figure 28: Comparison of magnetic hysteresis loops of bulk and deposited complex (left) and its temperature depended AC measurements after deposition[60].

Cervetti et al[70] reported [Fe4(L5)2(dpm)6] where L5 = 2-hydroxymethyl-2-(4-(pyren-1-yl)-butoxy)methylpropane1,3-diol and dpm=dipivaloylmethane and deposited this compound on the graphene layer. The two pyrene functional groups formed π-π interactions with the surface. AFM showed thickness of the deposited layer to be 1.8 nm. AC susceptibility

measurements revealed that the spin-graphene interaction in the hybrid material led to significant decrease of the relaxation time as a stronger QTM took place in the hybrid system (**Figure 31**).
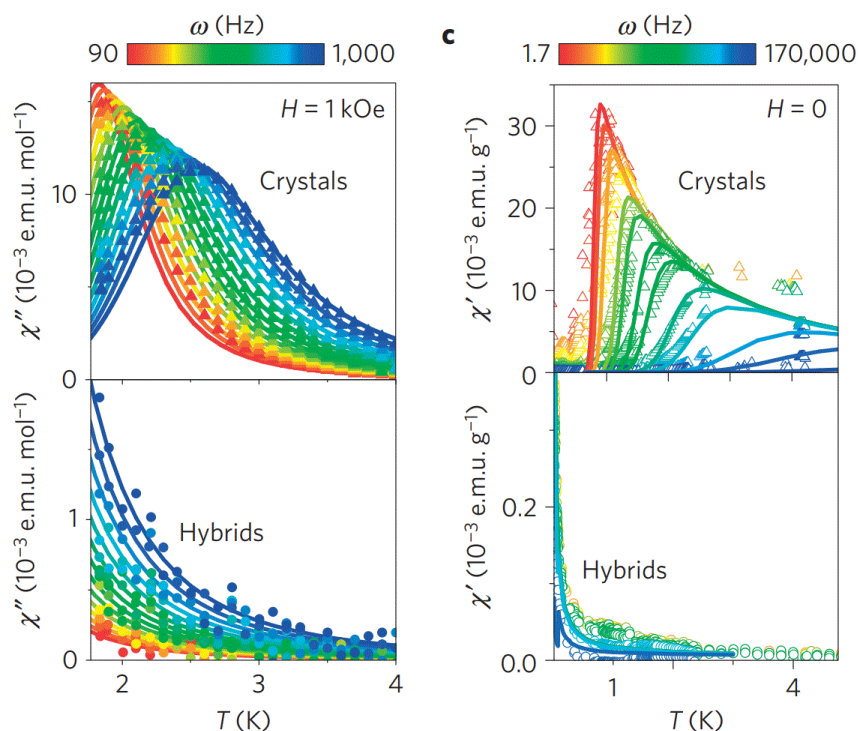
Figure 29: Temperature and frequency dependent AC susceptibility data for[Fe$_4$(L)$_2$(dpm)$_6$] in bulk (top) and after deposition in hybrid materials (bottom)[70].

Additionally, several other reports on deposition of SMMs or other suitable compounds have been reported in the literature showing a good potential to control the organization of molecular structures on surfaces[71,72]. Several works have been reported also by members of the MOTeS research group[73–75].

4. Methodology and Theoretical background

In this chapter are discussed analytical methods important for this thesis and for SMMs/SIMs and their deposition on surfaces. Section 4.1 focuses on magnetization studies of SMMs/SIMs and the theory of the measurements. In the section 4.2 is discussed geometry of coordination compounds of Co(II) and their crystal structure. The analysis of Co(II) SIMs by Electron Paramagnetic Resonance is discussed in section 4.3 and their deposition on surfaces in section 4.4.

4.1   Magnetization Studies

The two main magnetometry techniques were used in this thesis and also in general in the research of Single Molecule Magnets are PPMS (**P**hysical **P**roperties **M**easurement **S**ystem) and SQUID (**S**uperconducting **Qu**antum **I**nterference **D**evice). They are very often combined into MPMS (**M**agnetic **P**roperties **M**easurement **S**ystem). More specifically, the DC susceptibility measurements were gathered from a VSM (**V**ibrating **S**ample **M**agnetometry) experiment. The VSM was invented by Simon Foner in 1955 and the principle remains same. The sample is placed in between the pick-up coils and small magnetic field is applied and the magnetization of the sample is aligned with the magnetic field. As the sample is moved it induces a magnetic field of its own. The moving magnetic field than induces an electric current in the pick-up coils. This induced current is then proportional to the magnetization of the sample and its amount. Usually, VSM is placed in the cryochamber, and it is possible to study the dependence of magnetic moment on temperature. Such dependency allows to observe such phenomena as Curie and Neél temperatures, ferro- or antiferro magnetic interaction within the sample or even ZFS. The last mentioned is the point of interest in the case of SMMs/SIMs. VSM also allows isothermal measurements while the external magnetic field is being swept. With the presence of superconducting magnet a high magnetic fields such as 9 T can be used.. The same principle of the current induction provides information about the magnetization in the whole magnetic field range. Such data are usually used to study magnetic hysteresis or to observe deviations from the ideal paramagnetic behavior described by the Brillouin function. The obtained magnetic moment μ or magnetization of sample in both measurements modes is processed to molar magnetization M_{mol} (A·m^2·mol^{-1}) and effective magnetic moment if preferred (**Equation 8-10**).

$$M_{mol} = \frac{\mu}{1000} \frac{M_r}{m} \qquad\qquad \textbf{(8)}$$

*M*r is molar mass, *m* is mass of a sample (g)

$$\chi_{mol} = \mu_0 \left(\frac{M_{mol}}{B}\right) \qquad (9)$$

χ_{mol} is molar susceptibility ($m^3 \cdot mol^{-1}$), μ_0 is permeability of vacuum, *B* is magnetic field (T)

$$\mu_{eff}/\mu_B = \sqrt{\frac{3k}{N_A \mu_0 \mu_B^2} \chi_{mol} T} = 798\sqrt{\mu_{mol} T} \qquad (10)$$

μ_{eff} is effective magnetic moment, μ_B is Bohr magneton, *k* is Boltzman constant ($J \cdot K^{-1}$), N_A is Avogadro's number (mol^{-1}), *T* is temperature (K)

Using the efollowing Spin Hamiltonian it is possible to extract ZFS parameters from the magnetic measurements:

$$\hat{H} = D\left(\hat{S}_z^2 - \hat{S}^2/3\right) + E\left(\hat{S}_x^2 - \hat{S}_y^2\right) + \mu_B B g \hat{S}_a \qquad (11)$$

The first term reflects axial magnetic anisotropy (*D*), the second term rhombicity (*E*) and the last one is the Zeeman term describing interaction of the paramagnetic species with magnetic field.

The defining property of SMMs/SIMs is slow relaxation of magnetization. This process can be studied only by using SQUID magnetometer. This method is very sensitive and allows to study very small magnetic fields (down to 10^{-14} T). This is possible thanks to Josephson junctions placed in the superconducting loops. Josephson junctions consist of two superconductors separated by a barrier – insulator, non-superconducting metal or physical obstruction. In such junctions a Josephson effect takes place, named after B. D. Josephson. Josephson junction allows to study very small voltage which is resulting from the sample magnetization and Josephson effect. During the measurement the AC magnetic field with changing amplitude and phase is generated. The final outcomes of the measurement are frequency and temperature dependent components of alternating susceptibility, namely in-phase χ' and out-of-phase χ'' components. χ'' is zero for paramagnetic materials and becomes non-zero if magnetic phase is changed (**Equation 12**). If the is alternating susceptibility is delayed behind the phase of magnetic field a slow relaxation of magnetization is present.

$$\chi_{AC} = \chi' \cos(\omega t) + \chi'' \sin(\omega t)$$

$$\chi' = \chi cos\theta, \chi'' = \chi sin\theta \qquad \qquad (12)$$

$$\chi = \sqrt{\chi'^2 + \chi''^2}$$

Θ is phase angle of the delay

The SQUID data can be additionally processed by using Arrhenius law to study the contribution of relaxation processes and to extract the relaxation time τ (**Equation 13**)*.*

$$\tau = \tau_0 e^{-U_{eff}/k_B T} + CT^n + \tau_{QTM} \qquad \qquad (13)$$

The first term represents Orbach process, the second Raman and the third represents QTM

4.2   Co(II) Complexes and Crystal Structure

Majority of coordination compounds discussed in this thesis contain the Co(II) central atom in their structures. Among the 3d elements, Co(II) is very good central atom for potential SIMs as its high spin coordination compounds possess strong SCO (**S**pin-**O**rbit **C**oupling), which gives rise to large magnetic anisotropy. The high spin character of coordination compounds is given by the strength and symmetry of their ligand field and these characteristically splits the d-orbitals (**Figure 32**). The ground term for Co(II) is ^4F and it is further split by the geometry and strength of the ligand field. The respective ground terms for various geometries are shown in **Figure 33** and **34**.
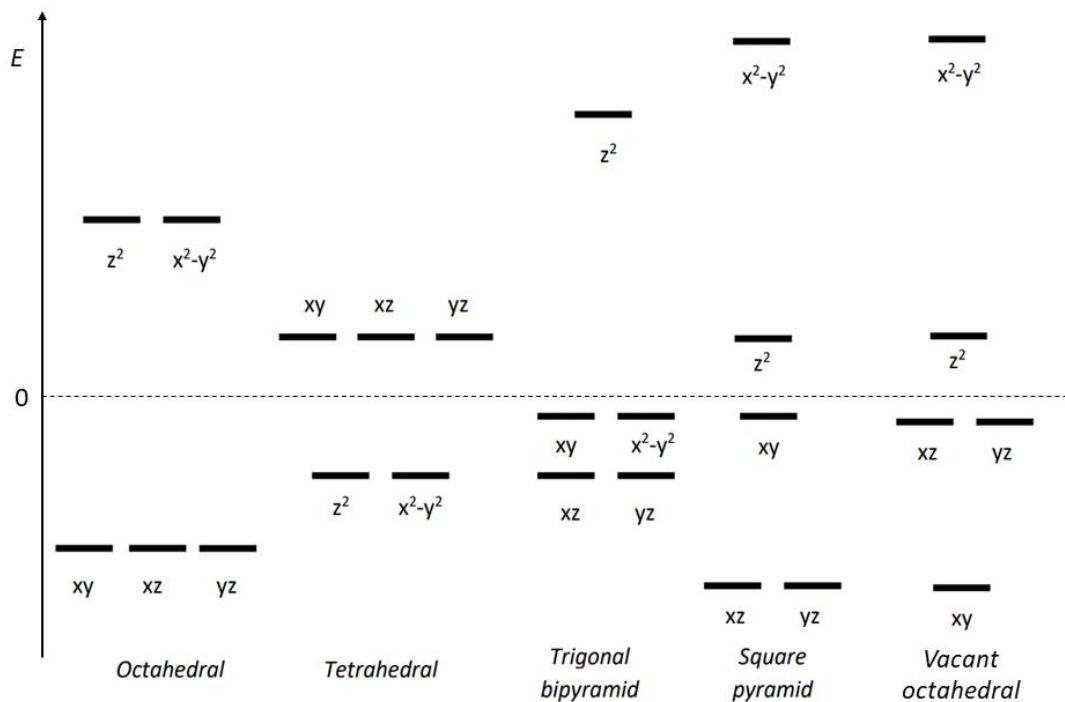
Figure 30: Splitting of d-orbitals in different geometry of coordination polyhedra

As can be seen from the above-mentioned relationship between the ligand field strength, symmetry and electronic structure of the complex molecules, the information about the geometry of the coordination polyhedron and the crystal structure in general is crucial for magnetic studies. The most reliable way of learning about the crystal structure of a compound is by X-ray diffraction. As the X-ray wavelength is similar to the distance d of the crystal planes it is diffracted in a characteristic direction for each studied crystal. The diffraction occurs when radiation of a given wavelength λ irradiates crystal under a given angle θ and as a result the scattered radiation is constructively interfered. This is described by the Bragg's law (**Equation 14**). Such diffraction produced diffraction pattern, which contains information about electron density in the crystal. This principle applies in both Single crystal and Powder diffraction techniques, though, each has different experimental setup.

$$n\lambda = 2d sin\theta \qquad (\mathbf{14})$$

For SMMs/SIMs it is very important to determine the magneto-structural relationship and thus to precisely know bond lengths and angles inside the coordination sphere. Most importantly, it allows us to determine the level of distortion from the ideal shape of coordination polyhedron. There are several ways to determine distortion from the different shape. The Addison parameter τ offers simple description for pentacoordinate complexes as it spans from

0 (Square pyramid) to 1 (Trigonal pyramid) resulting from subtraction of two biggest angles divided by 60[76]. To gather more precise insights into the geometry of coordination polyhedral one needs more complex tools such as SHAPE[77] software. Single-crystal X-Ray diffraction data bring also essential information for the theoretical calculations used in this thesis such as DFT (Density Function Theory) and CASSCF (Complete Active Space Self Consistent Field).
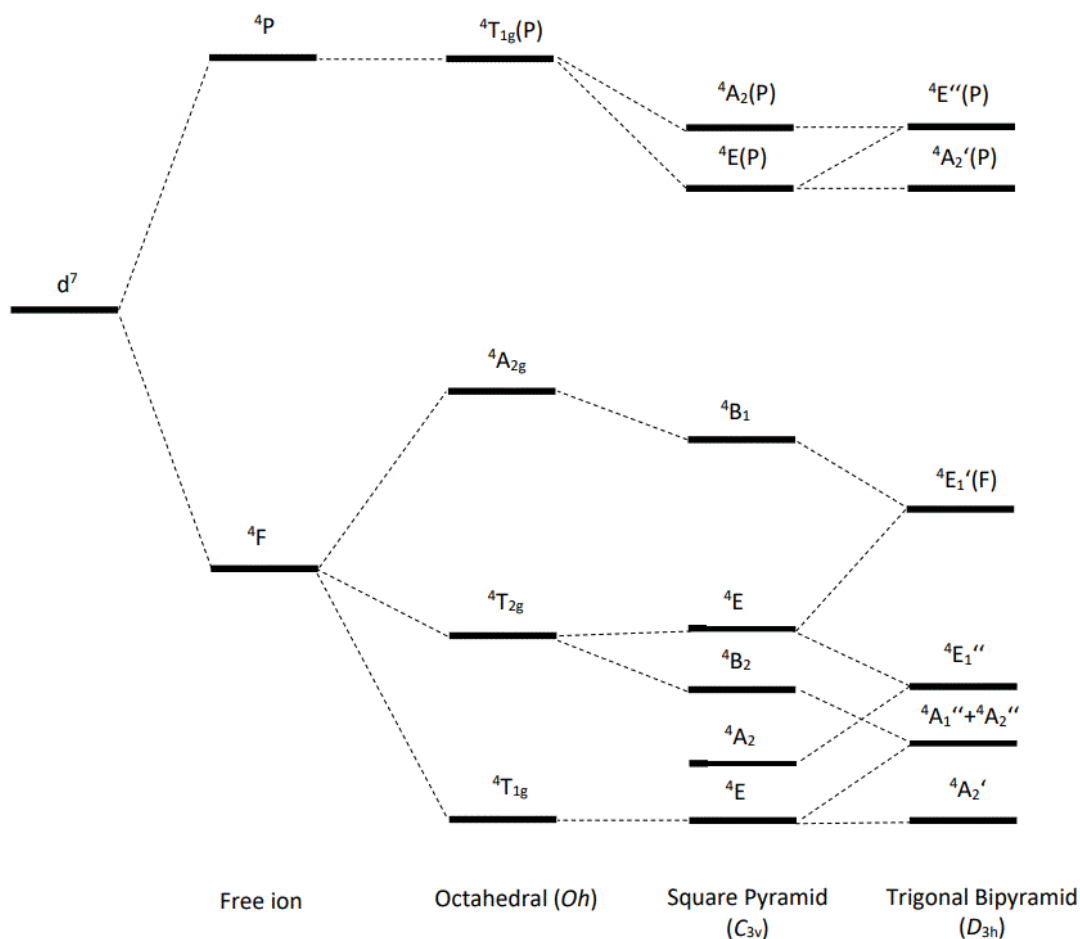
Figure 31: Splitting of the crystal field terms of d^7 systems.
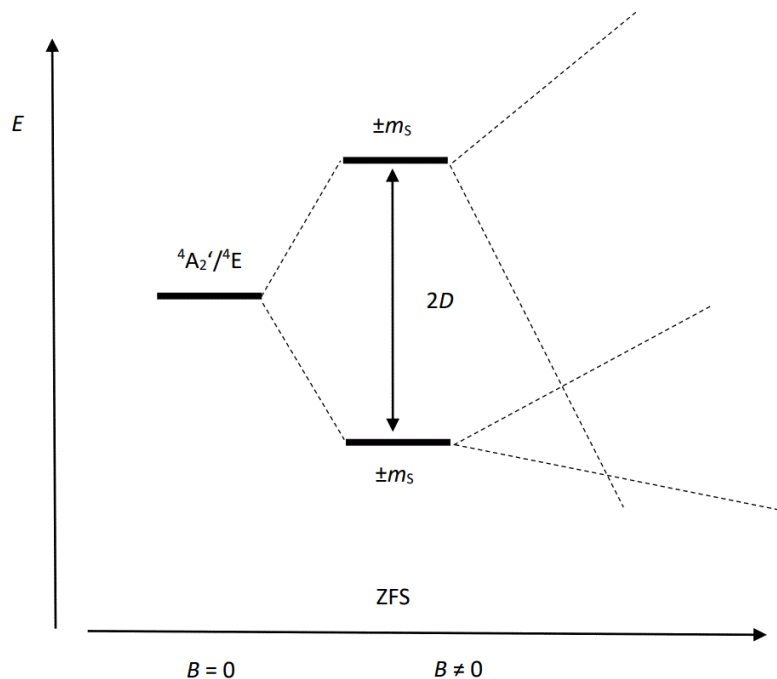
Figure 32: Splitting of the ground term due to ZFS.

4.3 Electron Paramagnetic Resonance

All SMMs/SIMs possess a non-zero total spin S as they contain unpaired electrons in they valence shell orbitals d or f. Spin quantum numbers follows the rule $m_S = -S, (-S+1),\ldots,+S$. One of the conditions for a coordination compound to be considered SMMs/SIMs is that S has to be bigger than $S=1/2$ with no upper limit to spin value. Low spin systems of Ni(II) or Fe(II) are common examples of SIMs with spin $S=1$. Other common examples of SIMs are high spin Co(II) having $S=3/2$ or coordination compounds of lanthanides in oxidation state III with even higher number of electrons in f orbitals. In the systems with $S > \frac{1}{2}$ where the terms are splitted by the crystal field is observed further splitting of the energy at zero magnetic field which is know as ZFS (**Z**ero **F**ield **S**plitting) which occurs in such systems as SIMs (**Figure 34**). The result of ZFS is that the m_S states are split even in the absence of external magnetic field. ZFS can be described by D and E parameters, D being the axial and E the transversal component of the magnetic dipole-dipole interaction in between the m_S states (**Equation 15**).

$$\mathcal{H}_{ZFS} = D\left[S_Z^2 - \frac{S(S+1)}{3}\right] + E(S_X^2 + S_Y^2) \tag{15}$$

The energy of m_S states depends on the value and sign of the D parameter and thus is characteristic for every SIM/SMM and their central atom. Considering an example of high spin SIM with Co(II) as central atom and $D < 0$, the spin is $S=3/2$ in many geometries of coordination

polyhedra for orbitally degenerate systems. In axial symmetry of magnetization the $D_{XX} = D_{YY}$ and thus $E = 0$ (**Equation 16**).

$$D = \frac{3D_{ZZ}}{2} \quad E = \frac{|D_{XX}-D_{YY}|}{2} \tag{16}$$

Where S_X, S_Y, S_Z are operators of spin projection along corresponding axis, D_{XX}, D_{YY}, D_{ZZ} are terms of magnetic anisotropy tensor

The Kramers doublets for this system are $m_S = \pm 1/2, \pm 3/2$ because of the presence of ZFS this levels will be split and due to the sign of D the state $m_S = \pm 3/2$ will be placed lower in energy and $\pm 1/2$ higher in energy. The difference in energy between the Kramers doublets corresponds to $2D$. However, in general case the energy is proportional to D.

Upon applying external magnetic field, the $\pm m_S$ levels are further split which is caused by Zeeman interaction. The larger the magnetic field the larger is the energy gap between them. The electrons occupying these levels can be excited by outside source in energy and they will occupy levels with higher energy. If a resonance condition (**Equation 17** and **Figure 35**) is met the electrons are continually excited and transition among $\Delta m_S = \pm 1$ can be observed.

$$\Delta E = h\upsilon = g_e \mu_B B_{ext} \tag{17}$$
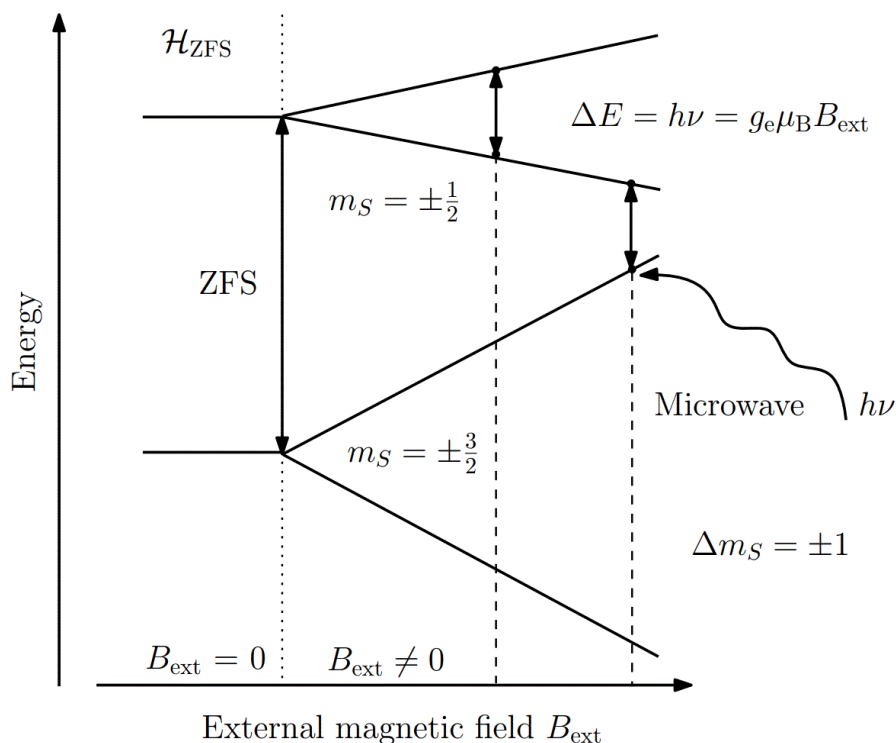
Figure 33: Depiction of ZFS, splitting in external magnetic field and the resonance condition. Adapted from [78].

This principle of resonance is applied in HF-EPR (**H**igh-**F**requency **H**igh-**F**ield **E**lectron **P**aramagnetic **R**esonance) or EPR in general. EPR is especially suitable technique to study systems with ZFS such as SIMs thanks to its precise determination of ZFS parameters and very high sensitivity. EPR can be even used to study hybrid materials of SMMs deposited on surfaces as few groups proved[79–81] it and special sample holders for study of such hybrid systems by EPR are being developed[82]. From the definition of resonance condition, the determination of ZFS using HF-EPR is limited by the frequency of microwave source (up to 1 THz in our custom-made setup) and the magnetic field produced by superconducting magnet. For SMM/SIM possessing very high D (e. g. D = -100 cm^{-1}) it is impossible to use this technique and EPR has to be complemented by HF-FTIR (**H**igh-**F**ield **F**ourier **T**ransform **I**nfra-**R**ed) spectroscopy (**Figure 36**).
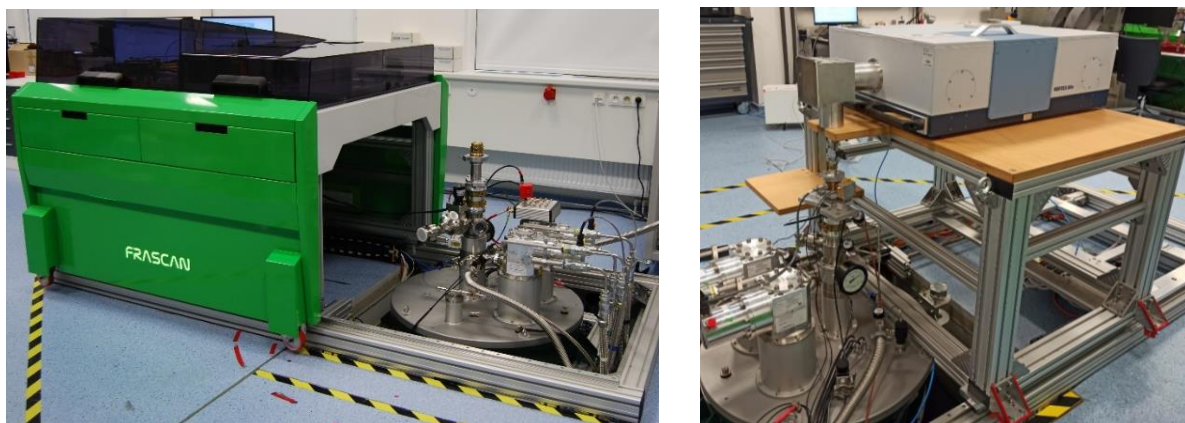
Figure 34: Custom build HF-EPR FRASCAN (left) and HF-FTIR (right) in the MOTeS group at CEITEC BUT.

4.4   MOTeS Sublimation Chamber

One of the approaches to deposit coordination compounds on surfaces is a thermal sublimation. Sublimation chamber was designed and built by Dr. Jakub Hrubý for this purpose in MOTeS group. This chamber allows deposition of bulk powder samples onto various substrates in high vacuum and allows the user to control the temperature. The thickness of deposited layer on substrate is controlled by quartz crystal microbalance – which is a sensitive quartz crystal coated by gold with specific resonance frequency that changes based on its mass difference caused by sublimated material. The flux of sublimation can be controlled by temperature or completely stopped by shutter, which presents barrier between crucible and substrates. For heating of the samples, serve different crucibles – quartz, carbon or h-BN. (**Figure 37**).
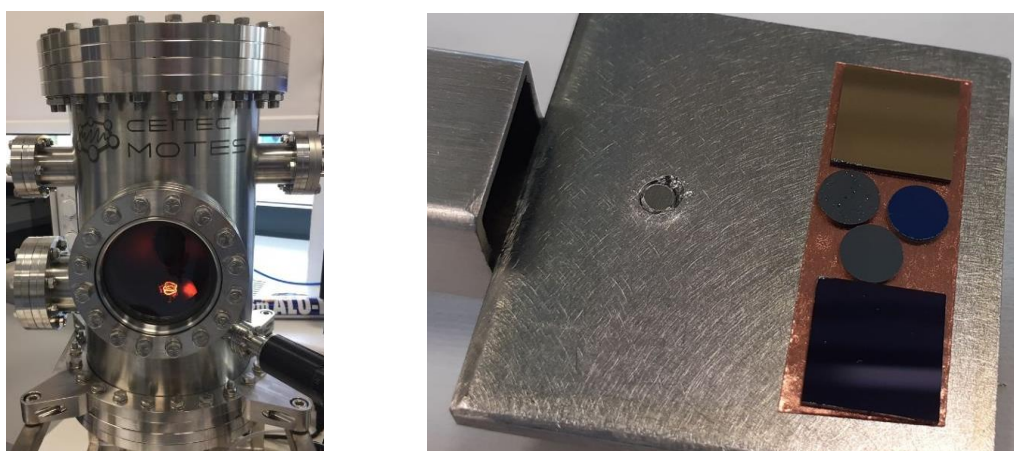
Figure 35: MOTeS Sublimation Chamber (left), various substrates loaded for deposition (right).

4.5 List of used Experimental Methods

The coordination compounds prepared in this thesis were analysed by the following experimental methods:

Structural analysis: The crystal structures were obtained using X-ray diffractometer XtaLAB Synergy-i (Rigaku) with micro focused X-ray source PhotonJet-i (Cu) and detector HyPix Bantam. The powder diffraction data were obtained using XRPD MiniFlex600 (Rigaku, Tokyo, Japan).

Magnetic measurements: Data for compounds **2b** and **3d** were obtained using VSM Cryogenic Limited Magnetometer (Cryogenic Limited, London, UK). The temperature and field-dependent magnetic data were studied as finely grinded powder dispersed in eicosane and fixed in a plastic straw. Data of the remaining samples were obtained using PPMS Quantum Design (Quantum Design Inc., San Diego, CA, USA). The temperature and field-dependent magnetic data were studied as finely grinded powder samples pressed into QD capsule. The AC data for compound **3d** were obtained using MPMS XL7 SQUID magnetometer (Quantum Design Inc., San Diego, CA, USA).The obtained magnetic data were analysed by EasySpin[83] a module for Matlab and fitted to Spin Hamiltonian. The data for compound **1a** were analysed using Poly_Aniso software[84–86].

HF-EPR measurements: HF-EPR data were collected using Frascan spectrometer (MOTeS research group, CEITEC BUT, Brno, Czech Republic) (**Figure 36**). The data were analysed by EasySpin[83] a module for Matlab and fitted to Spin Hamiltonian.

Theoretical calculations: The magnetic exchange was investigated by DFT calculations (Broken Symmetry DFT). The ZFS parameters have been calculated using CASSCF/NEVPT2 which were utilised to calculate all energy levels resulting from $3d^7$ electronic configuration with the ORCA 4.2 computational package[87,88]. The ab initio ligand field theory (AILFT) was used to calculate the splitting of d-orbitals[89].

Spectroscopy: The XPS spectra have been collected with X-ray Photoelectron Spectroscopy Axis Supra (KRATOS-XPS) (Kratos, Manchester, UK) and Raman spectra with IR Raman Bruker RFS 100 (IR-RAMAN) (Bruker, Billerica, Massachusetts, USA). The data were analyzed using CasaXPS software [90].

5. Obtained Results

5.1 Dy(III) Coordination Compounds

As was discussed in section 3.1, SMM/SIM of Dy(III) with Mannich type of ligands are uncharted territory. Moreover, this type of the ligands impose trigonal symmetry, which can be used in preparation of less common coordination numbers (e.g. 6 or 7) if the ligands contain sterically demanding substituents (e.g. $-CH(CH_3)_2$, $-C(CH_3)_3$,).

For this thesis a series of organic ligands were prepared via Mannich reaction and eight of them were successfully isolated (**Figure 38**). It was intended to prepare tetradentate ligands with either three O-donor and one N-donor atom or two O-donor and two N-donor atoms. For these structural reasons were chosen also reactants such as glycine, 2-picolylamine and 4-picolylamine and were reacted with formaldehyde and various derivates of phenol. It was expected that upon reaction with dysprosium salts complex the precursor complexes with the coordination number 8 or 9 will be formed as Mannich ligand provides four coordination bonds and NO_3^- or solvent ligands may provide up to four coordination bonds. The syntheses of the following complexes were attempted, the expected compositions are outlined here, although the possible dimerization and other combinations (protonation *vs*. presence of the NO_3^- and solvent ligands) cannot be excluded: $[Dy(LX)(HLX)]$, $[Dy(HLX)(NO_3)_2]$, $[Dy(LX)(solv)_{2-3}]$ (where $H_3LX =$ is one of the prepared Mannich ligands). Such compounds could be further used after introduction of appropriate bi- or tridentate blocking ligand (e.g. 2,2'-bipyridine-N-oxide, or tridentate Schiff base ligands originating from condensation of salicylaldehyde derivatives and ortho-aminophenols) for synthesis of the target six or seven coordinate Ln complexes. Even though that many attempts to synthesize coordination compounds with the H_3LX ligands were performed, including extensive screenings of the different basicity (Dy:base from 1:0 up to 1:10) and reactant ratios (Dy:H_3LX from 1:1 up to 1:4), the chemical identification of the prepared products was never successful. Also, various hydrothermal reaction conditions were tested, but the performed reactions did not bring any success and typically resulted in forming insoluble white powder product. Characterization of such powders never led to the confirmation of the chemical identity.

Following these attempts, the rather complex ligands were replaced by simpler trigonal ligand triisopropylamine (H_3tipa). H_3tipa possesses trigonal structure and three O-donor and one N-donor ligand which is suitable for coordination of Dy(III). As shown in section 3.1 coordination of simple trigonal aliphatic ligands to Dy(III) usually lead to coordination number

9. Extensive series of reactions of H_3tipa and Dy(III) salts with varying ration of used base to modify the deprotonation of the H_3tipa were performed in attempt to prepare – [Dy(H_2tipa)$_2$Cl], [Dy(H_2tipa)(Htipa)], [Dy(H_2tipa)(Htipa)(NO$_3$)], [Dy(tipa)(NO$_3$)$_2$]. The attempts were unsuccessful or resulted in isolation of dimeric coordination compound [Dy$_2$(Htipa)$_2$(NO$_3$)$_4$]·2Et$_2$O – **1a**.
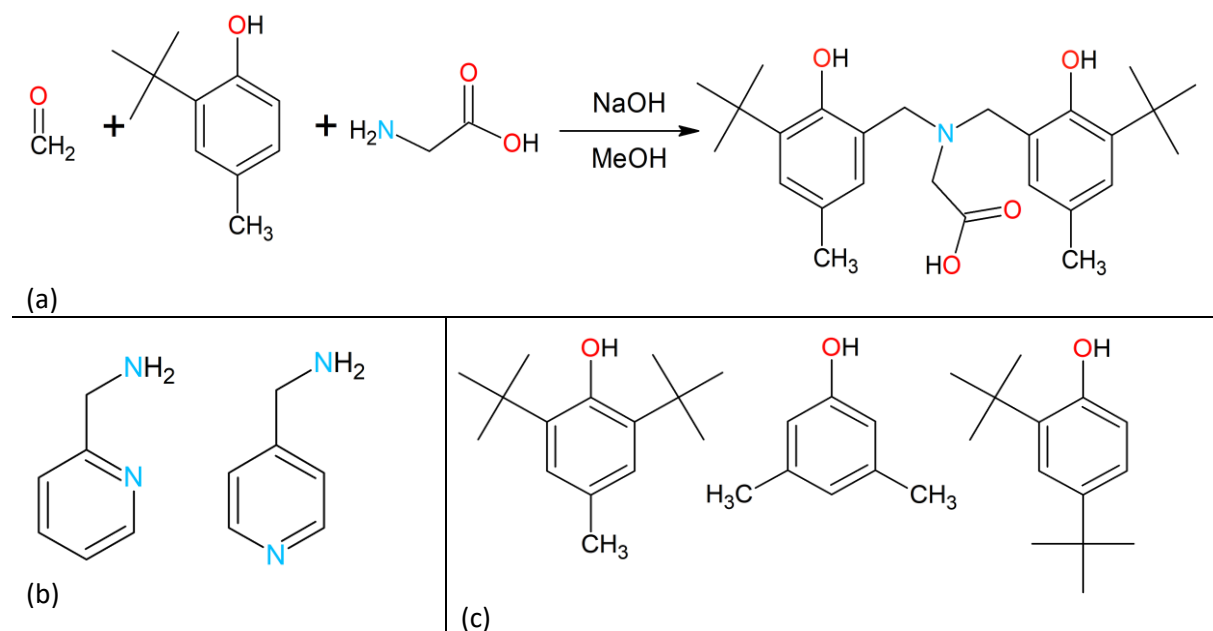
Figure 36: (a) chemical synthesis of mannich type ligand. (b) glycin was replaced by 2-picolylamine and 4-picolylamine. (c) 2-tert-butyl-4-methylphenol was replaced by 2,6.di-tert-butyl-4-methylphenol, 3,5-dimethylphenol and 2,4-di-tert-butylphenol.

Synthesis of [Dy$_2$(Htipa)$_2$(NO$_3$)$_4$]·2Et$_2$O (**1a**) was done as follows: 1 mmol of Dy(NO$_3$)$_3$·7H$_2$O was dissolved in 5 ml of MeOH and it was mixed with a solution of 2 mmol of H$_3$tipa in 10 mmol of MeOH. This solution was stirred at room temperature for 24 hours, filtered with paper filter and crystalized by slow diffusion of diethylether. Colorless crystals formed after two weeks (**Figure 39**).
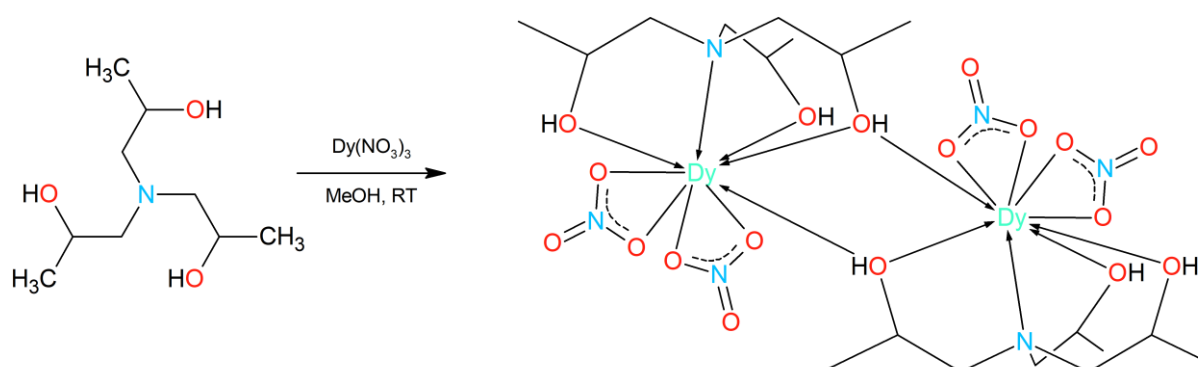
*Figure 37: Synthetic scheme for preparation of **1a**.*

Crystal structure:

Complex $[Dy_2(Htipa)_2(NO_3)_4] \cdot 2Et_2O$ crystalizes in the $P2_1/n$ space group. Both Dy(III) central atoms are coordinated each by one tetradentate ligand H_3tipa forming metal-ligand (ML) bond lengths between the central atom and one nitrogen ($d(Dy-N) = 2.596(3)$ Å) and three oxygen ($d(Dy-O) = 2.278(2), 2.405(2), 2.408(2)$ Å) donor atoms. The H_3tipa ligand function also as the bridging ligand in the dimer as each Dy is coordinated by one oxygen atom from the adjacent H_3tipa ligand ($d(Dy-O) = 2.244(2)$ Å). Additionally, each Dy is coordinated by two nitrate ligands in a bidentate manner ($d(Dy-O) = 2.488(2), 2.495(2), 2.503(2), 2.521(2)$ Å) (**Figure 40**). The intramolecular Dy⋯Dy distance is 3.709(3) Å.

The unit cell contains two diethylether molecules per complex molecule, which is stabilized in the crystal structure by hydrogen bond formed between the oxygen atom from diethylether and hydroxy group of Htipa ($d(O \cdots H-O) = 2.727(3)$ Å).
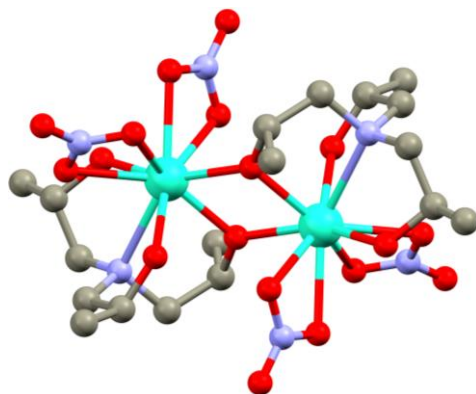
Figure 38: Crystal structure of $[Dy_2(Htipa)_2(NO_3)_4] \cdot 2Et_2O$. Grey (C), light blue (N), azure (Dy), red (O).

Magnetic properties and Theoretical calculations:

The effective magnetic moment (μ_{eff}/μ_B) is significantly decreasing with decreasing temperature from about 30.71 at 300 K down to 32.33 at approximately 20 K where follows clear and sudden drop of μ_{eff}/μ_B to 15.68 at 2.99 K. These values are expected for Dy(III) dimer SMM (14.17μ_B). Using CASSCF calculation together with fitting the magnetic data the exchange interaction between both central atoms was obtained $J = -0.409$ cm^{-1} (**Figure 41**).
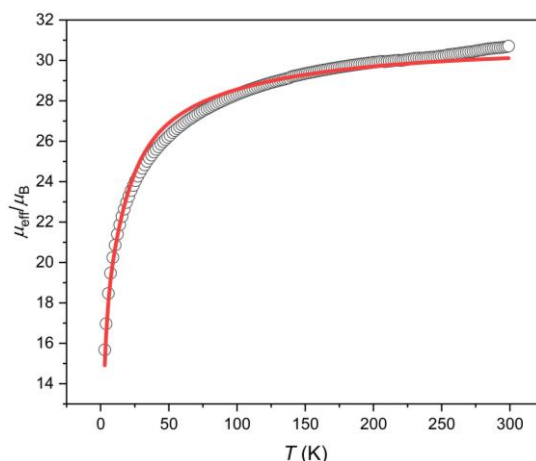
*Figure 39: Temperature dependent magnetic measurement of **1a**. Black circles are data and red line is fit.*

Using CASSCF theoretical calculations it was possible to determine the value of spin-reversal barrier for single Dy(III) centre and the probability of relaxation processes. The relatively high probability of QTM suggests that compound **1a** will be field induced SMM (**Figure 42**).
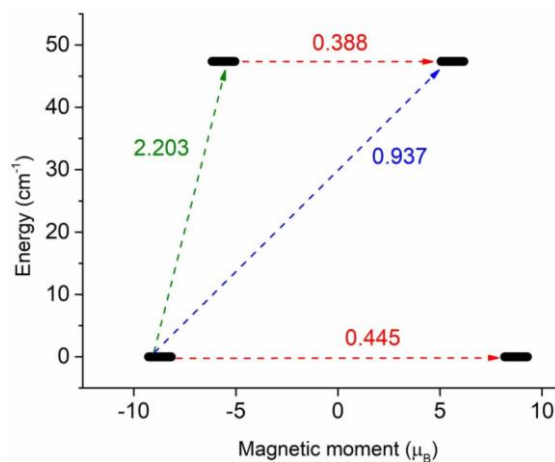
*Figure 40: CASSCF calculation of the spin-reversal barrier of **1a**. Red dashed lines are QTM. Blue dashed line is thermally assisted QTM process and green dashed line is Orbach process of relaxation. The numbers indicate probability.*

5.2   Co (II) SIMs with Tripodal Ligand Trenb

The complexes with the ligand trenb (tris(2-aminoethyl)amine) were chosen due to their specific molecular geometry. First, the trenb ligand partially encapsulates the Co(II) central atom and allows coordination of only one additional monodentate ligand, resulting thus in coordination number 5. The geometry of such coordination polyhedron is close to trigonal bipyramidal and such Co(II) complexes have proved to be interesting SIMs[40,41,43]. Next, upon a formation of the complex, three phenyl functional groups form kind of tripodal geometry, which after deposition may be oriented towards the substrate (and can possibly further rotate) enabling formation of the π-π interactions between the substrate (e.g. graphene). Such geometry

can help and improve self-assembly distribution of the complex molecules on the surface of substrate [61,63,91–93].

Series of 13 coordination compounds have been synthetized and resynthesized (**Figure 43**). The crystal structures of two of these compounds have been reported earlier - [Co(trenb)N$_3$]Cl by H. Jiang et al.[94] and [Co(trenb)(NCS)]Cl by Y. Xie et al.[95]. Furthermore, part of a series was partially described in my master's thesis[96]. Herein, this series was fully structurally and magnetically characterized and used for deposition on the selected surfaces with goal to study such hybrid systems by HF-EPR. Four bulk samples have been studied by HF-EPR and the obtained ZFS parameters have been compared with the magnetic measurements and theoretical calculations. Selected samples have been studied by Raman spectroscopy and XPS followed by several attempts for wet and thermal depositions on gold, SiO$_2$ and graphene substrates.
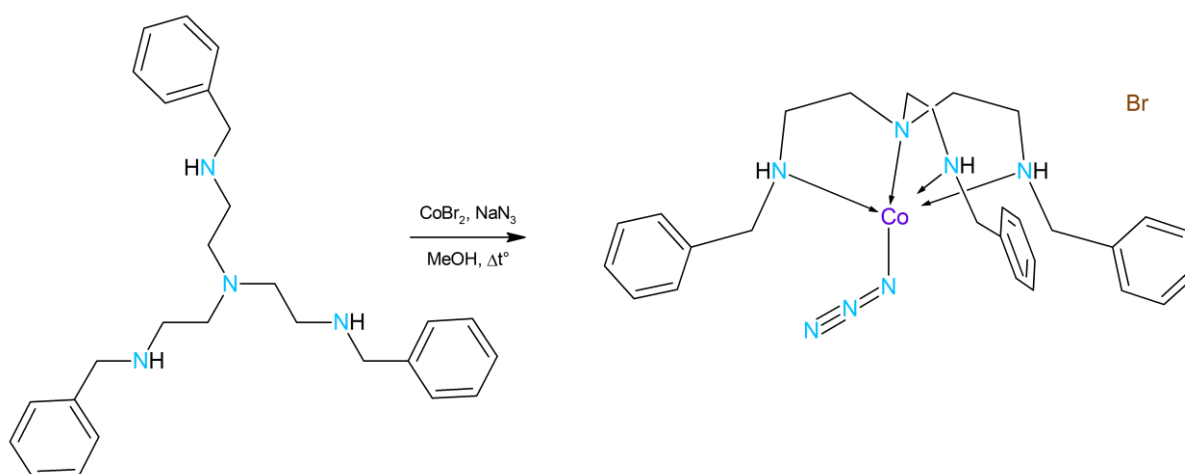
Figure 41: Synthetic scheme for preparation of 2b.

The substrates have been chosen based on the chemical formula of the samples and their geometrical orientation (*vide supra*) given by the crystal structure. The presence of the NCS$^-$ ligand offers a possibility for anchoring the coordination compound on a gold surface due to very high mutual affinity of the gold and sulphur atoms and to create a self-assembly pattern for the samples allowing to control the distribution of SIMs as it is necessary for bottom-up preparation of functional hybrid systems[97–100].

A complete series consists of 13 coordination compounds: [Co(trenb)N$_3$]Cl (**2a**), [Co(trenb)N$_3$]Br (**2b**), [Co(trenb)(NCS)]Cl·MeOH (**2c**), [Co(trenb)(NCS)]Br (**2d**), [Co(trenb)(NCSe)]Cl (**2e**), [Co(trenb)(NCSe)]Br (**2f**), [Co(trenb)(NCO)]Br (**2g**),

[Co(trenb)Cl]Cl (**2h**), [Co(trenb)Br]Br (**2i**), [Co(trenb)Cl]Br (**2j**), [Co(trenb)Br]I (**2k**), [Co(trenb)Cl]I (**2l**), [Co(trenb)I]I (**2m**).

Crystal structures:

The crystal structure of samples **2g**-**2j** and **2l** could not be resolved into good publication quality due to low quality of the crystals. Nevertheless, the quality was high enough to confirm coordination sphere and distinguish which halogen atom is coordinated and which remains as a counter ion in the crystal structure.

Compounds **2a**-**2f** are isomorphous and they crystalize in the orthorhombic Pbca space group. Compound **2j** crystalize in the Pnma space group, **2k** in $P6_5$ space group and **2m** in $P6_1$ space group. Compounds **2c** contain crystal solvate methanol. All the complex molecules in **2a**-**2m** are pentacoordinate with the cobalt(II) central atom. The tetradentate trenb ligand encapsulates the Co(II) atom and forms four Co$-$N bonds, while the fifth position is occupied by the (pseudo)halido monodentate ligand. The counter anion in the second coordination sphere changes through the series (Cl$^-$, Br$^-$, I$^-$). Three nitrogen donor atoms (N1, N2, N3) are the secondary amines and are located in the equatorial positions. The fourth N-donor atom (N4) is from tertiary amine group located in the axial position. The ML bond lengths with the trenb ligand are very similar for the whole series. The longest ML bonds were observed for the bonds with the halido ligands, the second longest are those with the N4 donor atom: $\underline{d}$(Co-X) = 2.35 $-$ 2.69 Å, d(Co-N4) = 2.21 $-$ 2.23 Å. The Co$-$N bonds with the equatorial nitrogen atoms are very similar throughout the series and they are the shortest: d(Co-N(1,2,3)) = 2.07 $-$ 2.11 Å. The geometry of the coordination polyhedra in **2a**-**2f** is slightly distorted trigonal bipyramid as can be described by the Addison parameter τ in **Table 1**. The crystal packing in the whole series is organized by the N$-$H$\cdots$X$\cdots$H$-$N interaction, which is causing the zig-zag packing, however, the observed donor-acceptor classify the present interactions among the weak non-covalent contacts: d(N$\cdots$X) = 3.29 to 3.63 Å [101](**Figure 44** and **Table 1**). Additionally, in **2a**-**2d** the C$-$H$\cdots$N hydrogen bonds between the N$_3{}^-$ or NCS$^-$ ligand and the aromatic C$-$H group of trenb were formed: d(C$\cdots$N) = 3.23 $-$ 3.79 Å.
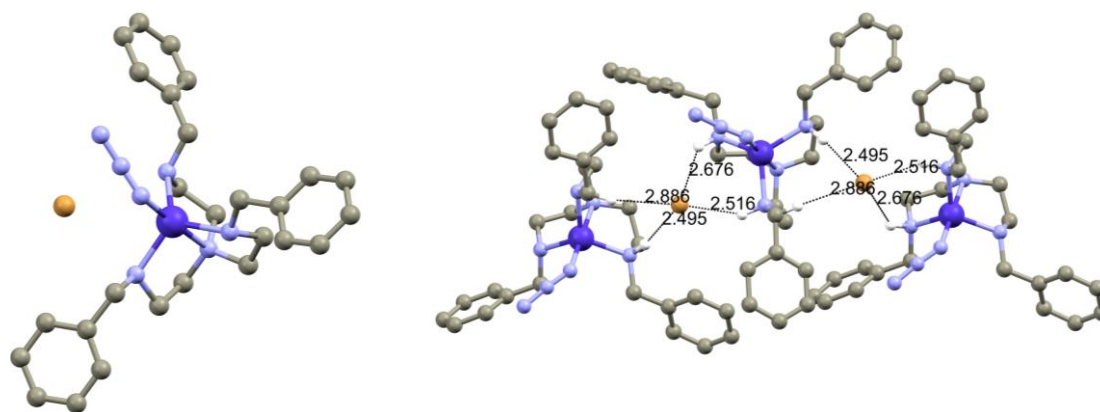
*Figure 42: Depiction of assymetric unit in the crystal structure of **2b** (left). Depiction of the H-Br interactions (black dashed lines) in the crystal lattice of **2b**. Grey (C), light blue (N), purple (Co), brown (Br), white (H). The hydrogen atoms besides those inolved in hydrogen bonding were ommited for clarity. Shown distances are in Å.*

Table 1: Summary of α and β angles, Addison parameter τ and bond lengths in the series of compounds with trenb ligand and showing average distance of hydrogen bonds between N-H···X···H-N.* single crystal data are of bad quality.

	τ	N1	N2	N3	N4	N5/X	N···X···N
2a	0.95	2.095(3)	2.091(3)	2.087(3)	2.226(1)	2.219(4)	3.301(2)
2b	0.99	2.095(4)	2.098(5)	2.115(5)	2.227(5)	2.010(5)	3.437(1)
2c	0.91	2.079(2)	2.097(2)	2.090(2)	2.218(2)	2.034(2)	3.289(2)
2d	0.91	2.107(3)	2.090(3)	2.092(3)	2.216(3)	2.051(3)	3.426(3)
2e	0.93	2.069(5)	2.088(5)	2.084(5)	2.216(5)	2.045(5)	3.305(4)
2f	0.93	2.081(3)	2.107(3)	2.096(3)	2.209(3)	2.081(3)	3.426(1)
2i	0.90	2.101(2)	2.119(2)	2.101(2)	2.225(2)	2.467(5)	3.414(3)
2j*	0.98	2.076	2.088	2.088	2.191	2.352	3.629
2k	0.96	2.084(6)	2.089(5)	2.102(5)	2.221(5)	2.496(1)	–
2m	0.91	2.089(8)	2.096(1)	2.121(9)	2.207(1)	2.687(2)	–

Magnetic properties:

Compounds **2a**-**2m** follow very similar behavior in both temperature and field dependent measurements. The μ_{eff}/μ_B is decreasing with decreasing temperature from about 4.5 at 300 K down to 4.2 at approximately 20 K, sudden drop of the μ_{eff}/μ_B value occurs (below 4.0 at 1.8 K). Such magnetic behavior is are typical for Co(II) SIMs as it demonstrates occurrence of ZFS. Magnetic measurements were newly performed and analyzed for **2b** (**Figure 45**). The temperature dependent data follow the same pattern as previously described for the rest of the series. The magnetic data have been fitted to the ZFS spin Hamiltonian (**Equation 11**) and the found ZFS parameters are $D = -5.39$ cm^{-1}, $E/D = 0.17$, $g_{iso} = 2.24$. Thus, the magnetic anisotropy of **2b** is small and axial, but with relatively large rhombicity.
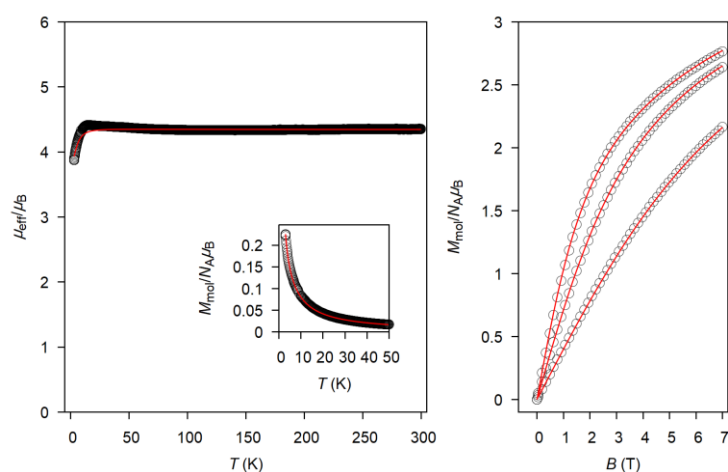
*Figure 43: PPMS measurements for **2b** - dependence of effective magnetic moment at temperature (right) and magnetization on magnetic field (left). Black circles represent experimental data and red lines are fit.*

HF-EPR:

The compounds **2a**, **2d**, **2f**, **2j** have been studied by HF-EPR. The ZFS parameters (zero-field resonance) for the **2a** (375 GHz) and **2j** (420 GHz) were directly observed in the HF-EPR spectra (**Figure 46**). The collected data have been fitted and the results of these analysis give important comparison with data obtained after analysis of PPMS measurements and theoretical calculations (**Table 2**). Additionally, the anisotropic g-values have been fitted (**Figure 46**). It is noteworthy to mention that the very large broadening of signals in the spectra of **2j** is caused by the exchange interactions in the crystal structure as the Co(II) centres lie relatively close to each other $d(\text{Co}\cdots\text{Co}) = 6.490$ Å and in the plane of Co$\cdots$Co interaction lies the chlorido ligand $d(\text{Co}\cdots\text{Cl}) = 4.145$ Å and his hydrogen bonds with ligand trenb as described in structure of **2j**. The ZFS parameters obtained by fitting of EPR data are not in all cases in a good agreement

with the values found by magnetic measurements. In the case of the small values of magnetic anisotropy in **2f** and **2d** (**Table 2**) the mismatch between the D signs determined by EPR and magnetometry is not surprising, because the fitting of the latter is not capable to distinguish correct sign of small D (e.g. with magnitude comparable to 2 cm^{-1}), especially in the case when rhombicity is present and fit was done for isotropic g-value. For **2j**, the $|D|$ value is still in reasonable agreement, however, the analysis of the EPR spectra was strongly affected by the line broadening. The relatively large difference between the calculated and experimentally (both magnetometry and HFEPR) determined D parameter in **2d** is hard to explain without a great deal of speculation. However, it must be emphasized that the temperature at which the crystal structure (and thus input geometry for calculations) was determined was much larger (150K) in comparison to the temperature range at which HFEPR was measured and at which the magnetic properties are sensitive to the present ZFS (below 20 K).

*Table 2: Comparison of the ZFS parameters obtained from DC measurements, from HF-EPR and from CASSCF/NEVPT2 calculations for 2a, 2d, 2f and 2j. * g values obtained from PPMS are g$_{iso}$ only.*

[Co(trenb)(N$_3$)]Cl **2a**	D	E/D	g_x	g_y	g_z
PPMS	-5.6	–		2.24*	
HF-EPR	-6.2	0.08	2.0	2.3	2.3
CASSCF	-2.3	0.09	2.2	2.2	2.3
[Co(trenb)(NCS)]Br **2d**	D	E/D	g_x	g_y	g_z
PPMS	-1.80	0.00		2.26*	
HF-EPR	2.14	0.16	2.15	2.09	2.24
CASSCF	-7.13	0.09	2.23	2.24	2.39
[Co(trenb)(NCSe)]Cl **2f**	D	E/D	g_x	g_y	g_z
PPMS	1.90	0.06		2.19*	
HF-EPR	-1.6	0.25	2.16	2.21	2.23
CASSCF	-4.6	0.14	2.19	2.27	2.22
[Co(trenb)Cl]Br **2j**	D	E/D	g_x	g_y	g_z
PPMS	-4.5	0.03		2.19*	
HF-EPR	8.5	0.05	2.1	2.3	2.2
CASSCF				–	
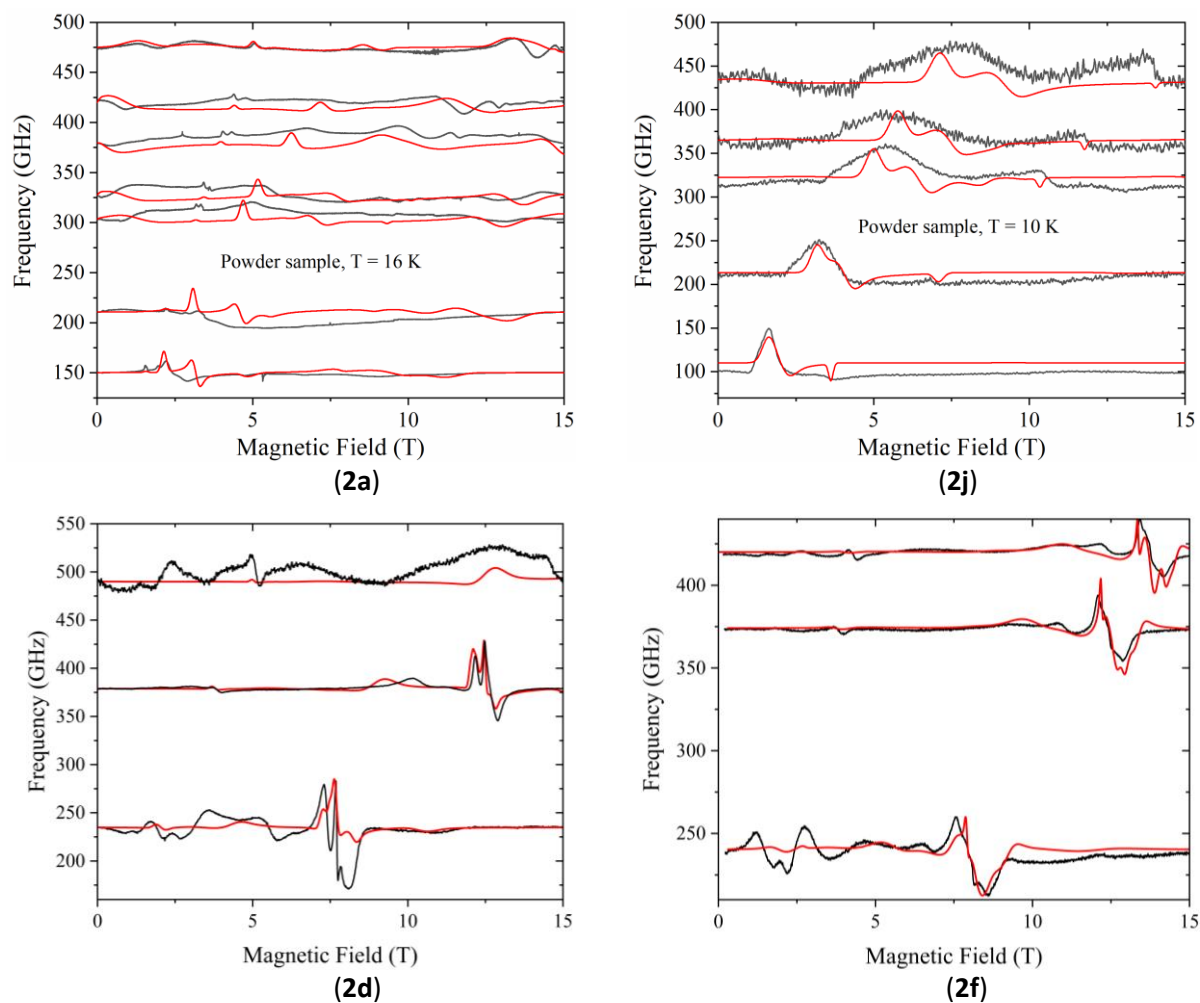
*Figure 44: EPR spectra for **2a**, **2d**, **2f** and **2j** measured at different frequencies and up to 15 T. Black lines represent experimental data and red lines are the fits.*

Theoretical calculation:

The CASSCF/NEVPT2 calculations were performed to theoretically predict the values of the ZFS and ligand field parameters (AI-LFT procedure). The summary of the calculated ZFS parameters for the trenb series can be found in **Table 3**.

	D	E/D	g_x	g_y	g_z
2a	-2.30	0.09	2.2	2.2	2.3
2b	-16.88	0.02	2.22	2.23	2.43
2d	-7.13	0.09	2.23	2.24	2.39
2e	1.27	0.25	2.24	2.25	2.36
2f	-4.60	0.14	2.19	2.27	2.22
2k	-4.02	0.13	2.25	2.27	2.36
2m	4.96	0.10	2.25	2.31	2.35

In general, the magnetic anisotropy is small with the D parameters adopting both positive and negative values, and rhombicity is significant. This can be explained on basis of the calculated electronic structure. First, the splitting of the ^4F atomic term to ligand field terms (LFTs) resulted in first excited LFT being energetically well separated from the ground state for 4000 cm^{-1} or even more (**Figure 47**). Next, the splitting of the d-orbitals corresponds well with expectations for the trigonal bipyramidal geometry with the degenerate pairs of d_{yz}, d_{xz} and d_{xy}, $d_{x^2-y^2}$ orbitals and (lowest in the energy), and d_{z^2} having the highest energy. Orbitals d_{yz} and d_{xz} are both occupied by two electrons, d_{xy}, $d_{x^2-y^2}$ and d_{z^2} is occupied with one electron each (**Figure 47**).Since the orbitals d_{xy} and $d_{x^2-y^2}$ have identical shape and the same quantum number ($m_l = \pm 2$) and the orbitals superimposable by rotation about an axis so the orbital angular momentum is present [102].
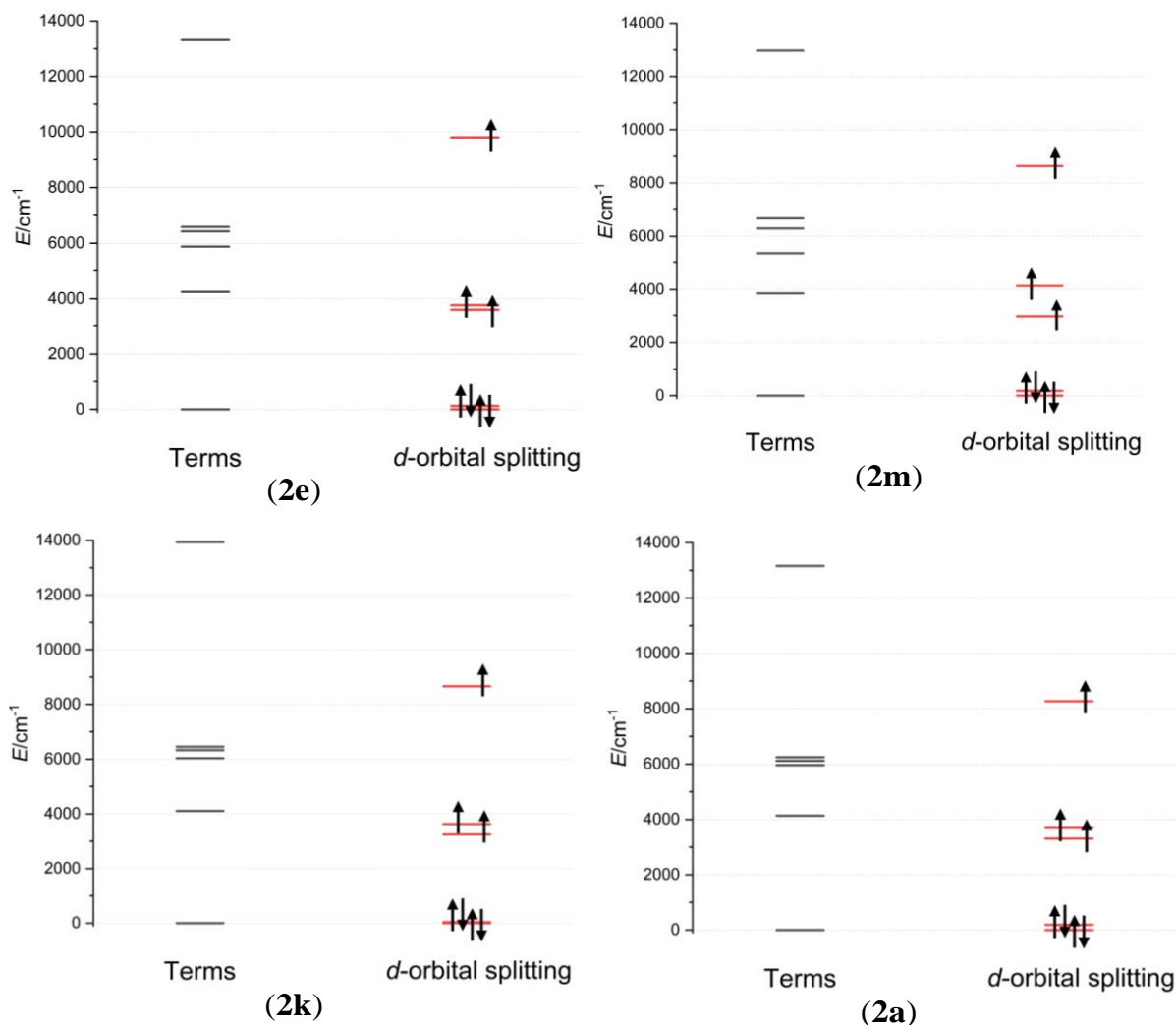
*Figure 45: Graphical representation of the ligand field terms and d-orbital energy levels as calculated by CASSCF/NEVPT2 for complexes **2a**, **2e**, **2k** and **2m**.*

<u>Depositions:</u>

Coordination compounds in this series have suitable ligands for deposition on the surfaces such as gold and graphene. Due to very poor solubility of **2a-2m** in any solvent a thermal sublimation was attempted. 15 nm thick film on the graphene and gold substrate was sublimed (at 350 °C). To verify the intactness of the studied compound, Raman spectroscopy was performed to compare the vibrational modes of the individual components of the resulting hybrid material. **Figure 48** shows Raman spectra, from top to bottom, of a SiO_2/Si + CVD graphene, powder of **2a** and deposited **2a** by thermal sublimation. The Raman spectrum of the bulk compound **2a** contains peaks characteristic of the ligand's functional groups such as benzyl, amine, and azide [103,104]. The strongest peaks around 1000, 1600, 3000 cm^{-1} originated mainly from benzyl group. In the Raman spectrum of the sublimated sample, we also observed these peaks, but their relative ratios were different. The peak around 1000 cm^{-1} was no longer the strongest

and peaks around 3000 cm^{-1} were dominated by aliphatic C-H bonds (< 3000 cm^{-1}) over aromatic (>3000 cm^{-1}). This indicated that compound **2a** has underwent a change during deposition.
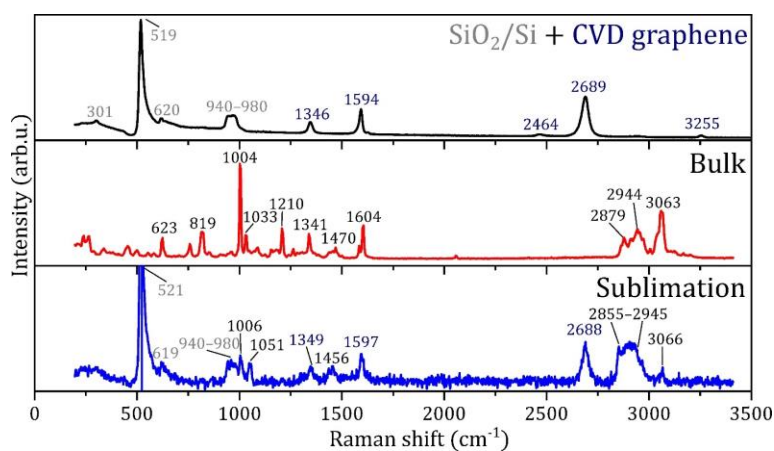
*Figure 46: Comparison of Raman spectra, from top to bottom, of the substrate: CVD graphene (Raman shift values marked in dark blue) on SiO2/Si (marked in grey), bulk **2a** and deposited **2a** by thermal sublimation (marked in black).*

XPS spectra show chemical composition for bulk and sublimated **2a** (**Figure 49**). Both survey spectra exhibited photoelectron peaks: Co 2p, N 1s, Cl 2p, C 1s, and O 1s; and Augers peaks: O$_{KLL}$ and Co$_{LMM}$. In the case of bulk spectrum, Sn 3d peak was observed. This contamination likely originated from a synthetic process of the ligand trenb. The detailed spectra of the selected peaks unveiled specific chemical composition. Co 2p peak of the bulk **2a** exhibited two main components Co 2p$_{3/2}$ and Co 2p$_{1/2}$ and shake-up satellites, which are common with paramagnetic states[105]. The oxidation state depends on spin-orbit splitting of the main components Co 2p$_{3/2}$ and Co 2p$_{1/2}$, and with Δ = 15.5 eV, it corresponds to Co(II) in the high-spin state[106]. In the case of the sublimated sample, the Co 2p signal is weak. However, it was possible to observe and fit the peak Co 2p$_{3/2}$ and the satellite, which was shifted with respect to the peak of the bulk (0.9 eV and 1.4 eV to higher binding energy, respectively).

In the case of N 1s of the bulk, the peak included five components. The main component corresponds to the amine at 399.9 eV, and two smaller peaks at 398.5 eV and 402.8 eV were attributed to the azido group[107,108]. The smallest peak at 406.3 eV may be attributed to chemisorbed nitrogen[109]. The origin of the fifth peak at 397.1 eV may correspond to unreacted azide[110]. In the case of the sublimated sample, the main component and chemisorbed nitrogen were shifted by 0.5 eV and 0.8 eV to higher binding energy, and a new peak appears at 401.9 eV. Components characteristic of the azido ligand are no longer present.

Considering the changes in the ratio of the peaks in the Raman spectrum and especially in the XPS spectrum of nitrogen, where we did not observe peaks of the azido group and a new peak appears, it indicated possible sample decomposition during the sublimation.
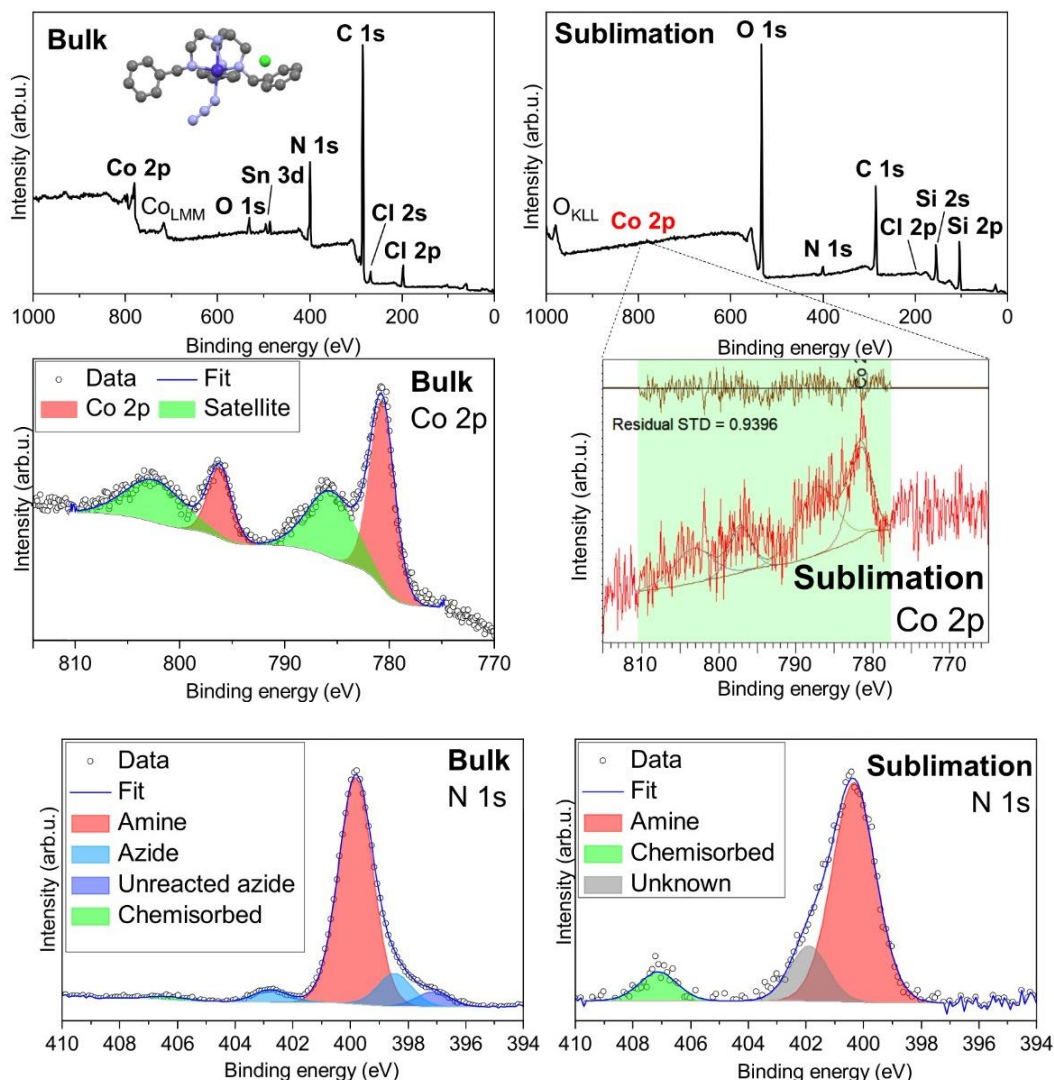
*Figure 47:Comparison of XPS spectra of the bulk and sublimated **2a** on graphene.*

TGA performed on **2c** revealed abrupt weight loss at temperatures above 250 °C. The morphology of the sample after sublimation on surface was probed by AFM and SEM (**Figure 50**). This decomposition was corroborated by comparison of bulk and sublimated **2a** by Raman and XPS. Raman spectra of sublimated compound on surface did not show signature vibrational molecular peaks.

The deposition of **2b**, **2c**, **2d** and **2j** were performed and the hybrid materials were investigated by Raman and XPS resulting in even larger spectral changes than was observed for **2a**.

As a conclusion, it was found out that despite of having favorable molecular geometry the physical parameters of the presented trenb complexes were not suitable for wet or sublimation deposition techniques.
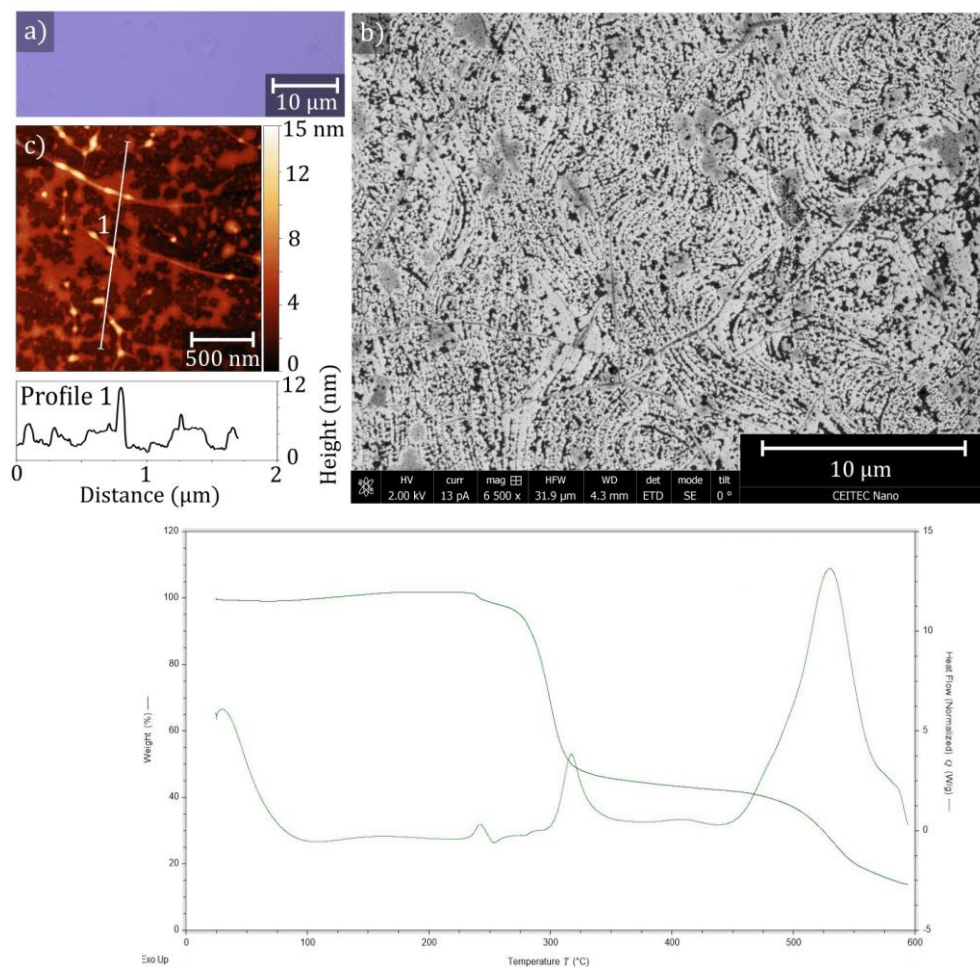
*Figure 48: a) optical image of **2a** sublimated on graphene, b) SEM image of sublimated **2a**, c) AFM image and height profile along the white line profile **2a**. In the bottom of the figure: TGA analysis for **2c** revealed abrupt mass loss at temperatures above 300 °C.*

5.3 Mono and Polynuclear Complexes with H_3tipa Ligand

This section discusses synthesis of coordination compounds with the trigonal ligand H_3tipa. The suitability of this ligand for coordination of lanthanides was discussed in section 5.1, here will be coordination of this ligand to the Co(II) central atom discussed. The tetradentate nature of this ligand allows encapsulation of the Co(II) central atom with a possibility for additional coordination of the monodentate ligand resulting into coordination number 5. Moreover, the ligand H_3tipa can become a bridging ligand and induce formation of polynuclear coordination compounds. As will be discussed below, it was also revealed that in a basic solutions a Co(III) complex with the doubly or triply deprotonated H_3tipa ligan was formed and acted as metallo-ligand for coordinating the Co(II) atoms.

A series of the reactions with varying level of deprotonation of H_3tipa ligand and with varying monodentate ligands was designed and prepared yielding six coordination compounds. These complexes have been structurally, magnetically, and spectroscopically studied. The formulas of the studied complexes are following: $[Co(H_2tipa)Cl]\cdot CH_3OH$ (**3a**), $[Co(H_2tipa)Cl]\cdot CH_3OH$ (**3b**), $[Co(H_2tipa)(NCS)]\cdot H_2O$ (**3c**), $(Et_3NH)[\{Co(III)_2(Htipa)(tipa)(NCS)_2\}Co(II)(NCS)_2]$ (**3d**), $(Et_3NH)_2[\{Co(III)_2(tipa)_2(NCS)_2\}\{Co(II)(NCS)_2\}_2]$ (**3e**) and $[\{Co(III)_2(tipa)_2(H_2O)_2\}\{Co(II)Cl_2\}_2]\cdot H_2O\cdot CH_3OH$ (**3f**).

5.3.1 Mononuclear Complexes with H_3tipa Ligand

Synthesis of **3a**, **3b** was done as followed: 1 mmol of $CoCl_2\cdot 6H_2O$/$CoBr_2$ was dissolved in 5 ml of MeOH and was added to the 5 ml MeOH solution of 1 mmol of H_3tipa and 1 mmol of Et_3N and stirred. Clear purple solution was filtered and crystalized by slow diffusion of diethyl ether into the mother liquor. Good quality purple crystals suitable for X-Ray diffraction studies were obtained this way (**Figure 51**).

Synthesis of **3c** was done by two different setups. As a first **3c** was prepared similarly to **3a** and **3b**. 1 mmol of $CoCl_2\cdot 6H_2O$ in 5 ml of MeOH was mixed with solution of H_3tipa and Et_3N in 5 ml MeOH and 1 mmol of KNCS was added as a solid. However, this approach often led to occurrence of impurities such as **3a** or even **3d** and **3e**. To prepare pure **3c**, first **3a** or **3b** were prepared and isolated. Then they were used as a precursor and were dissolved in 5 ml of MeOH and 1 mmol of KNCS was added. The resulting solution produced good quality single crystal upon diffusion of diethyl ether into mother liquor (**Figure 51**).
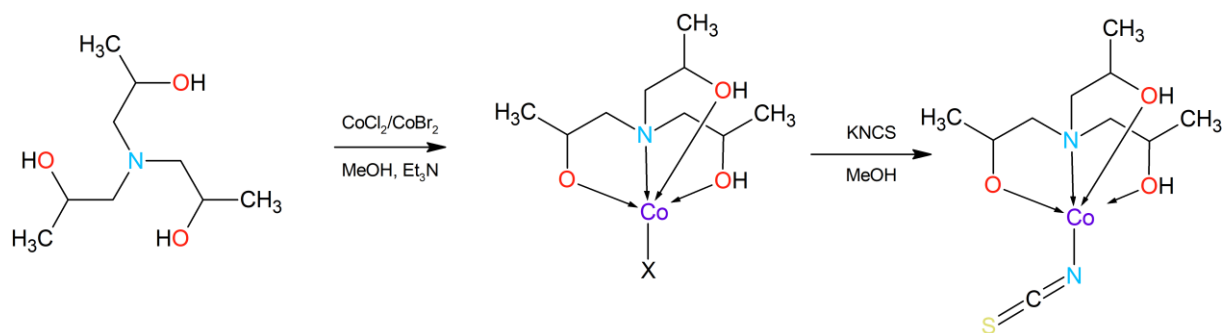
*Figure 49: Synthetic scheme for preparation of **3a** and **3b**, followed by synthesis of **3c**. X = Cl or Br.*

Crystal structures:

The crystal structures were successfully determined for all the prepared coordination compounds of this series. **3a** and **3b** are isomorphous and crystalize in the $P2_1/c$ space group and both contain crystal solvate methanol. **3c** crystalizes in the $P2_1/n$ space group and contains one molecule of water as crystal solvate in its unit cell (**Figure 52**). The ligand H_3tipa is once deprotonated in the structures of **3a**, **3b** and **3c** and coordinates to the central Co(II) by one nitrogen and three oxygen donor atoms. The fifth position is occupied by the monodentate (pseudo)halogenido ligand Cl⁻, Br⁻ or NCS⁻. The geometry of their coordination polyhedra is a little distorted trigonal bipyramid with following Addison parameters: τ(**3a**) =0.86, τ(**3b**) =0.84 and τ(**3c**) =0.79. The longest ML bonds are those with the halogenido ligands: d(Co-Cl) = 2.296(4) Å and d(Co-Br) = 2.453(1) Å. The Co–N bond with the isothiocyanido ligand is significantly shorter: d(Co-NCS) = 2.025(3) Å. The Co–N bonds with the nitrogen atoms of the H_3tipa ligand are very similar in the structure of all three compounds with the bond lengths ranging in the very narrow interval: d(Co-N) = 2.15 – 2.16 Å. This is similar also for the Co–O ML bonds with the protonated O-donor atoms (d(Co-OH) = 2.02 – 2.06 Å) or deprotonated O-donor atoms of the H_2tipa⁻ ligand (d(Co-O) = 1.98 – 1.98 Å).

The crystal packing in **3a** and **3b** is organized by strong O-H⋯O hydrogen bonds (d(O-H⋯O) = 2.62-2.59 Å) that are formed between the protonated hydroxy groups of the H_2tipa ligand and solvate methanol molecules. Another type of the O–H⋯O hydrogen bond (d(O-H⋯O) = 2.66-2.69 Å) is formed between deprotonated hydroxy groups of the H_2tipa ligand and solvate methanol molecules (**Figure 52**). The crystal packing in **3c** is different since the O–H⋯O and O–H⋯S hydrogen bonds are present. The O-H⋯O hydrogen bonds (d(O-H⋯O) = 2.644(4) Å) are formed between the protonated hydroxy groups of the H_2tipa ligand and solvate water molecules. Another type of the O–H⋯O (d(O-H⋯O) = 2.737(3) Å) is formed between

deprotonated hydroxy groups of the H₂tipa ligand and solvate water molecules. The O−H···S hydrogen bonds (d(O−H···S) = 3.368(3) Å) are formed between the sulfur atom from the isothiocyanido ligand and solvate water molecule (**Figure 52**). The presence of hydrogen bonds causes formation of supramolecular dimer of **3a**, **3b** and **3c**.

(**3a**)   (**3b**)   (**3c**)

(**3a**)   (**3c**)
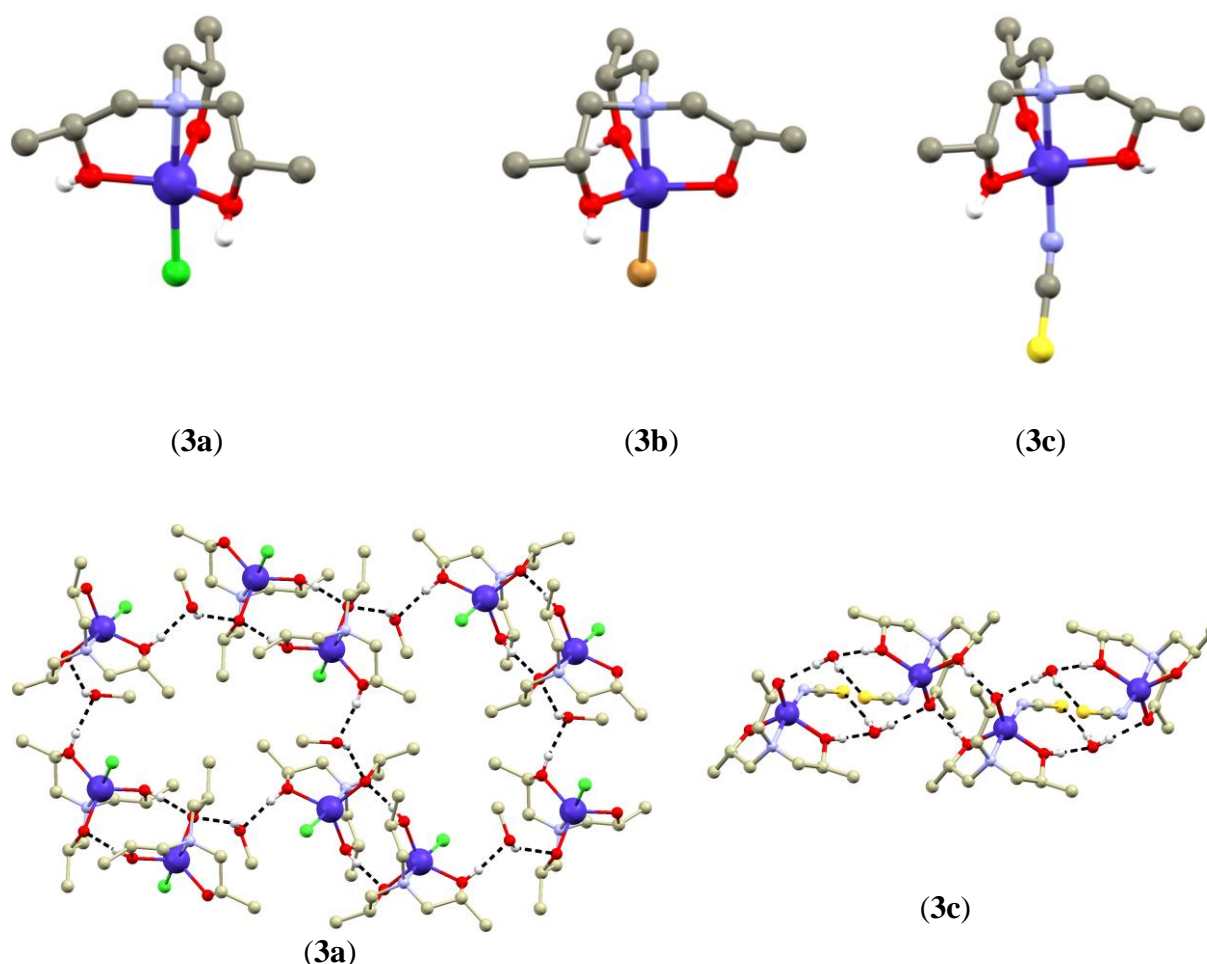
*Figure 50: Depiction of crystal structures of **3a**, **3b** and **3c** and hydrogen bonds (blacked dashed lines) formed in crystal of **3a** and **3c**. Grey (C), light blue (N), purple (Co), green (Cl), yellow (S), red (O), white (H). The hydrogen atoms besides those involved in hydrogen bonding were ommited for clarity.*

Magnetic properties:

The maxima in the susceptibility plots of **3a-3c** visible at low temperatures (at ca. 7K) (insets in **Figure 53**) indicate a presence of non-negligible antiferromagnetic interactions in these compounds. Since these complexes are mononuclear the magnetic exchange pathways could be ascribed to the shortest non-covalent interactions assembling the [Co(H₂tipa)X] molecules (X = Cl⁻, Br⁻, NCS⁻) into the supramolecular dimers via strong O−H···O hydrogen

bonding (*vide supra*). Therefore, the magnetic data were analyzed by spin Hamiltonian for dimer with the exchange coupling, anisotropy and Zeeman terms:

$$\hat{H} = -J(\vec{S}_1 \cdot \vec{S}_2) + \sum_{i=1}^{2} D_i(\hat{S}_{z,i}^2 - \hat{S}_i^2/3) + E_i(\hat{S}_{x,i}^2 - \hat{S}_{y,i}^2) + \mu_B B g_i \hat{S}_{a,i} \tag{18}$$

The magnetic data were depicted as temperature dependence of μ_{eff}/μ_B and field dependence of molar magnetization in Figure 49.

μ_{eff}/μ_B of **3a** and **3c** have similar at 300 K (5.42 and 5.22) and it decreases with temperature. The μ_{eff}/μ_B decreases at lower temperatures suggesting presence of ZFS and antiferromagnetic exchange coupling provided by strong hydrogen bonds. The temperature data follow similar pattern for all three compounds (**Figure 53** and **Table 4**).

The ZFS parameters and exchange interaction J are shown in **Table 4**. The magnetic anisotropy of **3a** and **3b** is small and axial and for **3c** is relatively big, all three compounds have large rhombicity.

Table 4: Summary of ZFS parameters and exchange interaction from fitting the magnetic data for positive and negative D.

	D	*E/D*	g_{iso}	*J*
3a	-6.61/6.59	0.33/0.29	2.03/2.03	-1.54/-1.60
3b	-8.87/8.70	0.33/0.33	2.17/2.17	-1.55/-1.54
3c	-14.37/14.27	0.33/0.33	2.13/2.13	-1.65/-1.66

(3a)   (3c)
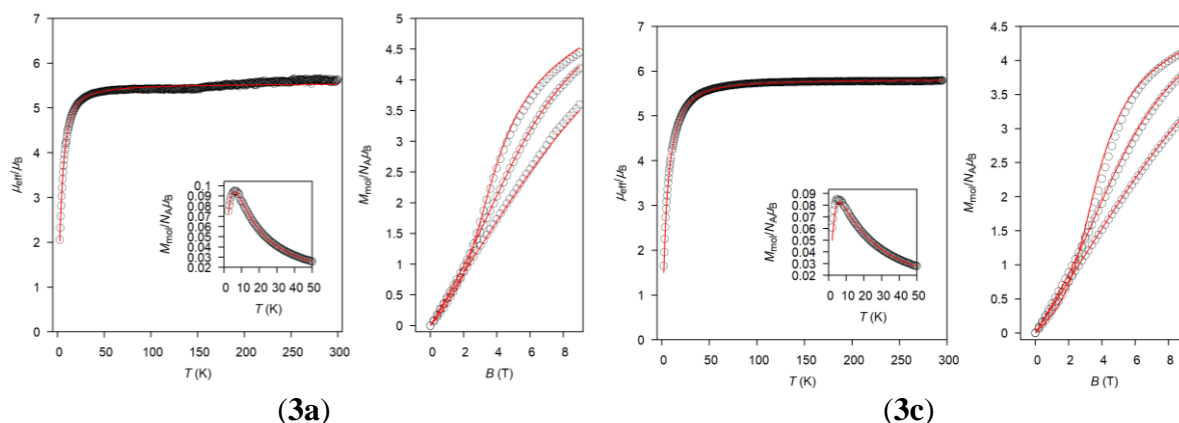
*Figure 51: Static magnetic measurements of **3a** and **3c** under external magnetic field 0.2 T. Dependence of μ_{eff}/μ_B on temperature (left) and $M_{mol}/N_A\mu_B$ on magnetic field (right). Black circles are data, red lines are fits.*

Theoretical calculations:

*Table 5: Comparison of CASSCF calculations for **3a**, **3b** and **3c**.*

	D	E/D	g_{iso}
3a_1	-7.24	0.21	2.23
3a_2	-7.54	0.13	2.22
3a_3	-7.75	0.17	2.23
3b_1	-8.85	0.27	2.22
3b_2	-8.93	0.12	2.22
3b_3	-8.73	0.07	2.22
3c_1	-9.97	0.25	2.22
3c_2	-9.34	0.18	2.22
3c_3	-9.94	0.24	2.22

The CASSCF/NEVPT2 calculations were performed for **3a-3c** on three structural models (extracted from the corresponding crystal structures). The ZFS parameters were calculated for the following structural fragments:

1) supramolecular dimers {[Co(H$_2$tipa)X]···[Zn(H$_2$tipa)X]}, in which one of the Co(II) atoms was substituted by diamagnetic Zn(II) (**3a_1**, **3b_1** and **3c_1**).
2) monomers in the presence of the crystal solvates (methanol in **3a_2**, **3b_2**, H$_2$O in **3c_2**)
3) monomers (**3a_3**, **3b_3**, **3c_3**).

It was found that the choice of the structural fragment did not influence calculated values of the D parameter much, but rhombicity changed significantly (**Table 5**). The axial magnetic anisotropy is a relatively small but axial for **3a** and the $|D|$ value is slightly growing for **3b** and **3c** respectively. This is in good agreement with the experimental values obtained by magnetometry (**Table 4**). The rhombicity was calculated largest for the dimeric fragments and therefore the better agreement with the magnetic measurements was achieved for calculations with the highest computational costs, especially in the case of **3a_1** and **3b_1**, whereas calculated rhombicity of **3c_1** and **3c_3** is comparable. The CASSCF/NEVPT2 calculations

were also used to predict the ligand field parameters (AI-LFT procedure, **Figure 54, Figure 70**).

The magnetic anisotropy of **3a-3c** can be explained on basis of the calculated electronic structure. First, the splitting of the ^4F atomic term to ligand field terms (LFTs) resulted in first excited LFT being energetically separated from the ground state for about 4000 cm^{-1} (**Figure 54**). Therefore, the second-order spin orbital coupling can be expected to induce magnetic anisotropy. The splitting of the d-orbitals corresponds well with expectations for the trigonal bipyramidal geometry with the degenerate pairs of d_{yz}, d_{xz} and d_{xy}, $d_{x^2-y^2}$ orbitals (lowest in the energy), and d_{z^2} having the highest energy. Orbitals d_{yz} and d_{xz} are both occupied by two electrons, d_{xy}, $d_{x^2-y^2}$ and d_{z^2} are occupied with one electron each (**Figure 54**).
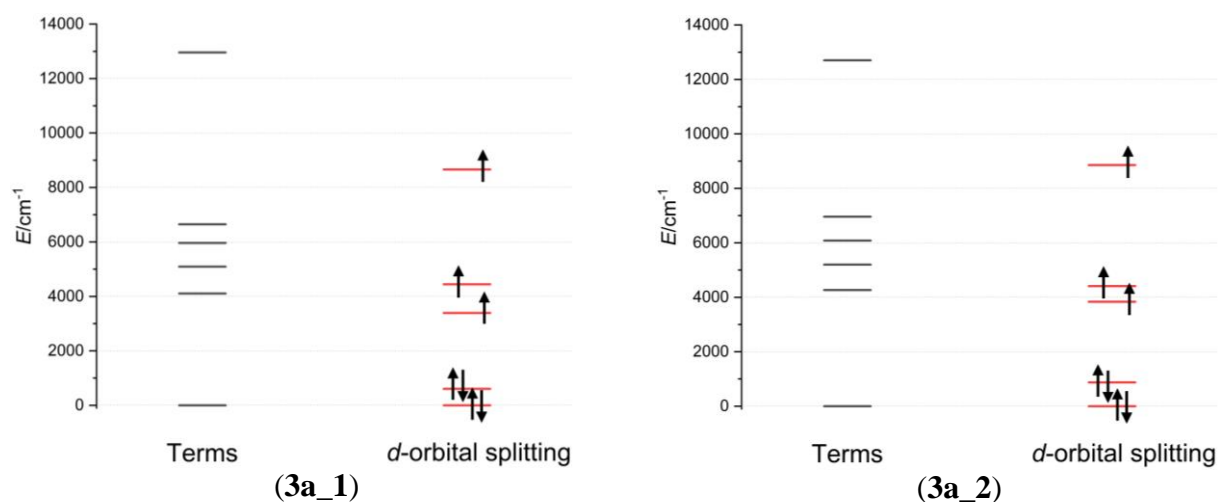
*Figure 52: Graphical representation of the ligand field terms terms and d-orbital energy levels as calculated by CASSCF/NEVPT2 for complexes **3a_1** and **3a_2**.*

The magnetic exchange interaction in **3a-3c** was also studied theoretically by means of the Broken-Symmetry DFT (BS-DFT) which calculates energies of the selected polynuclear fragments either with spins oriented parallelly (high-spin state, HS) and anti-parallelly (broken-symmetry state, BS). From the energy difference the isotropic exchange coupling constant is calculated using according to formulas established by L. Noodleman et al.[111,112], A. Bencini et al.[113] and Yamaguchi et al.[114] The BS-DFT calculations were performed at B3LYP/def2-TZVP level of the theory on the fragments selected from the crystal structures of **3a-3c**. The obtained results confirmed the assumption about dominant exchange pathway through the O–H···O hydrogen bonding within the supramolecular dimer. The spin density is localized dominantly on the metal centers; however, its part is distributed also on the oxygen atoms involved in the hydrogen bonding (**Figure 55**). The calculated exchange coupling constants are very similar

for all three complexes and agrees rather well with the J-values determined from experimental data: $J/cm^{-1} = -1.6$ (**3a**), -1.6 (**3b**), -1.9 (**3c**).
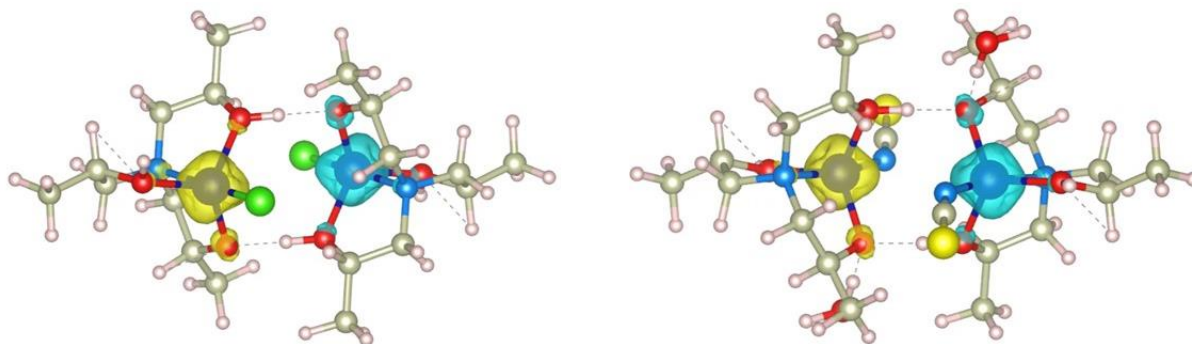
*Figure 53: Graphical representation of the calculated spin densities distribution for the broken-symmetry states of **3a** (left) and **3c** (right). Positive and negative spin densities are represented by yellow and blue surfaces, respectively. The isodensity surfaces are plotted with the cutoff values of $0.02 ea_0^{-3}$*

5.3.2 Tri- and Tetranuclear SMMs with H$_3$tipa Ligand
<u>Synthesis:</u>

Used stoichiometric ratios of reactants for preparation of **3d**, **3e** and **3f** did not correspond to the stoichiometry of the complexes. First, an extensive screening of the reactant ratios combined with titration investigation to investigate the influence of basis/KNCS concentrations (starting with stoichiometric ratios of 1:0 **3a**: KNCS up to 1:20 with varying combinations) on formation of **3d** and **3e** was performed. Based on the results of titration experiments it was revealed that, despite a weak basic nature of NCS$^-$, it was not sufficient to treat solutions containing Co^{2+} ions and H$_3$tipa molecules only by KNCS to achieve both oxidation of cobalt ions and deprotonation of the H$_3$tipa ligand. Using UV-VIS spectrometry it was determined that for successful preparation is necessary combination of Et$_3$N and KNCS, while using solely KNCS led the most probably to a formation of the [Co(NCS)$_4$]$^{2-}$ anions in titrated solutions[115] (**Figure 56**).
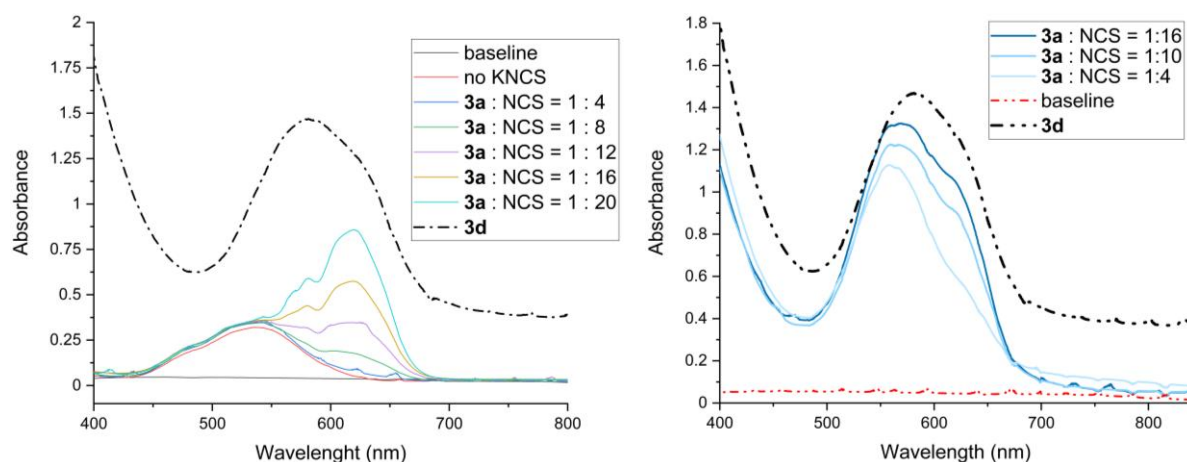
Figure 54: UV/VIS spectra of titration investigation of polynuclear H₃tipa complexes. Left – titration without base. Right – titration with base.

Pure batch of **3d** was prepared by reaction of $CoCl_2 \cdot 6H_2O$, H₃tipa, KNCS and Et₃N in molar ratios 1:2:4:4 in methanol (**Figure 57**). The solution was heated and stirred for 1 hour and filtered through the paper filter. Upon crystallization by slow diffusion of diethylether into mother liquor, the good quality crystals were acquired. If the reaction was heated for too long and the volume of methanolic solution was significantly reduced (more than one fourth of the volume) a crystallization of **3a** occurred.

Similar reaction setup was used to prepare pure **3e** where the reaction ratios were 2:1:3:3 (**Figure 57**).

A bottom-up synthesis for **3d** and **3e** was also tested by reacting **3c** with $Co(NCS)_2$ in different ratios (1:1 for **3d** and 1:2 for **3e**) in basic methanolic solutions (Et₃N). Resulting solutions were crystallized by slow diffusion of diethylether forming a blue microcrystalline slurry which was recrystallized in acetone and again crystallized by slow diffusion of diethylether. This way the crystals of **3d** and **3e** were obtained but in the minimal yield (5%).
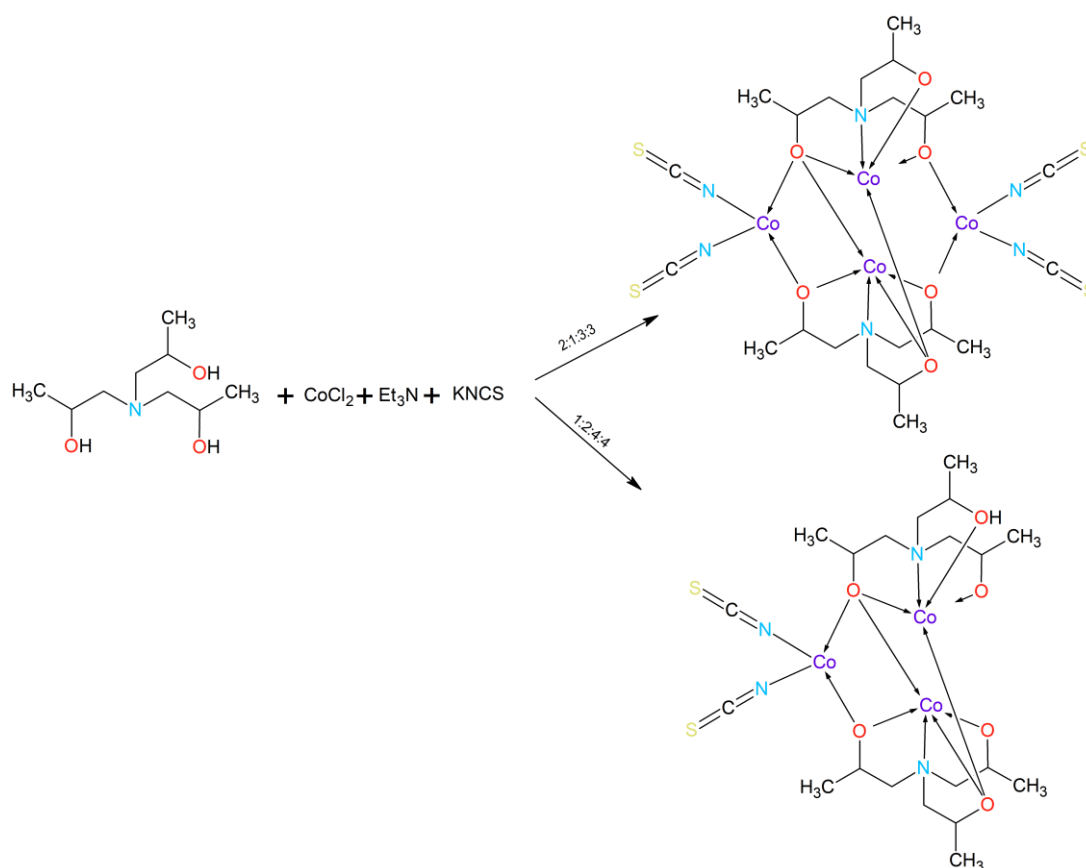
*Figure 55: Synthetic scheme of preparation of compounds **3d** and **3e**.*

3f was prepared only by reaction in microwave reactor. 1 mmol of CoCl$_2$·6H$_2$O, 1 mmol of H$_3$tipa and 1 mmol of Et$_3$N in 5 ml of iPrOH were mixed and placed in the Anton Paar reaction vessel and heated up at 120 °C for 10 minutes. Resulting blue solution was filtered through the paper filter and crystallized by slow diffusion of diethyl ether producing good quality crystals (**Figure 58**).
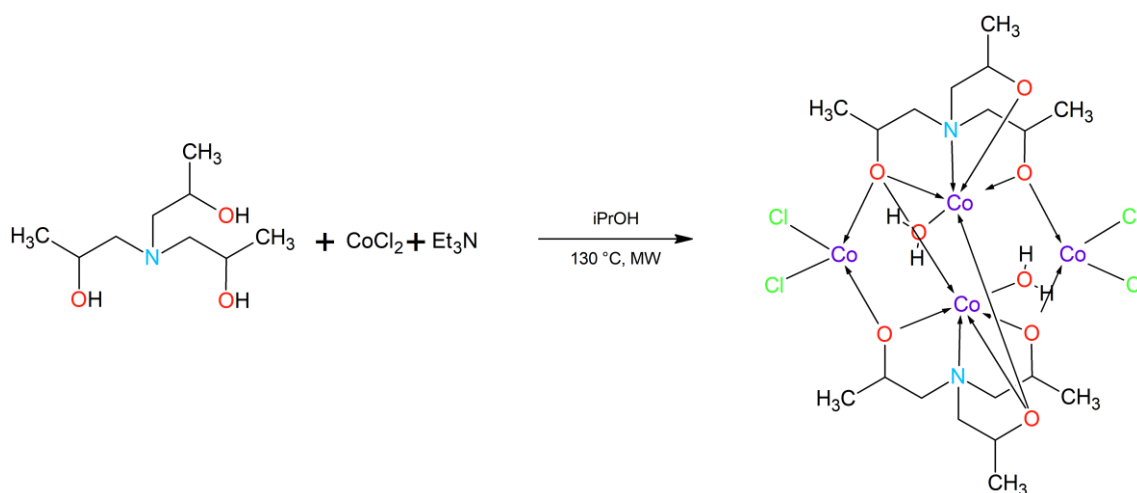
*Figure 56: Synthetic scheme for preparation of compound **3f**.*

Crystal structure:

Compound **3d** crystalizes in the monoclinic space group $P2_1/c$. This trinuclear complex molecule is not electroneutral and its charge is balanced by the Et_3NH^+ cation. The complex anion $[\{Co_2(Htipa)(tipa)(NCS)_2\}\{Co(NCS)_2\}]^-$ is composed of two hexacoordinate Co(III) subunits $\{Co_2(Htipa)(tipa)(NCS)_2\}^-$, which are bridged by the deprotonated μ-O atoms of two H_3tipa ligands. The sixth positions are occupied by the NCS^- ligands. These bonds are rather short d(Co–O) = 1.88-1.93 Å, d(Co–N) = 1.90-1.92 Å, which corresponds with their low spin state and oxidation number (III). The third Co center is tetracoordinated by two oxygen atoms from the Co(III) subunits and by two NCS^- ligands (**Figure 59**). The bond lengths are longer than for Co(III) suggesting the oxidation number (II): d(Co–O) = 1.99-2.00 Å, d(Co–N) = 1.97-1.99 Å. The oxygen atoms from the H_3tipa ligand are forming strong intramolecular hydrogen bonds d(O···O) = 2.434(3) Å. Another type of N–H···S hydrogen bonding is formed between the sulphur atom of one of the NCS^- ligands and amine group from the Et_3NH^+ cation: d(N···S) = 3.304(6) Å.

The compound **3e** crystalizes in the monoclinic space group $P2_1/c$ and consist of two Et_3NH^+ cations balancing charge of the complex anion $[\{Co_2(tipa)_2(NCS)_2\}\{Co(NCS)_2\}_2]^{2-}$, which is centrosymmetric (**Figure 59**). The Co(III) atoms are coordinated in the same manner as in **4b** with one difference, both the H_3tipa ligands are fully deprotonated. The subunits $\{Co_2(tipa)_2(NCS)_2\}^{2-}$ work as bridging metallo-ligands and their central atoms adopt the low-spin state with rather short bond lengths d(Co-N) = 1.90-1.92 Å, d(Co-O) = 1.90-1.95 Å. They are coordinating two tetracoordinate subunits $\{Co(NCS)_2\}_2$ which are both coordinated by two oxygen atoms of the H_3tipa ligand and two nitrogen atoms from NCS^- monodentate ligands. The geometry of coordination polyhedron is distorted tetrahedral. The bond lengths are again longer for the Co(II) high spin centres d(Co-N) = 1.97-2.00 Å, d(Co-O) = 1.90-1.96 Å. The Et_3NH^+ cations form N–H···S hydrogen bonds with the NCS^- ligands d(N···S) = 3.283(4) Å.

The compound **3f** crystalizes in the monoclinic space group $P2_1/n$ and with two crystal solvate methanol and two water molecules per complex molecule and the structure is centrosymmetric (**Figure 59**). The structure of **3f** differs from **3d** and **3e** by absence of the cations balancing the charge as **3f** is electroneutral. The compound contains two subunits coordinated by the H_3tipa ligand in the same manner as it is for **3e** with all the hydroxy groups being deprotonated and with one important difference causing electroneutrality of the complex molecule - the sixth position is occupied by aqua ligand: $[\{Co_2(tipa)_2\}\{CoCl_2\}_2]$. The metal-

ligand bond lengths are: $d(\text{Co–O}) = 1.87\text{-}1.96$ Å, $d(\text{Co–N}) = 1.92$ Å. This confirms that the Co centers are in the low-spin state and in the oxidation state (III). The two tetracoordinated Co centers in the $\{\text{CoCl}_2\}_2$ moiety are coordinated by two oxygen atoms from the H_3tipa ligand and by two chlorido ligands. The geometry of coordination polyhedral is distorted tetrahedral with longer coordination bonds than were observed for Co(III) fragment: $d(\text{Co–O}) = 1.95\text{-}1.96$ Å, $d(\text{Co–Cl}) = 2.28\text{-}2.29$ Å. Thus, the Co centers are in the high-spin state and having oxidation number (II). The water crystal solvate molecules are forming the O–H···O hydrogen bonds with aqua ligand $d(\text{O···O}) = 2.692(4)$ Å. Relatively strong O–H···Cl hydrogen bonds are also formed between crystal solvate and aqua ligand $d(\text{O···Cl}) = 2.710(5)$ Å.
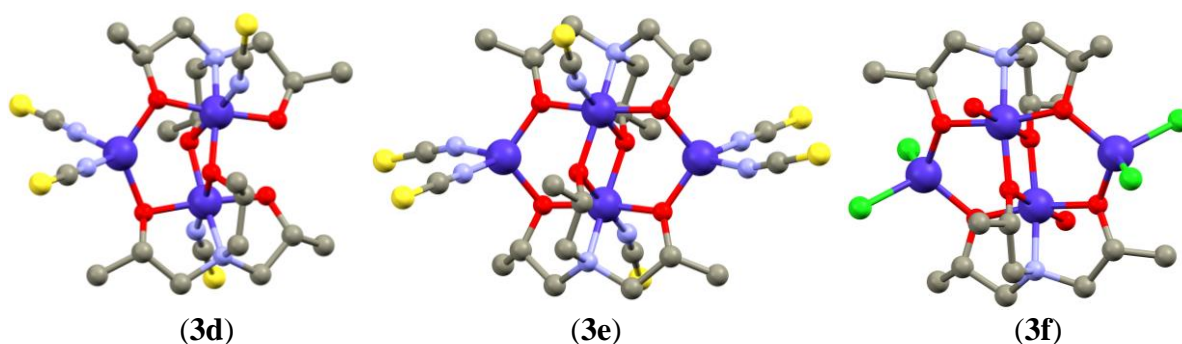
*Figure 57: Depiction of the complex molecules from the crystal structures of **3d**, **3e** and **3f**. Purple (Co), grey (C), red (O), light blue (N), green (Cl), yellow (S), hydrogen atoms were omitted for clarity.*

Magnetic properties:

3d, **3e** and **3f** contains Co(II)–Co(III) mixed-valence complex molecules containing with one (**3d**) or two (**3e**, **3f**) paramagnetic Co(II) centers. This composition difference indeed influences the magnetic response of the samples.

The effective magnetic moment of **3d** has value of 4.15 at 300 K, which is larger than spin only value ($\mu_{\text{eff}} = 3.87$ μ_B for $g = 2.0023$ and $S = 3/2$) indicating spin-orbital contribution to the ground state. The μ_{eff}/μ_B value decreases very gradually with temperature and below 50 K, the decrease becomes more pronounced (3.2 at 2 K). With respect to the crystal structure of **3d** the observed decrease of μ_{eff} below 50 K can only be ascribed to the zero-field splitting (ZFS), and therefore, the magnetic data were analyzed using the ZFS spin Hamiltonian (**Equation 11**, **Figure 60** and **Table 6**). The fitting of magnetic data resulted in the following set of parameters: $g = 2.14$, $D = \text{-}17.2$ cm^{-1} a $E/D = 0.02$. Thus, the magnetic anisotropy in **3d** is relatively large, axial with a low rhombicity. This makes **3d** to be a good candidate for observation of slow-magnetic relaxation.

The μ_{eff}/μ_B value for **3e** is 6.0 at ($\mu_{eff} = 5.48\ \mu_B$) 300 K and remains constant down to 50 K and on further cooling it drops to 2.8 at 2 K (**Figure 60** and **Table 6**). Such behavior indicates ZFS together with antiferromagnetic type of magnetic coupling between two Co(II) ions in **3e** separated on relatively short distance (5.76 Å). Therefore, besides the ZFS terms also the magnetic exchange coupling term was included into analysis of the magnetic data (**Equation 18**). The two sets of the fitted parameters sufficiently reconstructed the experimental data (one with $D>0$, second for $D<0$, **Table 6**). The exchange interaction between the Co(II) centers was fitted to be $J = -0.59\ cm^{-1}$ for $D<0$, or $J = -0.83\ cm^{-1}$ for $D>0$.

The μ_{eff}/μ_B value for **3f** is 5.5 ($\mu_{eff} = 5.48\ \mu_B$) at 300 K and gradually decreases down to 5.2 at 50 K where a sudden drop occurs to 2.3 at 3 K (**Figure 60** and **Table 6**). Similarly, to **3e**, this indicates a presence of magnetic exchange interaction together with ZFS. Therefore, the spin Hamiltonian including the ZFS and exchange terms were used (**Equation 11 Table 6**). The exchange interaction between the Co(II) atoms was fitted to be $J = -1.3\ cm^{-1}$.

Despite the rather similar Co(III) metallo-ligand and tetracoordinate nature of the Co(II) central atoms in both **3e** and **3f**, the magnitude of D differs significantly. Another puzzling thing is difference in magnitude of the exchange coupling constant J -obviously the exchange interaction is mediated through the shortest possible super-exchange pathway, which is in this case Co(II)−O−Co(III)−O−Co(II) pathway. This is shorter (7.67 Å) for **3e** which exhibits weaker exchange interaction than **3f** possessing longer pathway (7.75 Å).
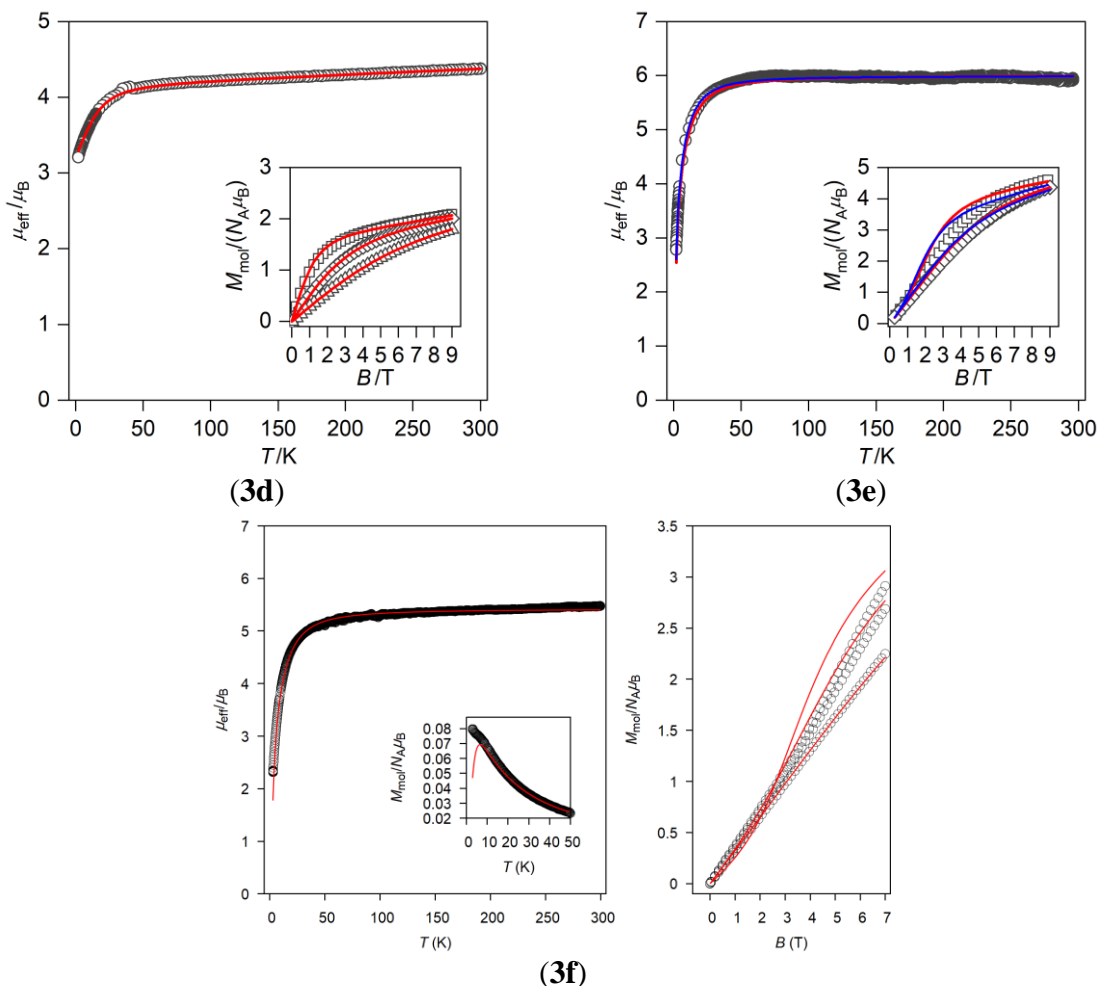
*Figure 58: Static magnetic measurements for **3d**, **3e** and **3f** under external magnetic field 0.1 T. Black circles represents experimental data, red and blue lines are fits.*

*Table 6: ZFS parameters and exchange interaction J obtained from the magnetometry for **3d**, **3e** and **3f**.*

	D	*E/D*	g_{iso}	*J*
3d	-17.2	0.02	2.14	–
3e	-13.8/+12.9	0.00/0.33	2.19/2.19	-0.59/-0.83
3f	9.5	0.00	1.99	-1.3

For **3d** have been performed also dynamic magnetic measurements. Under the small static external field (B_{DC} = 0.1 T) appeared out-of-phase susceptibility signal as frequency dependent maxima which confirms presence of the slow relaxation of magnetization in **3d**. Argand diagrams and Arrhenius law plot were constructed (**Figure 61**). The best fit provided following values: τ_0 = 4.1(3.9)·10^{-9} s and U_{eff} = 35.0(3.1) K. The U_{eff} obtained from Arrhenius law is in very good agreement with a value calculated using **Equation 13** with ZFS parameters: U_{eff} = 34.4 K.
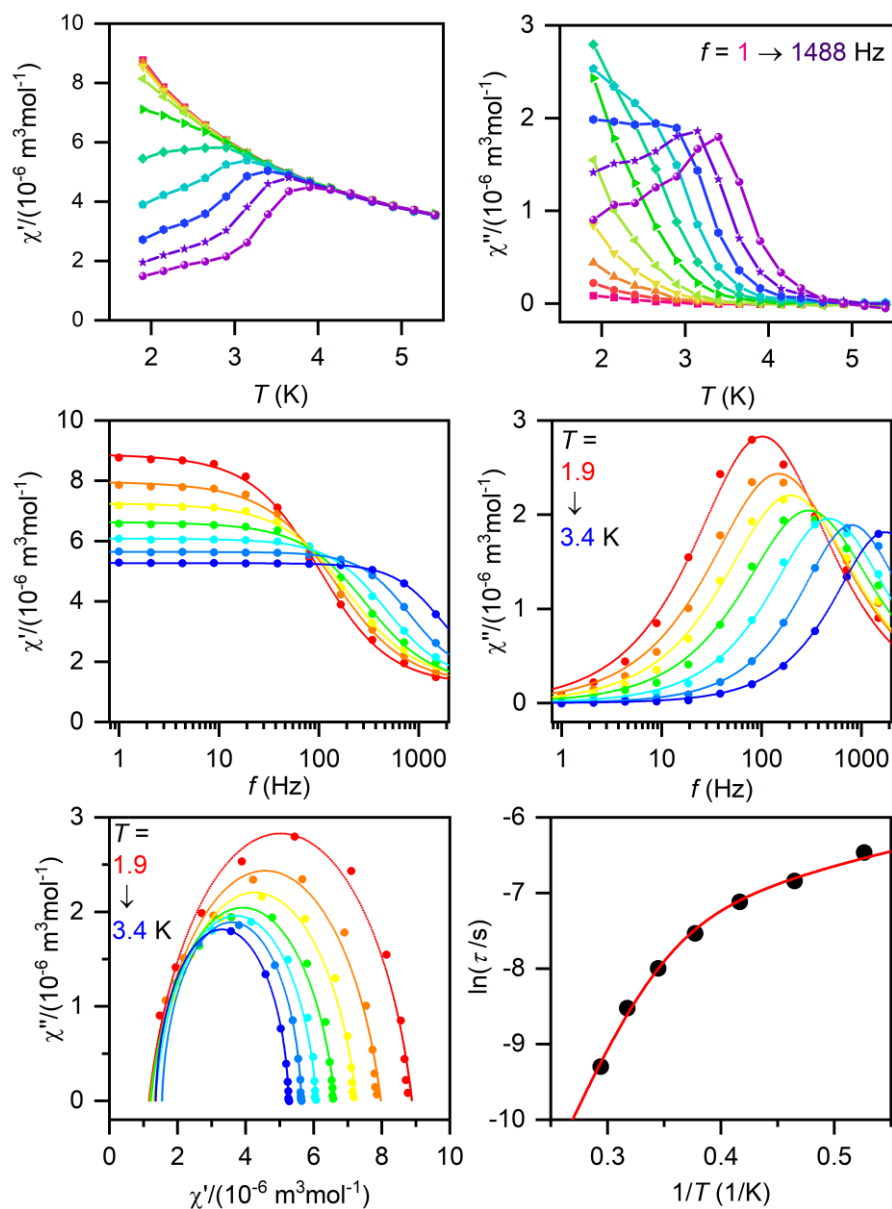
*Figure 59:The AC measurements of **3d**, temperature dependent data (top), frequency dependent data (middle), Argand diagram (left bottom) and Arrhenius diagram (right bottom).*

Theoretical calculations:

The analysis of magnetic data was supported by the CASSCF/NEVPT2 theoretical calculations, which were utilized to calculate all energy levels resulting from the $3d^7$ electronic configuration (**Figure 62**) with the ORCA 4.2 computational package[88]. The cation(s) (Et_3NH^+) were also involved in the calculations due to the fact that they form hydrogen bonds to the coordinated isothiocyanido ligands, and previously (and also for **3a-3c** in this thesis) it was found that such weak interaction can have significant impact on ZFS parameters[116,117].

	D	*E/D*	g_x	g_y	g_z
3d	-15.2	0.21	2.26	2.39	2.18
3e	8.09	0.32	2.24	2.30	2.18
3f	-4.69	0.28	2.26	2.29	2.33

The CASSCF/NEVPT2 calculations were performed to theoretically predict the values of the ZFS and ligand field parameters (AI-LFT procedure). ZFS data collected from the calculations are compared in **Table 7**. The axial parameter of magnetic anisotropy is negative for **3d** and its value is in a relatively good agreement with the magnetometry results. The *D* parameter calculated for **3e** is positive and again, agreement with the result provided by magnetometry (**Table 6**) is quite good. The largest disagreement between theory and experiment was observed for **3f**, for which the best fit of magnetic data gave the positive *D* value, however, the calculations provided significantly smaller |*D*| and with negative sign. Calculations predicted large rhombicity for all the complexes **3d-3f**. The calculated d-orbital splitting is characteristic for tetracoordinated species and weak ligand field (weakest for **3f**, **Figure 62**). The separation of the first LF term is satisfactory (1100 for **3d**, 1000 for **3e** and 1159 for **3f**) allowing use of spin Hamiltonian and confirming expected second-order SOC contribution.
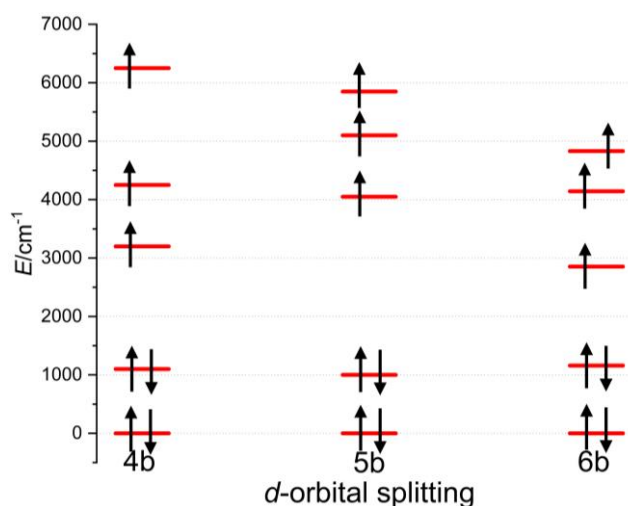
*Figure 60: Theoretical calculations of d-orbital energy levels for **3d**, **3e** and **3f**.*

The magnetic exchange interaction between the Co(II) atoms in **3e-3f** was also studied theoretically by BS-DFT calculations, which were performed at B3LYP/def2-TZVP level of the theory on the molecular structures selected from the crystal structures of **3e-3f**. The calculated spin density is localized dominantly on the metal centers; however, its part is

distributed also on the oxygen atoms which supports hypothesis about the Co(II)–O–Co(III)–O–Co(II) magnetic exchange pathway (**Figure 63**). The calculated exchange coupling constants confirm antiferromagnetic coupling and agree rather well with the *J*-values determined from the experimental data: $J/cm^{-1} = -0.4$ (**3e**) and -2.2 (**3f**).
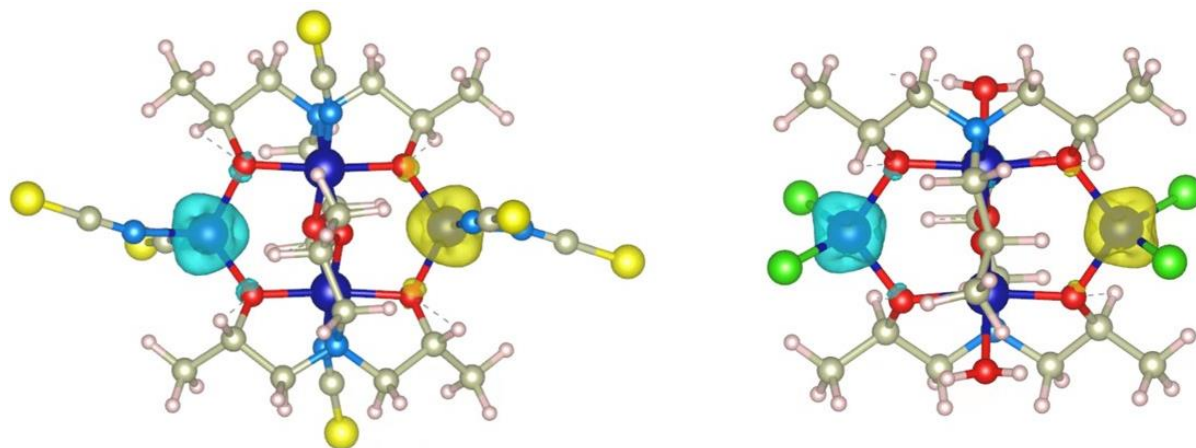
*Figure 61: Graphical representation of the calculated spin densities distribution for the broken-symmetry states of **3e** (left) and **3f** (right). Positive and negative spin densities are represented by yellow and blue surfaces, respectively. The isodensity surfaces are plotted with the cutoff values of $0.02 ea_0^{-3}$*

5.4 {M[Co(acac)$_3$]}$_n$ Magnetic Chains

Organic molecule acetylacetone (acac) contains two possible O-donor atoms in its structure and it is rather sterically compact, potentially allowing high coordination numbers of the acetylacetonato complexes. Additionally, the preparation of the alkali metal salts of acac introduces new option which is interaction between the complex anion (in the case of Co(II) formation of [Co(acac)$_3$]$^-$ is expected) with the alkali metal cations, similarly as was described by Zadrozny et al. [36]. Thus, under appropriate conditions, the linear chain structure composed of alternating complex and alkali metal ion building blocks is expected to form and therefore, this type of coordination compounds are potential candidates for observation of the magnetic properties characteristic of SCM. For these reasons three acac salts have been prepared (namely Liacac, Naacac and Kacac) and coordinated to Co(II) affording following coordination compounds – Li[Co(acac)$_3$] (**4a**), Na[Co(acac)$_3$] (**4b**) K[Co(acac)$_3$] (**4c**) (**Figure 66**).

The structure of the studied acetylacetonate Co(II) complexes have been previously published in the literature [118–120] and remarkably, the Li salt has been investigated as precursor for preparation of non-aqueous redox flow cells with applications in batteries[121]. In this thesis the modified and simplified synthesis of the **4a**, **4b** and **4c** is reported: 4 mmol of NaOH/KOH/LiOH·H$_2$O was dissolved in 5 ml of MeOH and 4 mmol of acac was added and

the mixture was stirred. 1 mmol of CoCl$_2$·6H$_2$O was added to the solution and it was stirred overnight. A purple powder was filtered through the paper filter and the mother liquor was left for isothermal crystallization. After 3-7 days purple needle shaped crystals suitable for single crystal diffraction formed (**Figure 64**)
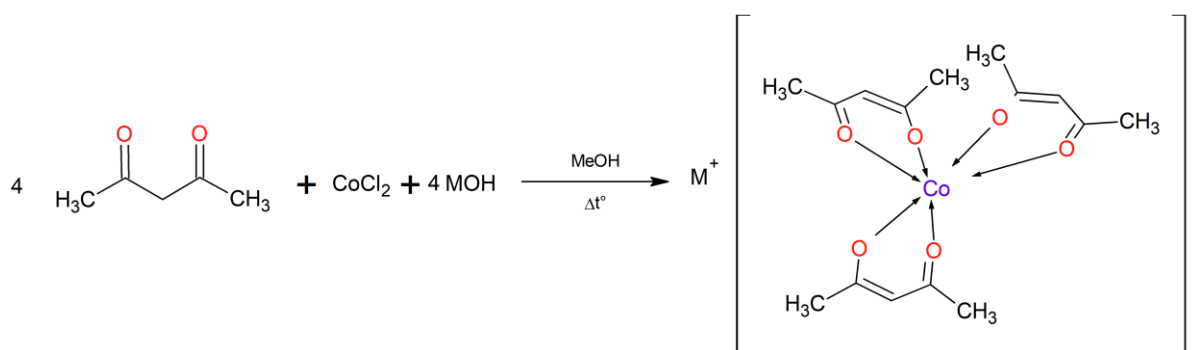
*Figure 62: Synthesis scheme for preparation of compounds **4a-4c**.M = Li(**4a**), Na(**4b**) or K(**4c**).*

Crystal structure:

As was mentioned above the crystal structures of the discussed compounds were previously published, here discussed as the crystal structures were obtained at low temperature in this thesis.

Compound **4a** crystalizes in the R$\bar{3}$c space group. The Co–O bonds have all the same length: d(Co–O) = 2.052(2) Å. The threefold main axis parallel to the c-axis goes through the Co and Li atoms, whereas three two-fold axes each going through the middle carbon atom of the acac ligand are perpendicular to the threefold main axis. The two-fold axes are perpendicular to the main axis and together with the absence of horizontal and diagonal planes this gives D_3 symmetry of the complex subunit. The charge of the [Co(acac)$_3$]$^-$ is compensated by the Li$^+$ cation. The lengths of the interactions between the ligand's oxygen atoms and the Li$^+$ cation are all equal: d(Li$^+$···O) = 2.135(5) Å. The chain-like structure of **4a** propagates along the c crystallographic axis with the angle Li–Co–Li being 180° (**Figure 65**). The distance between Co and Li$^+$ is d(Co-Li$^+$) = 2.738(4) Å and it is longer than in **4b,** but the distance between two in-chain neighbouring Co centres is shorter d(Co···Co) = 5.471(4) Å (**Figure 66**).

Compound **4b** isostructural to **4a** crystalizes in the R$\bar{3}$c space group. Three bidentate acac ligands are coordinating the Co center by two O-donor atoms each and all having the same length d(Co-O) = 2.069(3) Å. Again, the local symmetry of the complex part is D_3.

The charge of the $[Co(acac)_3]^-$ is compensated by the Na^+ cation. The oxygen atoms of ligand for interactions with the cation all of equal lengths $d(Na^+\cdots O) = 2.346(1)$ Å as well as with the cation of the neighboring unit. The chain-like structure of **4b** propagates along the c crystallographic axis holding thus linear Na–Co–Na angle. The distance between Co and Na^+ is rather short: $d(Na^+\cdots Co) = 2.975(2)$ Å and distance between two in-chain neighbouring Co centres is 5.951(2) Å. These interactions and their influence on forming a chain-like structure (**Figure 66**) is similar to that described by Zadrozny et al[36] (**Figure 26**).

Compound **4c** differs from **4a** and **4b**. It crystalizes in the monoclinic space group Pna2$_1$. In the crystal structure there are several features like in **4a** and **4b**. The charge of the $[Co(acac)_3]^-$ is compensated by the K^+ cation. The Co centre is coordinated by oxygen atoms of the three acac ligands, however in **4c** their bond lengths are not equal, but varying within the narrow range: $d(Co-O) = 2.06-2.09$ Å. The K–O bonds lengths also differs with $d(O-K^+) = 2.6-2.79$ Å. The distance between the Co and K atoms is $d(Co\cdots K^+) = 3.389(2)$ Å and it is longer than in **4b**, while the distance in between two in-chain Co centres is shorter $d(Co-Co) = 6.611(2)$ Å. The structure of **4c** does not propagate itself along the crystallographic a-axis in the linear manner and the Co–K–Co angle is 153.86(8)° (**Figure 65**), though, the structure is still chain-like (**Figure 66**).

(a)   (b)
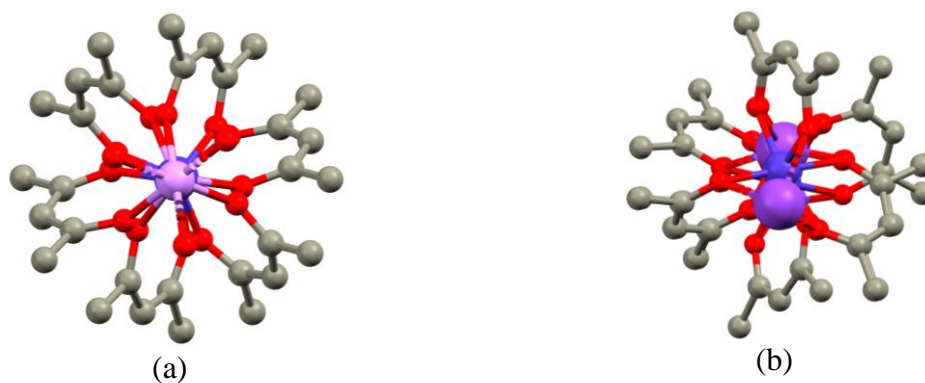
*Figure 63: View along crystallographic c-axis for **4a** a) and along a-axis for **4c** b). Purple (Co), pink (Li), dark pink (K), grey (C), red (O), hydrogen atoms are omitted for clarity.*

(**4a**)

(**4b**)

(**4c**)
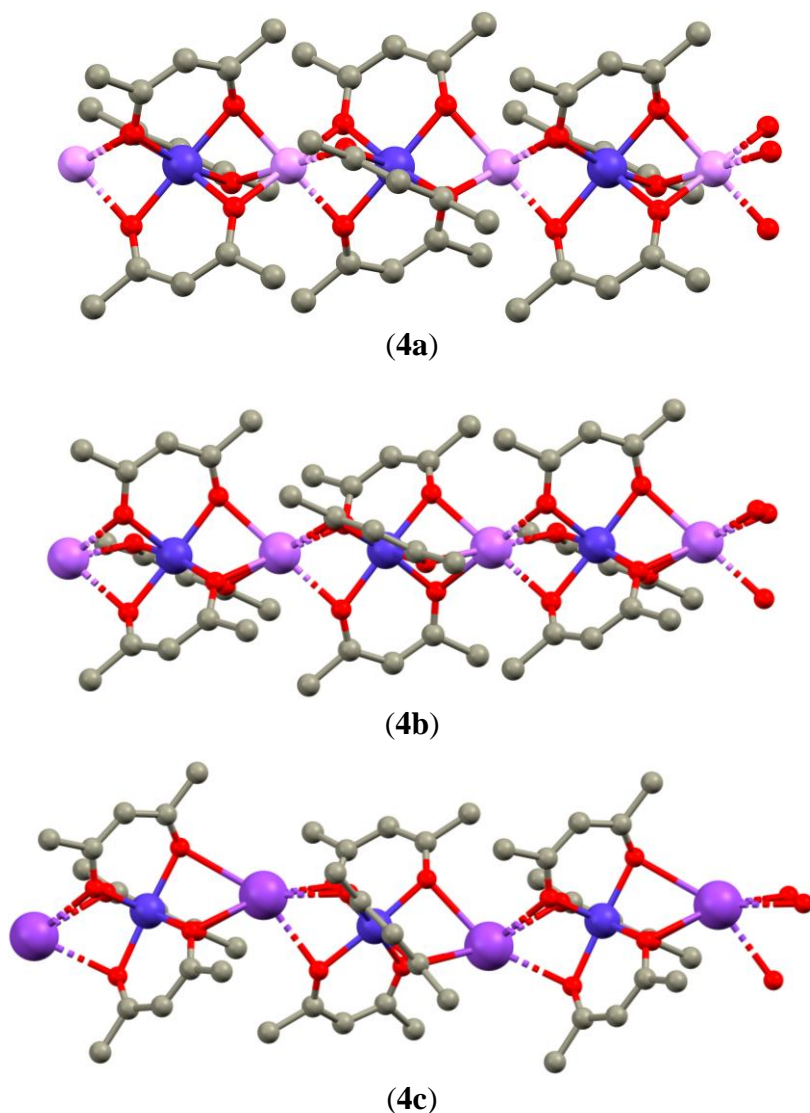
*Figure 64: Perspective view of a chain-like substructure of **4a**, **4b** and **4c**. Purple (Co), light pink (Li), pink (Na), dark pink (K), grey (C), red (O), hydrogen atoms are omitted for clarity.*

Theoretical calculations:

For the ideal D_3 symmetry, which was observed for **4a** and **4b,** the expected ground spin state (LF multiplet) for species with $S = 3/2$ is ^4E. Such ground term is orbitally degenerate and as such, it is a subject of the first order SOC producing huge and axial magnetic anisotropy[122,123]. The AILFT calculations revealed d-orbital splitting typical for trigonal prism, though this geometry does not correspond to that of coordination polyhedron in **4a** and **4b** as can be confirmed by calculation of continuous measure indexes (**Figure 67**). The lowest energy was calculated for the orbital d_z^2 (two electrons), and two degenerate pairs d_{xy}, $d_{x^2-y^2}$ (three electrons) and d_{yz}, d_{xz} (two electrons) have higher energy. Thus, the total spin is $S = 3/2$ and the configuration is orbitally degenerate (**Figure 67**). The orbital splitting in **4c** is very similar to

those calculated for **4a** and **4b**, however, the degeneracy of the d_{xy}, $d_{x^2-y^2}$ and d_{yz}, d_{xz} pairs is not perfect and they are separated by 67cm^{-1} (d_{xy}, $d_{x^2-y^2}$) and 333 cm^{-1}(d_{yz}, d_{xz}).
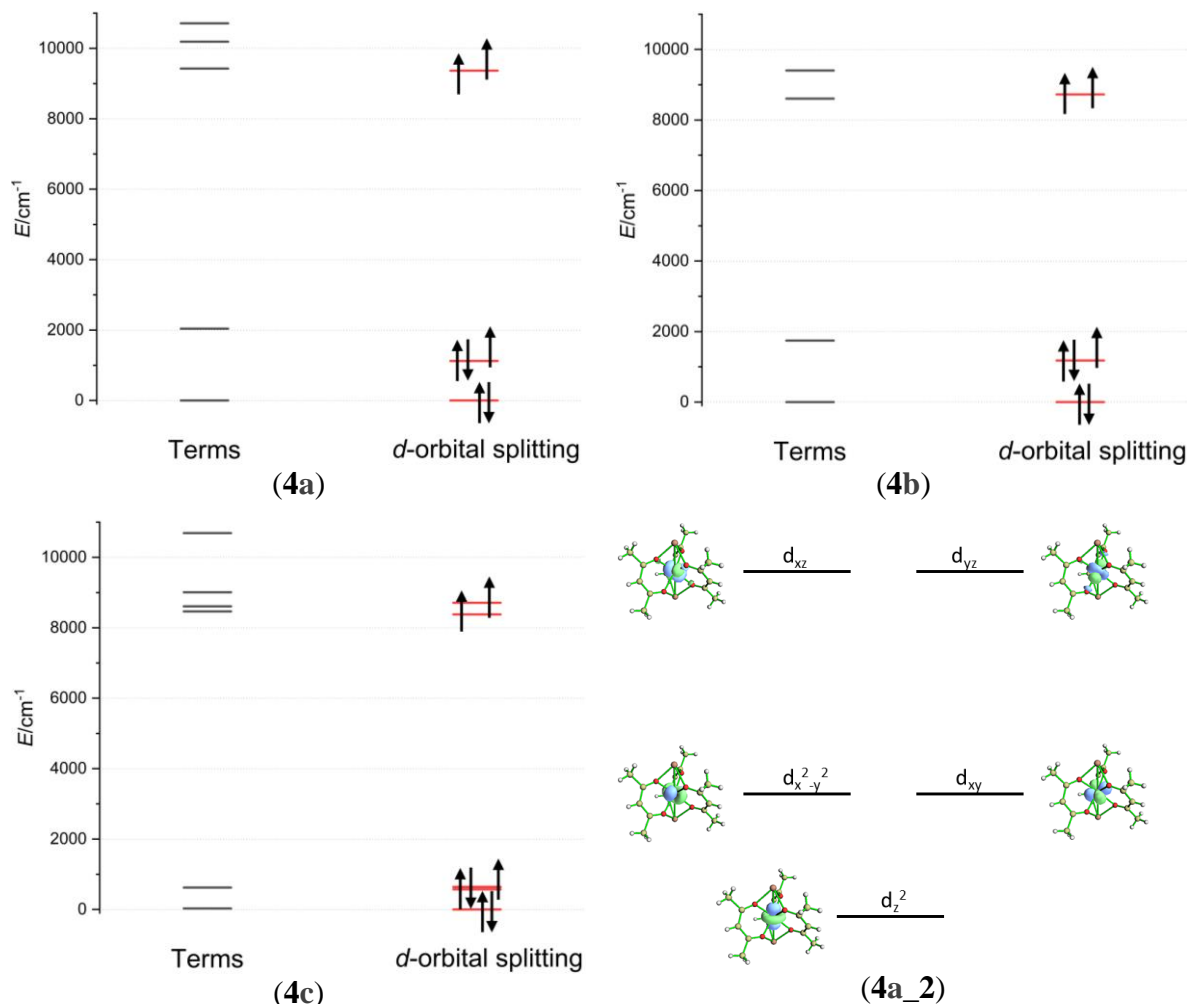
*Figure 65: Theoretical calculations of terms and d-orbital energy levels for **4a**, **4b** and **4c** and graphical depiction of the calculated orbitals by ab-initio ligand field theory in **4a** (**4a_2**).*

Due to the degeneration of the ground state (and non-applicability of spin Hamiltonian) it was not possible to calculate ZFS parameters for **4a** and **4b**. The calculated energy separation of the ground and first excited LF multiplets is 241 cm^{-1} (in **4a**) and 238 cm^{-1} (in **4b**). This indicates a very large magnetic anisotropy in these compounds. Calculation of the ZFS parameters for **4c** was successful, however, the calculated parameters must be taken with great care because the first excited LF term adopt a rather low energy (30 cm^{-1}) and thus, spin Hamiltonian formalism is not applicable.

The BS-DFT calculations were used to determine possible magnetic interactions between the in-chain lining Co(II) atoms with the expected Co−M$_a$−Co exchange pathway (M$_a$

= Li, Na, K). The calculations were performed at B3LYP/def2-TZVP level of the theory on the in-chain fragments as selected from the crystal structures of **4a-4c**. Remarkably, the calculations brought a rather surprising result. The magnetic exchange interaction was calculated to be negligible for **4a** ($J = 0.01$ cm^{-1}), which has the smallest in-chain separation between the Co atoms. The exchange interaction in **4b** was calculated to be weak and antiferromagnetic ($J = 2.50$ cm^{-1}). Again, weak and antiferromagnetic exchange interaction was calculated also for **4c** ($J = 1.74$ cm^{-1}). However, the energy of the ZFS splitting is in **4a-4c** that large, that splitting of the levels due to exchange interactions in **4b** and **4c** would be negligible.

Magnetic properties:

The μ_{eff}/μ_B of **4a** slowly decreases from 4.44 at 300K down to 3.99 at 70 K and decreases steeper further to 2.94 at 2.9 K (**Figure 68**).

The μ_{eff}/μ_B of **4b** has value of 4.79 at 300 K and it gradually decreases with temperature down to 3.68 at 3 K (**Figure 68**).

The μ_{eff}/μ_B of **4c** has value of 5.19 at 300 K and it gradually decreases with temperature down to 3.14 at 3 K (**Figure 68**).

In the previous section, we have shown that spin-Hamiltonian is not suitable for analysis of the magnetic data of **4a-c**. Nevertheless, the utilization of the L-S Hamiltonian based on Griffith and Figgis which describes the splitting of the $^4T_{1g}$ term originating from the ^4F atomic term in lower symmetries than O_h[124–127]. However, this approach did not bring any reasonable result. Therefore, to at least quantify apparent large magnetic anisotropy, the measured data were analyzed and fitted using Spin Hamiltonian using program POLYMAGNET[128]. The found ZFS parameters are shown in **Table 8**. The magnetic anisotropy is very large and for **4a** and **4c** is negative with small rhombicity. The magnetic anisotropy for **4b** is positive with maximal rhombicity.

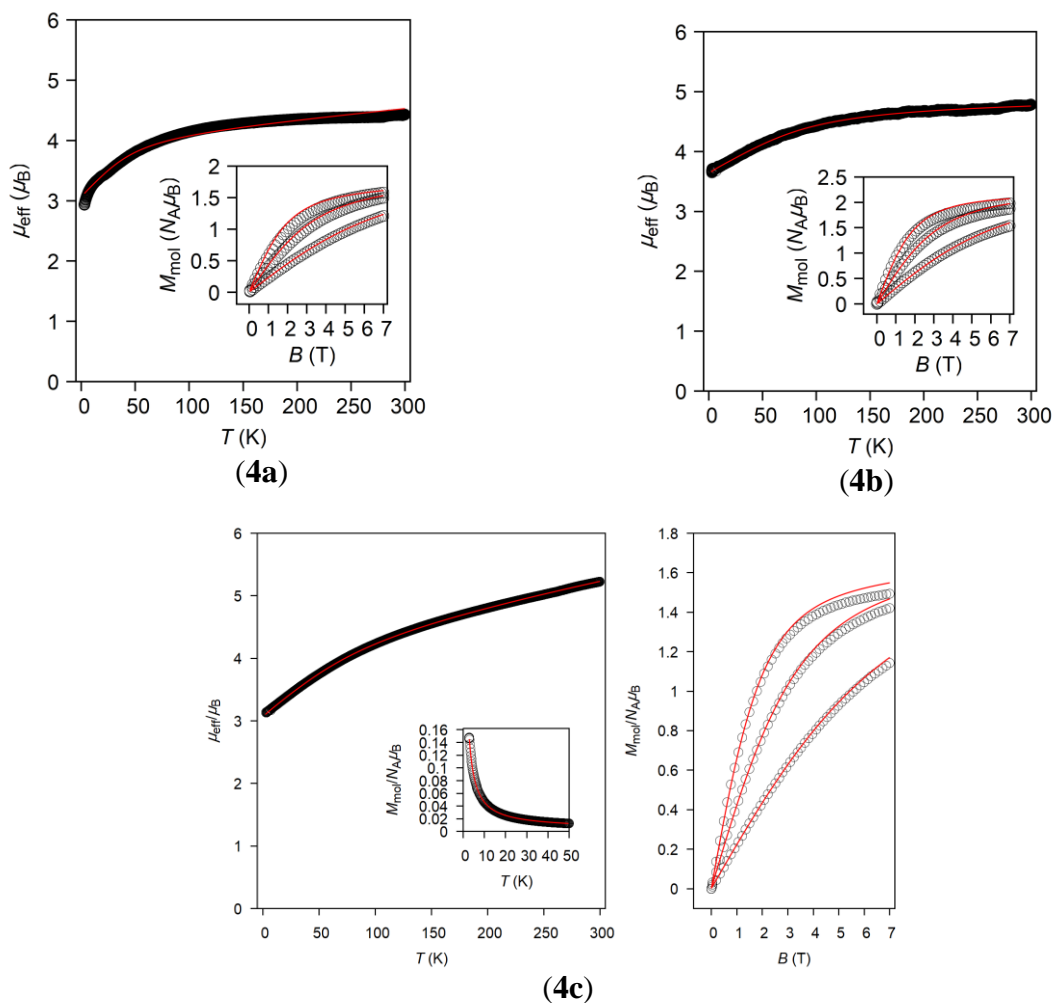*Figure 66: Static magnetic measurements of 4a, 4b and 4c under external magnetic field of 0.2 T. Black circles represent experimental data, red lines are fits.*

Table 8: ZFS parameters of 4a, 4b and 4b obtained from Spin Hamiltonian fitting

	D	*E/D*	g_{iso}
4a	-44.11	0.00	2.05
4b	75.02	0.33	2.43
4c	-80.23	0.00	2.05

6. Conclusions

In first step this thesis focused on synthesis of trigonal organic ligands suitable for coordination of Dy(III) and Co(II) atoms. In the next step, it was planned to grow single crystals of prepared coordination compounds and study them structurally and magnetically. In the final step selected samples were supposed to be deposited on various substrates. The first and third step was complicated by issues of preparation of Dy(III) coordination compounds and thermal deposition of Co(II).

In section 5.1 is discussed preparation of a series of Mannich type ligands and attempts to prepare coordination compounds of them with Dy(III) as an central atom. A series of different Mannich ligands were prepared with great potential for synthesis of the Dy(III) coordination compounds with coordination number lower than usual 8 or 9. Despite many attempts made, the isolation of pure and crystalline products were unsuccessful.

Previously, many magnetically interesting Dy(III) coordination compounds with the H_3tea ligand were reported, so in this work H_3tea was replaced by more sterically demanding ligand H_3tipa. However, the preparation of wide series of structurally different complexes was not successful, while extensive screening of reaction conditions led only to preparation of dimeric complex **1a**. **1a** was structurally and magnetically studied. The magnetic data were analyzed using approach combining fitting of experimental data and ab initio calculations. This helped to reveal weak antiferromagnetic exchange interaction between the Dy(III) atoms of the dimer. From the theoretical calculations the value of spin-reversal barrier $U_{eff} = 47.36$ cm^{-1} was obtained.

In section 5.2 it was possible to complete the series of coordination compounds with the trigonal ligand trenb reaching total amount of twelve coordination compounds. The series was extensively experimentally and computationally studied. The magnetic measurements revealed that studied complexes possess small or medium axial magnetic anisotropy ($|D| = 1.8 - 9.4$ cm^{-1}). Additionally, the four compounds from the series were studied by HFEPR mostly confirming the magnetization studies and the measurements were also complemented by theoretical CASSCF/NEVPT2 calculations. Repeated attempts for utilization of the members of this series for depositions showed that they are not suitable for wet depositions (low solubility) nor for thermal sublimation (high temperature of sublimation).

Section 5.3 describes series of the Co-based coordination compounds with the H_3tipa ligand. Six coordination compounds were prepared– three mononuclear, one trinuclear and two tetranuclear. The preparation of the tri- and tetranuclear complexes was complicated and required extensive screening of the reaction conditions supported by titration and by UV/VIS characterization. This series is magnetically interesting due to the formation of the magnetic exchange pathways involving the non-covalent interactions. In the case of the mononuclear complexes, the O–H···O hydrogen bonding contributed to formation of the supramolecular dimers. The BS-DFT calculations confirmed this exchange pathway to mediate weak antiferromagnetic interactions ($J_{CALC} = $ -1.7 to -1.5 cm^{-1}), which is in the excellent agreement with the results obtained from fitting of the magnetic data ($J_{exp} = $ -1.9 to -1.6 cm^{-1}). In the case of tetranuclear complexes, the magnetic exchange interaction is mediated between the peripheral Co(II) atoms via the O–Co(III)–O exchange pathway. Again, the BS-DFT calculations supported this hypothesis and the agreement between the calculated ($J_{CALC} = $ -0.6 cm^{-1} for **3e** and -1.3 cm^{-1} for **3f**) and experimentally obtained exchange coupling constants (J_{exp} = -0.4 cm^{-1} for **3e** and -2.2 cm^{-1} for **3f**) is excellent. AC susceptibility measurements were measured and analyzed for trinuclear Co(III)$_2$-Co(II) complex and it was revealed that this compound behaves as field-induced SIM with U_{eff} = 34.4 K.

From the magnetic point of view, the most perspective group of coordination compounds studied in this thesis are **4a**, **4b** and **4c**, discussed in section 5.4. These compounds are composed of the chains with alternating triacetylacetonato-Co(II) complex molecules and alkali cations (**Figure 66**) forming 1D chains. Li and Na salts have degenerate ground states, which should give a rise to large axial magnetic anisotropy. There is weak (Na, K salts) or even negligible (Li salt) magnetic exchange interaction between the molecules via exchange pathways involving alkali cations. The magnetic analysis of this series is very complicated, and it is still ongoing. Nevertheless, the obtained magnetization data corresponds with huge magnetic anisotropy.

7. References

1. Buschow, K. H. J., de Boer, F. R. *Physics of Magnetism and Magnetic Materials*. vol. 59 (World Scientific, 2003).

2. Lis, T. Preparation, structure, and magnetic properties of a dodecanuclear mixed-valence manganese carboxylate. *Acta Crystallogr. Sect. B Struct. Crystallogr. Cryst. Chem.* **36**, 2042–2046 (1980).

3. Hl-, N. I. H. G. *et al.* [Mn12012(02CR)16(H20)4]. 1804–1816 (1993).

4. Bogani, L. & Wernsdorfer, W. Molecular spintronics using single-molecule magnets. *Nanosci. Technol. A Collect. Rev. from Nat. Journals* 194–204 (2009) doi:10.1142/9789814287005_0020.

5. Barra, A. L., Debrunner, P., Gatteschi, D., Schulz, C. E. & Sessoli, R. Superparamagnetic-like behavior in an octanuclear iron cluster. *Europhys. Lett.* **35**, 133–138 (1996).

6. Yang, E.-C. *et al.* Cobalt single-molecule magnet. *J. Appl. Phys.* **91**, 7382 (2002).

7. Ishikawa, N., Sugita, M., Ishikawa, T., Koshihara, S. Y. & Kaizu, Y. Lanthanide double-decker complexes functioning as magnets at the single-molecular level. *J. Am. Chem. Soc.* **125**, 8694–8695 (2003).

8. Frost, J. M., Harriman, K. L. M. & Murugesu, M. The rise of 3-d single-ion magnets in molecular magnetism: towards materials from molecules? *Chem. Sci.* **7**, 2470–2491 (2016).

9. Bogani, L. & Wernsdorfer, W. Molecular spintronics using single-molecule magnets. *Nat. Mater.* **7**, 179–186 (2008).

10. Sessoli, R., Gatteschi, D., Caneschi, A. & Novak, M. A. Magnetic bistability in a metal-ion cluster. *Nature* **365**, 141–143 (1993).

11. Spree, L. *et al.* Robust Single Molecule Magnet Monolayers on Graphene and Graphite with Magnetic Hysteresis up to 28 K. *Adv. Funct. Mater.* **31**, 1–7 (2021).

12. Lenz, E. Über die Bestimmung der Richtung der durch elektodynamische Vertheilung erregten galvanischen Ströme. *Ann. der Phys. und Chemie* **107**, 483–494 (1834).

13. Boča, R. *Chémia koordinačných a organokovových zlúčenin*. (Nakladateľstvo STU, 2011).

14. Wernsdorfer, W. Classical and Quantum Magnetization Reversal Studied in Nanometer-Sized Particles and Clusters. in *Handbook of Advanced Magnetic Materials* 77–127 (Springer US). doi:10.1007/1-4020-7984-2_3.

15. Gatteschi, D., Sessoli, R. & Villain, J. *Molecular Nanomagnets*. (Oxford University Press, 2006). doi:10.1093/acprof:oso/9780198567530.001.0001.

16. Benelli, C. & Gatteschi, D. *Introduction to Molecular Magnetism*. (Wiley-VCH Verlag GmbH & Co. KGaA, 2015). doi:10.1002/9783527690541.

17. Borah, A. & Murugavel, R. Magnetic relaxation in single-ion magnets formed by less-studied lanthanide ions Ce(III), Nd(III), Gd(III), Ho(III), Tm(II/III) and Yb(III). *Coord. Chem. Rev.* **453**, 214288 (2022).

18. Herchel, Radovan; Tuček, J. ;Trávníček Z. *Střídavá susceptibilita a vysokoteplotní magnetická měření a jejich využití v chemii a fyzice*. (Palacký University, 2009).

19. Aronica, C. *et al.* A Nonanuclear Dysprosium(III)–Copper(II) Complex Exhibiting Single-Molecule Magnet Behavior with Very Slow Zero-Field Relaxation. *Angew. Chemie* **118**, 4775–4778 (2006).

20. Sokol, J. J., Hee, A. G. & Long, J. R. A cyano-bridged single-molecule magnet: Slow magnetic

relaxation in a trigonal prismatic MnMo6(CN)18 cluster. *J. Am. Chem. Soc.* **124**, 7656–7657 (2002).

21.	Nemec, I. *et al.* Magnetic anisotropy and field-induced slow relaxation of magnetization in tetracoordinate CoII compound [Co(CH3-im)2Cl2]. *Materials (Basel).* **10**, 1–14 (2017).

22.	Sessoli, R. *et al.* High-Spin Molecules: [Mn12O12(O2CR)16(H2O)4]. *J. Am. Chem. Soc.* **115**, 1804–1816 (1993).

23.	Chandrasekhar, V., Pandian, B. M., Vittal, J. J. & Clérac, R. Synthesis, structure, and magnetism of heterobimetallic trinuclear complexes {[L2Co2Ln][X]} [Ln = Eu, X = Cl; Ln = Tb, Dy, Ho, X = NO3; LH3 = (S)P[N(Me)N=CH-C6H 3-2-OH-3-OMe]3]: A 3d-4f family of single-molecule magnets. *Inorg. Chem.* **48**, 1148–1157 (2009).

24.	Chakraborty, A., Acharya, J. & Chandrasekhar, V. Ferrocene-Supported Compartmental Ligands for the Assembly of 3d/4f Complexes. *ACS Omega* (2020) doi:10.1021/acsomega.0c00654.

25.	Goswami, S., Mondal, A. K. & Konar, S. Nanoscopic molecular magnets. *Inorg. Chem. Front.* **2**, 687–712 (2015).

26.	Karasawa, S., Zhou, G., Morikawa, H. & Koga, N. Magnetic Properties of Tetrakis[4-(α - diazobenzyl)-pyridine]bis(thiocyanato-N)cobalt(II) in Frozen Solution after Irradiation. Formation of a Single-Molecule Magnet in Frozen Solution. *J. Am. Chem. Soc.* **125**, 13676–13677 (2003).

27.	Freedman, D. E. *et al.* Slow magnetic relaxation in a high-spin iron(II) complex. *J. Am. Chem. Soc.* **132**, 1224–1225 (2010).

28.	Colacio, E. *et al.* Family of Carboxylate- and Nitrate-diphenoxo Triply Bridged Dinuclear Ni. *Inorg. Chem.* **51**, 5857–5868 (2012).

29.	Li, H. *et al.* Remarkable Ln III 3 Fe III 2 clusters with magnetocaloric effect and slow magnetic relaxation. *Dalt. Trans.* **44**, 468–471 (2015).

30.	Papatriantafyllopoulou, C., Wernsdorfer, W., Abboud, K. A. & Christou, G. Mn 21 Dy Cluster with a Record Magnetization Reversal Barrier for a Mixed 3d/4f Single-Molecule Magnet. *Inorg. Chem.* **50**, 421–423 (2011).

31.	Chandrasekhar, V., Pandian, B. M., Azhakar, R., Vittal, J. J. & Clérac, R. Linear trinuclear mixed-metal CoII-GdIII-Co II single-molecule magnet: [L2Co2Gd][NO 3]·2CHCl3 (LH3 = (S)P[N(Me)N=CH-C 6H3-2-OH-3-OMe]3). *Inorg. Chem.* **46**, 5140–5142 (2007).

32.	Chandrasekhar, V. *et al.* Cyclo- and Carbophosphazene-Supported Ligands for the Assembly of Heterometallic (Cu 2+ /Ca 2+ , Cu 2+ /Dy 3+ , Cu 2+ /Tb 3+) Complexes: Synthesis, Structure, and Magnetism . *Inorg. Chem.* **51**, 2031–2038 (2012).

33.	Chandrasekhar, V., Dey, A., Das, S., Rouzières, M. & Clérac, R. Syntheses, structures, and magnetic properties of a family of heterometallic heptanuclear [Cu5Ln2] (Ln = Y(III), Lu(III), Dy(III), Ho(III), Er(III), and Yb(III)) complexes: Observation of SMM behavior for the Dy(III) and Ho(III) analogues. *Inorg. Chem.* **52**, 2588–2598 (2013).

34.	Chandrasekhar, V. *et al.* Trinuclear heterobimetallic Ni2Ln complexes [L 2Ni2Ln][ClO4] (Ln = La, Ce, Pr, Nd, Sm, Eu, Gd, Tb, Dy, Ho, and Er; LH3 = (S)P[N(Me)N=CH-C6H 3-2-OH-3-OMe]3): From simple paramagnetic complexes to single-molecule magnet behavior. *Inorg. Chem.* **47**, 4918–4929 (2008).

35.	Zadrozny, J. M. & Long, J. R. Slow magnetic relaxation at zero field in the tetrahedral complex [Co(SPh) 4] 2-. *J. Am. Chem. Soc.* **133**, 20732–20734 (2011).

36. Zadrozny, J. M., Telser, J. & Long, J. R. Slow magnetic relaxation in the tetrahedral cobalt(II) complexes [Co(EPh)4]2- (EO, S, Se). *Polyhedron* **64**, 209–217 (2013).

37. Mossin, S. *et al.* A Mononuclear Fe(III) Single Molecule Magnet with a 3/2↔5/2 Spin Crossover. *J. Am. Chem. Soc.* **134**, 13651–13661 (2012).

38. Zadrozny, J. M. *et al.* Magnetic blocking in a linear iron(I) complex. *Nat. Chem.* **5**, 577–581 (2013).

39. Fataftah, M. S., Zadrozny, J. M., Rogers, D. M. & Freedman, D. E. A mononuclear transition metal single-molecule magnet in a nuclear spin-free ligand environment. *Inorg. Chem.* **53**, 10716–10721 (2014).

40. Varzatskii, O. A. *et al.* Chloride ion-aided self-assembly of pseudoclathrochelate metal tris-pyrazoloximates. *Inorg. Chem.* **53**, 3062–3071 (2014).

41. Novikov, V. V. *et al.* A Trigonal Prismatic Mononuclear Cobalt(II) Complex Showing Single-Molecule Magnet Behavior. *J. Am. Chem. Soc.* **137**, 9792–9795 (2015).

42. Carl, E., Demeshko, S., Meyer, F. & Stalke, D. Triimidosulfonates as Acute Bite-Angle Chelates: Slow Relaxation of the Magnetization in Zero Field and Hysteresis Loop of a CoII Complex. *Chem. - A Eur. J.* **21**, 10109–10115 (2015).

43. Shao, F. *et al.* Tuning the Ising-type anisotropy in trigonal bipyramidal Co(II) complexes. *Chem. Commun.* **51**, 16475–16478 (2015).

44. Rechkemmer, Y. *et al.* A four-coordinate cobalt(II) single-ion magnet with coercivity and a very high energy barrier. *Nat. Commun.* **7**, 1–8 (2016).

45. Sottini, S. *et al.* Magnetic Anisotropy of Tetrahedral CoII Single-Ion Magnets: Solid-State Effects. *Inorg. Chem.* **55**, 9537–9548 (2016).

46. Zhu, Y. Y. *et al.* Zero-field slow magnetic relaxation from single Co(ii) ion: A transition metal single-molecule magnet with high anisotropy barrier. *Chem. Sci.* **4**, 1802–1806 (2013).

47. Bradley, D. C., Ghotra, J. S. & Hart, F. A. Three-co-ordination in Lanthanide Chemistry : *J. Chem. Soc., Chem. Commun.* 349–350 (1972).

48. Zhang, P. *et al.* Equatorially coordinated lanthanide single ion magnets. *J. Am. Chem. Soc.* **136**, 4484–4487 (2014).

49. Hänninen, M. M. *et al.* Two C 3 -Symmetric Dy 3 III Complexes with Triple Di-μ-methoxo-μ-phenoxo Bridges, Magnetic Ground State, and Single-Molecule Magnetic Behavior. *Chem. - A Eur. J.* **20**, 8410–8420 (2014).

50. Mylonas-Margaritis, I. *et al.* Using the Singly Deprotonated Triethanolamine to Prepare Dinuclear Lanthanide(III) Complexes: Synthesis, Structural Characterization and Magnetic Studies. *Magnetochemistry* **3**, 5 (2017).

51. Koroteev, P. S. *et al.* Mononuclear and binuclear lanthanide acetates with chelating and bridging triethanolamine ligands. *Polyhedron* **154**, 54–64 (2018).

52. Li, X., Liu, Y., Chi, X., Zhu, G. & Gao, F. Synthesis, Structures, and Magnetic Properties of Zigzag Tetranuclear Lanthanide Complexes. *Zeitschrift für Anorg. und Allg. Chemie* **646**, 1292–1296 (2020).

53. Langley, S. K., Moubaraki, B., Forsyth, C. M., Gass, I. A. & Murray, K. S. Structure and magnetism of new lanthanide 6-wheel compounds utilizing triethanolamine as a stabilizing ligand. *Dalt. Trans.* **39**, 1705–1708 (2010).

54. Goura, J. *et al.* Heterometallic Zn 3 Ln 3 Ensembles Containing (μ 6 -CO 3) Ligand and Triangular Disposition of Ln 3+ ions: Analysis of Single-Molecule Toroic (SMT) and Single-

Molecule Magnet (SMM) Behavior. *Chem. - A Eur. J.* **23**, 16621–16636 (2017).

55. Chen, Y. C. *et al.* Symmetry-Supported Magnetic Blocking at 20 K in Pentagonal Bipyramidal Dy(III) Single-Ion Magnets. *J. Am. Chem. Soc.* **138**, 2829–2837 (2016).

56. Takamatsu, S., Ishikawa, T., Koshihara, S. Y. & Ishikawa, N. Significant increase of the barrier energy for magnetization reversal of a single-4f-ionic single-molecule magnet by a longitudinal contraction of the coordination space. *Inorg. Chem.* **46**, 7250–7252 (2007).

57. Goodwin, C. A. P., Ortu, F., Reta, D., Chilton, N. F. & Mills, D. P. Molecular magnetic hysteresis at 60 kelvin in dysprosocenium. *Nature* **548**, 439–442 (2017).

58. Guo, F. S. *et al.* A Dysprosium Metallocene Single-Molecule Magnet Functioning at the Axial Limit. *Angew. Chemie - Int. Ed.* **56**, 11445–11449 (2017).

59. Guo, F. S. *et al.* Magnetic hysteresis up to 80 kelvin in a dysprosium metallocene single-molecule magnet. *Science (80-.).* **362**, 1400–1403 (2018).

60. Kyatskaya, S. *et al.* Anchoring of rare-earth-based single-molecule magnets on single-walled carbon nanotubes. *J. Am. Chem. Soc.* **131**, 15143–15151 (2009).

61. Lopes, M. *et al.* Surface-enhanced raman signal for terbium single-molecule magnets grafted on graphene. *ACS Nano* **4**, 7531–7537 (2010).

62. Zhu, X., Hale, A., Christou, G. & Hebard, A. F. Electronegative ligands enhance charge transfer to Mn12 single-molecule magnets deposited on graphene. *J. Appl. Phys.* **127**, (2020).

63. Cimatti, I. *et al.* Vanadyl phthalocyanines on graphene/SiC(0001): Toward a hybrid architecture for molecular spin qubits. *Nanoscale Horizons* **4**, 1202–1210 (2019).

64. Marocchi, S. *et al.* Relay-Like Exchange Mechanism through a Spin Radical between TbPc2 Molecules and Graphene/Ni(111) Substrates. *ACS Nano* **10**, 9353–9360 (2016).

65. Mannini, M. *et al.* Quantum tunnelling of the magnetization in a monolayer of oriented single-molecule magnets. *Nature* **468**, 417–421 (2010).

66. Wäckerlin, C. *et al.* Giant Hysteresis of Single-Molecule Magnets Adsorbed on a Nonmagnetic Insulator. *Adv. Mater.* **28**, 5195–5199 (2016).

67. Margheriti, L. *et al.* X-Ray Detected Magnetic Hysteresis of Thermally Evaporated Terbium Double-Decker Oriented Films. *Adv. Mater.* **22**, 5488–5493 (2010).

68. Stepanow, S. *et al.* Spin and Orbital Magnetic Moment Anisotropies of Monodispersed Bis(Phthalocyaninato)Terbium on a Copper Surface. *J. Am. Chem. Soc.* **132**, 11900–11901 (2010).

69. Mannini, M. *et al.* X-ray magnetic circular dichroism picks out single-molecule magnets suitable for nanodevices. *Adv. Mater.* **21**, 167–171 (2009).

70. Cervetti, C. *et al.* The classical and quantum dynamics of molecular spins on graphene. *Nat. Mater.* **15**, 164–168 (2016).

71. Paschke, F., Erler, P., Enenkel, V., Gragnaniello, L. & Fonin, M. Bulk-Like Magnetic Signature of Individual Fe 4 H Molecular Magnets on Graphene. *ACS Nano* **13**, 780–785 (2019).

72. Kahle, S. *et al.* The Quantum Magnetism of Individual Manganese-12-Acetate Molecular Magnets Anchored at Surfaces. *Nano Lett.* **12**, 518–521 (2012).

73. Ciccullo, F. *et al.* Interfacing a Potential Purely Organic Molecular Quantum Bit with a Real-Life Surface. *ACS Appl. Mater. Interfaces* **11**, 1571–1578 (2019).

74. Ciccullo, F. *et al.* Thin film properties and stability of a potential molecular quantum bit based on copper(ii). *J. Mater. Chem. C* **6**, 8028–8034 (2018).

75.   Hrubý, J. *et al.* Co(ii)-Based single-ion magnets with 1,1'-ferrocenediyl-bis(diphenylphosphine) metalloligands. *Dalt. Trans.* **49**, 11697–11707 (2020).

76.   Addison, A. W., Rao, T. N., Reedijk, J., Rijn, J. van & Verschoor, G. C. Synthesis, Structure, and Spectroscopic Properties of Copper(II) Compounds containing Nitrogen-Sulphur Donor Ligands. *J. Chem. Soc. Dalt. Trans* **7**, 1349–1356 (1984).

77.   M. Llunell, D. Casanova, J. Ciera, P. Alemany, S. A. SHAPE, Version 2.1. (2013).

78.   Hrubý, J. High Frequency Electron Spin Resonance Spectroscopy. *PhD thesis* (Brno University of Technology, 2021).

79.   Hrubý, J. *et al.* Deposition of Tetracoordinate Co(II) Complex with Chalcone Ligands on Graphene. *Molecules* **25**, 1–17 (2020).

80.   Hrubý, J. *et al.* A graphene-based hybrid material with quantum bits prepared by the double Langmuir–Schaefer method. *RSC Adv.* **9**, 24066–24073 (2019).

81.   Marie, L. S. *et al.* Nanostructured graphene for nanoscale electron paramagnetic resonance spectroscopy. *J. Phys. Mater.* **3**, 014013 (2020).

82.   Sojka, A. *et al.* Sample Holders for Sub-THz Electron Spin Resonance Spectroscopy. *IEEE Trans. Instrum. Meas.* **71**, 1–12 (2022).

83.   Stoll, S. & Schweiger, A. EasySpin, a comprehensive software package for spectral simulation and analysis in EPR. *J. Magn. Reson.* **178**, 42–55 (2006).

84.   Ungur, L., Van den Heuvel, W. & Chibotaru, L. F. Ab initio investigation of the non-collinear magnetic structure and the lowest magnetic excitations in dysprosium triangles. *New J. Chem.* **33**, 1224 (2009).

85.   Chibotaru, L. F., Ungur, L. & Soncini, A. The Origin of Nonmagnetic Kramers Doublets in the Ground State of Dysprosium Triangles: Evidence for a Toroidal Magnetic Moment. *Angew. Chemie Int. Ed.* **47**, 4126–4129 (2008).

86.   Chibotaru, L. F. *et al.* Structure, Magnetism, and Theoretical Study of a Mixed-Valence Co II 3 Co III 4 Heptanuclear Wheel: Lack of SMM Behavior despite Negative Magnetic Anisotropy. *J. Am. Chem. Soc.* **130**, 12445–12455 (2008).

87.   Neese, F., Wennmohs, F., Hansen, A. & Becker, U. Efficient, approximate and parallel Hartree-Fock and hybrid DFT calculations. A 'chain-of-spheres' algorithm for the Hartree-Fock exchange. *Chem. Phys.* **356**, 98–109 (2009).

88.   Neese, F. Software update: the ORCA program system, version 4.0. *Wiley Interdiscip. Rev. Comput. Mol. Sci.* **8**, 1–6 (2018).

89.   Anatasov, M.; Ganyushin, D.;Sivalingam, K. and Neese, F. *Molecular Electronic Structures of Transition Metal Complexes II*. vol. 143 (Springer Berlin Heidelberg, 2012).

90.   Fairley, N. *et al.* Systematic and collaborative approach to problem solving using X-ray photoelectron spectroscopy. *Appl. Surf. Sci. Adv.* **5**, 100112 (2021).

91.   Bazarnik, M., Brede, J., Decker, R. & Wiesendanger, R. Tailoring molecular self-assembly of magnetic phthalocyanine molecules on fe- and co-intercalated graphene. *ACS Nano* **7**, 11341–11349 (2013).

92.   Danieli, C. *et al.* A novel class of tetrairon(III) single-molecule magnets with graphene-binding groups. *Polyhedron* **28**, 2029–2035 (2009).

93.   Lisi, S. *et al.* Graphene-induced magnetic anisotropy of a two-dimensional iron phthalocyanine network. *J. Phys. Chem. Lett.* **6**, 1690–1695 (2015).

94. Jiang, H., Xie, Y. S., Zhou, Z. Y., Xu, X. L. & Liu, Q. L. Syntheses, structures and characterization of cobalt(II) and cobalt(III) complexes with N-benzylated polyamines and a terminal azido ligand. *J. Coord. Chem.* **56**, 825–832 (2003).

95. Xie, Y. S. *et al.* Syntheses and characterization of copper(II) and cobalt(II) complexes with tris[2-(benzylamino)ethyl]amine. *Collect. Czechoslov. Chem. Commun.* **67**, 1647–1657 (2002).

96. Havlíček, L. Magnetické vlastnosti a struktura pentakoordinovaných sloučenin Co(II) s tri- a tetradentátními ligandy odvozenými od alifatických triaminů. *Univerzita Palackého v Olomouci* (2018).

97. Mannini, M. *et al.* Magnetic memory of a single-molecule quantum magnet wired to a gold surface. *Nat. Mater.* **8**, 194–197 (2009).

98. Cornia, A. *et al.* Direct observation of single-molecule magnets organized on gold surfaces. *Angew. Chemie - Int. Ed.* **42**, 1645–1648 (2003).

99. Holmberg, R. J. *et al.* Hybrid nanomaterials: Anchoring magnetic molecules on naked gold nanocrystals. *Inorg. Chem.* **52**, 14411–14418 (2013).

100. Cornia, A., Mannini, M., Sainctavit, P. & Sessoli, R. Chemical strategies and characterization tools for the organization of single molecule magnets on surfaces. *Chem. Soc. Rev.* **40**, 3076–3091 (2011).

101. Desiraju, G. & Steiner, T. *The Weak Hydrogen Bond*. (Oxford University Press, 2001). doi:10.1093/acprof:oso/9780198509707.001.0001.

102. Gomez-Coca, S., Cremades, E., Aliaga-Alcalde, N. & Ruiz, E. Mononuclear Single-Molecule Magnets: Tailoring the Magnetic Anisotropy of First-Row Transition-Metal Complexes. *J. Am. Chem. Soc.* **135**, 7010–7018 (2013).

103. Mazilu, M., De Luca, A. C., Riches, A., Herrington, C. S. & Dholakia, K. Optimal algorithm for fluorescence suppression of modulated Raman spectroscopy. *Opt. Express* **18**, 11382 (2010).

104. Larkin, P. *Infrared and Raman Spectroscopy*. (Elsevier, 2011).

105. J. F. Moulder, W. F. Stickle, P. E. S. and K. D. B. *Handbook of X-Ray Photoelectron Spectroscopy*. (J. F. Moulder, W. F. Stickle, P. E. Sobol and K. D. Bomben, Eden Prairie, Minnesota: Physical Electronics Division, Perkin-Elmer Corporation, 1992).

106. Poneti, G. *et al.* Magnetic and Spectroscopic Investigation of Thermally and Optically Driven Valence Tautomerism in Thioether-Bridged Dinuclear Cobalt–Dioxolene Complexes. *Inorg. Chem.* **52**, 11798–11805 (2013).

107. Solomon, E. I., Basumallick, L., Chen, P. & Kennepohl, P. Variable energy photoelectron spectroscopy: electronic structure and electronic relaxation. *Coord. Chem. Rev.* **249**, 229–253 (2005).

108. Lange, S. C., van Andel, E., Smulders, M. M. J. & Zuilhof, H. Efficient and Tunable Three-Dimensional Functionalization of Fully Zwitterionic Antifouling Surface Coatings. *Langmuir* **32**, 10199–10205 (2016).

109. Zhan, H. J. *et al.* Microwave Irradiation Synthesized Cobalt-Loaded Nitrogen-Doped Active Carbon as an Efficient Catalyst for Selective Oxidation of Ethylbenzene. *IOP Conf. Ser. Mater. Sci. Eng.* **562**, 012004 (2019).

110. Goldmann, A. S. *et al.* Surface Modification of Poly(divinylbenzene) Microspheres via Thiol−Ene Chemistry and Alkyne−Azide Click Reactions. *Macromolecules* **42**, 3707–3714 (2009).

111. Noodleman, L. Valence bond description of antiferromagnetic coupling in transition metal

dimers. *J. Chem. Phys.* **74**, 5737–5743 (1981).

112. Noodleman, L. & Davidson, E. R. Ligand spin polarization and antiferromagnetic coupling in transition metal dimers. *Chem. Phys.* **109**, 131–143 (1986).

113. Bencini, A. & Gatteschi, D. X.alpha.-SW calculations of the electronic structure and magnetic properties of weakly coupled transition-metal clusters. The [Cu2Cl6]2- dimers. *J. Am. Chem. Soc.* **108**, 5763–5771 (1986).

114. Yamaguchi, K., Takahara, Y. & Fueno, T. Ab-Initio Molecular Orbital Studies of Structure and Reactivity of Transition Metal-OXO Compounds. in *Applied Quantum Chemistry* 155–184 (Springer Netherlands, 1986). doi:10.1007/978-94-009-4746-7_11.

115. Osborne, S. J. *et al.* Thermochromism and switchable paramagnetism of cobalt(<scp>ii</scp>) in thiocyanate ionic liquids. *Dalt. Trans.* **44**, 11286–11289 (2015).

116. Zoufalý, P., Čižmár, E., Kuchár, J. & Herchel, R. The structural and magnetic properties of FeII and CoII complexes with 2-(furan-2-yl)-5-pyridin-2-yl-1,3,4-oxadiazole. *Molecules* **25**, 1–18 (2020).

117. Herchel, R., Zoufalý, P. & Nemec, I. The effect of the second coordination sphere on the magnetism of [Ln(NO 3) 3 (H 2 O) 3]·(18-crown-6) (Ln = Dy and Er). *RSC Adv.* **9**, 569–575 (2019).

118. Harrah, B. No Title. *Microscope* **13**, 295 (1962).

119. Wei, Z., Han, H., Filatov, A. S. & Dikarev, E. V. Changing the bridging connectivity pattern within a heterometallic assembly: design of single-source precursors with discrete molecular structures. *Chem. Sci.* **5**, 813–818 (2014).

120. Li, X., Musie, G. & Powell, D. R. Sodium tris(acetylacetonato-κ 2 O , O ')cobalt(II). *Acta Crystallogr. Sect. E Struct. Reports Online* **59**, m717–m718 (2003).

121. Shin, S. H., Yun, S. H. & Moon, S. H. A review of current developments in non-aqueous redox flow batteries: Characterization of their membranes for design perspective. *RSC Adv.* **3**, 9095–9116 (2013).

122. Matos, C. R. M. O. *et al.* Field-induced single-ion magnets exhibiting tri-axial anisotropy in a 1D Co(<scp>ii</scp>) coordination polymer with a rigid ligand 4,4'-(buta-1,3-diyne-1,4-diyl)dibenzoate. *Dalt. Trans.* **50**, 15003–15014 (2021).

123. Świtlicka, A. *et al.* Field-induced slow magnetic relaxation in pseudooctahedral cobalt(<scp>ii</scp>) complexes with positive axial and large rhombic anisotropy. *Dalt. Trans.* **48**, 1404–1417 (2019).

124. Nemec, I., Herchel, R. & Trávníček, Z. Two polymorphic Co(<scp>ii</scp>) field-induced single-ion magnets with enormous angular distortion from the ideal octahedron. *Dalt. Trans.* **47**, 1614–1623 (2018).

125. Zoufalý, P., Kliuikov, A., Čižmár, E., Císařová, I. & Herchel, R. Cis and Trans Isomers of Fe(II) and Co(II) Complexes with Oxadiazole Derivatives - Structural and Magnetic Properties. *Eur. J. Inorg. Chem.* **2021**, 1190–1199 (2021).

126. Drahoš, B., Šalitroš, I., Císařová, I. & Herchel, R. A multifunctional magnetic material based on a solid solution of Fe(<scp>ii</scp>)/Co(<scp>ii</scp>) complexes with a macrocyclic cyclam-based ligand. *Dalt. Trans.* **50**, 11147–11157 (2021).

127. Ghosh, S. *et al.* Reversible Spin-State Switching and Tuning of Nuclearity and Dimensionality via Nonlinear Pseudohalides in Cobalt(II) Complexes. *Inorg. Chem.* **59**, 17638–17649 (2020).

128. Boča, R. MIF with FIT Module. (2019).

8. Author Publications and Other Outputs

Publications

- 2022 – L. Havlíček, R. Herchel, I. Nemec, P. Neugebauer. Weak antiferromagnetic interaction in Cu(II) complex with semi-coordination exchange pathway, *Polyhedron*, 223, 2022
- 2022 – X. Zhang, J. Kastyl, M. C. Luna, L. Havlíček, M. Vondra, V. Brummer, K. Sukačová, S. Y. Teng, P. Neugebauer. Microalgae-derived nanoporous biochar for ammonia removal in sustainable wastewater treatment, *Journal of Environmental Chemical Engineering*, 10, 2022

Oral contribution

- 2018 – PETER Summer School, Brno, Czech Republic
- 2019 – 12th European School on Molecular Nanoscience and 7th Workshop on 2D Materials, Elche, Spain

Posters

- 2018 – ICN+T, Brno, Czech Republic
- 2018 – PETER Summer School, Brno, Czech Republic
- 2021 –ICMM 17th International Conference on Molecule Based Magnets, online

Supervision

- 2019 - CEITEC Student Talent supervision of Vojtěch Richard Krejsa (2nd place), Brno, Czech Republic

Grants

- 2018-2019 - VUT Specific research
- 2020-2021 - VUT Specific research – publication
- 2019-2021 – member of INTER-EXCELLENCE LTAUSA19060

Teaching activities

- September-December 2019 - Teaching Seminar of General chemistry (prof. Jiří Pinkas at MU, Brno, Czech Republic)
- September-December 2020 – Teaching Chemical Synthesis practicum (Dr. Slávka Janků at MU, Brno, Czech Republic)
- 2019 – presentation for Diploma Seminar (prof. Jiří Pinkas at MU, Brno, Czech Republic)

Internships

- 2019 – one month in a group of prof. Song Gao, Beijing, China
- 2019 – two weeks in a group of prof. Nikodem Kuźnik, Gliwice, Poland
- 2021 – one week in a laboratory of Assoc. prof. Ivan Šalitroš, Bratislava, Slovakia
- 2021 – one month in a group of prof. Paola Barbara, Washington DC, USA

Voluntary activities

- 2018, 2019 – Researcher's Night, CEITEC BUT, Brno, Czech Republic
- 2019 – 2021 Open days and school excursions at CEITEC BUT, Brno, Czech Republic

- 2019 – 120 years of BUT anniversary, Brno, Czech Republic

Appendix

Crystal structure

	1a
Space group	P 2$_1$/n
a[Å]	8.64752(2)
b[Å]	19.6538(2)
c[Å]	11.90840(13)
α[°]	90
β[°]	91.7139(11)
γ[°]	90
V[Å^3]	2023.01
T[K]	90
R	2.15

	2b
Space group	Pbca
a[Å]	14.7621(7)
b[Å]	15.4048(8)
c[Å]	25.3007(15)
α[°]	90
β[°]	90
γ[°]	90
V[Å^3]	5753.56
T[K]	100.15
R	6.58

	3a	**3b**	**3c**	**3d**	**3e**	**3f**
Space group	P 2$_1$/c	P 2$_1$/c	P 2$_1$/n	P 2$_1$/c	P 2$_1$/c	P 2$_1$/n
a[Å]	8.805(17)	8.86887(11)	9.6565(2)	17.4966(5)	15.6673(6)	20.0822(5)
b[Å]	10.75(2)	10.85365(12)	10.9025(2)	16.4566(4)	13.2121(5)	16.3140(5)
c[Å]	16.22(3)	16.3288(2)	14.7404(3)	13.5334(3)	13.7989(5)	10.9041(3)
α[°]	90	90	90	90	90	89.970(3)
β[°]	104.78(3)	104.2983(13)	104.238(2)	90.755(2)	114.291(5)	98.734(4)
γ[°]	16.22(3)	90	90	90	90	90.011(3)
V[Å^3]	1484.49	1523.11	1504.2	3896.4	2603.47	1772.72
T[K]	100.15	100.15	283	100.15	100.15	

R	5.86	2.3	4.42	5.2	4.69	4.1

Table 12: Crystallographic data of compounds 4a, 4b and 4c

	4a	**4b**	**4c**
Space group	R3c	R3c	Pna2$_1$
a[Å]	16.2550(3)	16.33410(10)	13.2035(2)
b[Å]	15.2550(3)	16.33410(10)	9.6337(2)
c[Å]	10.9427(2)	11.90167(10)	14.4677(3)
α[°]	90	90	90
β[°]	90	90	90
γ[°]	120	120	90
V[Å^3]	2503.97	2749.98	1840.27
T[K]	100.15	2.99	100.15
R	5.86	2.3	6.57
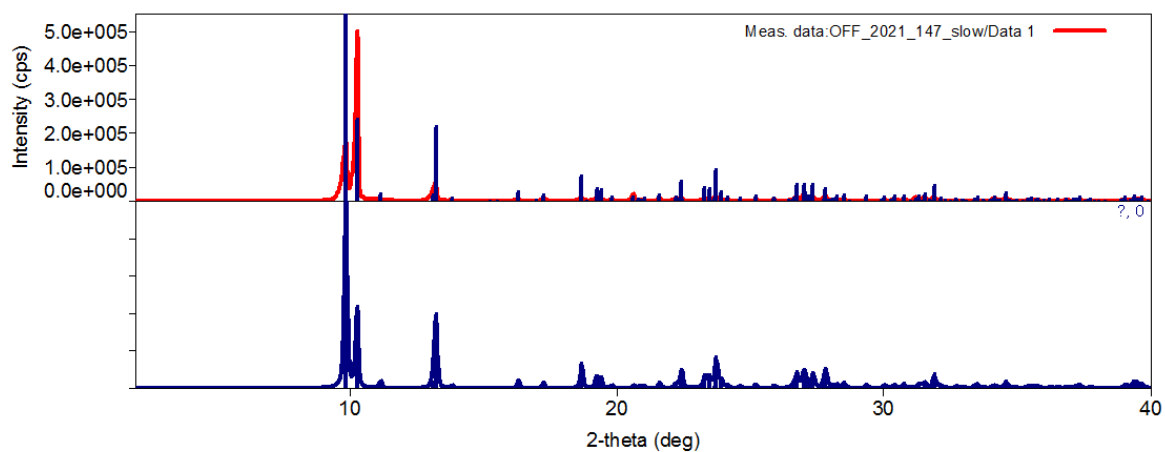
(3a)
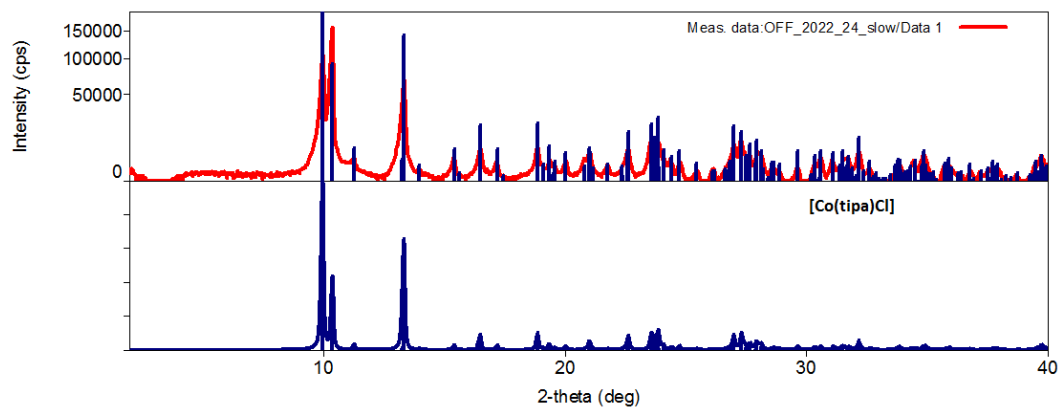
(3b)
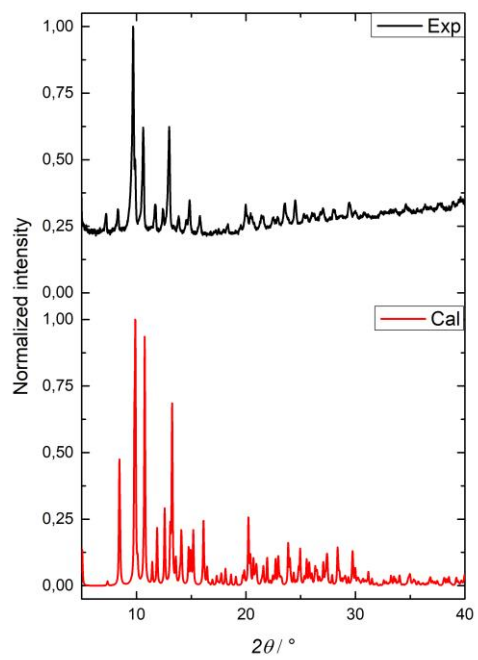
(3d)
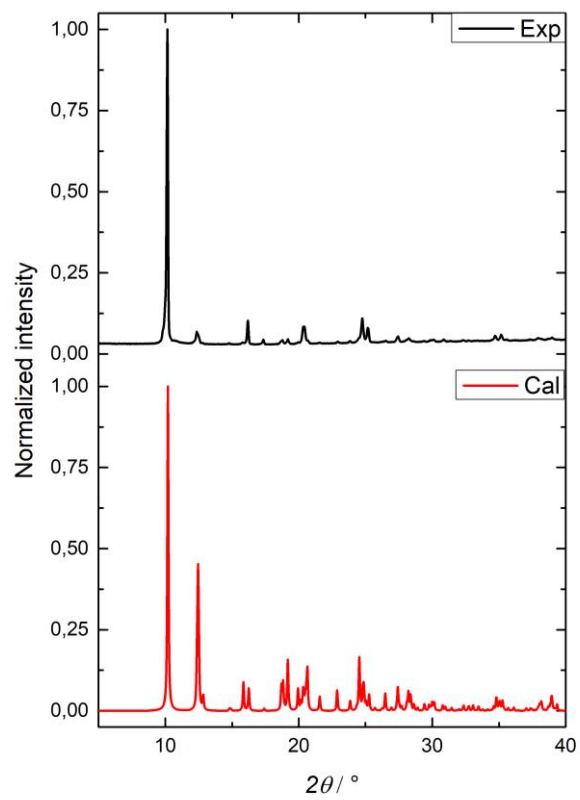
(3c)
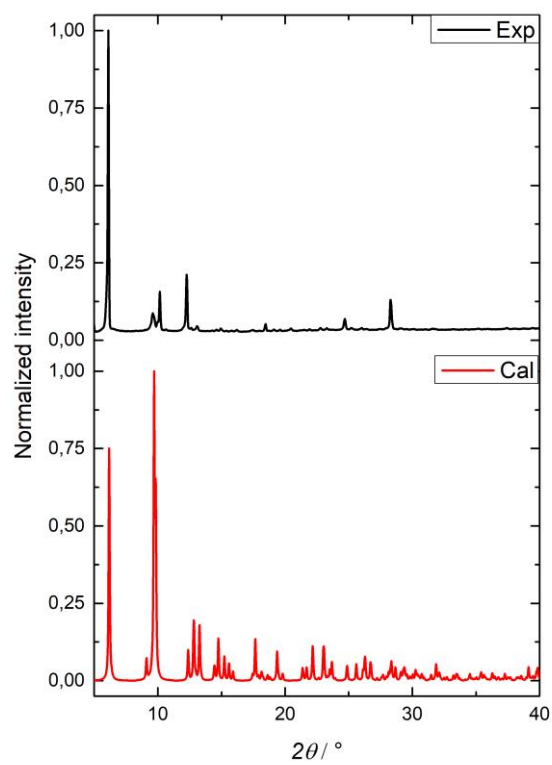
(3e)

*Figure 67: XRPD measurements for **3a**, **3b**, **3c**, **3d** and **3e***

Theoretical calculations

(3a_1)   (3a_2)   (3a_3)

(3b_1)   (3b_2)   (3b_3)
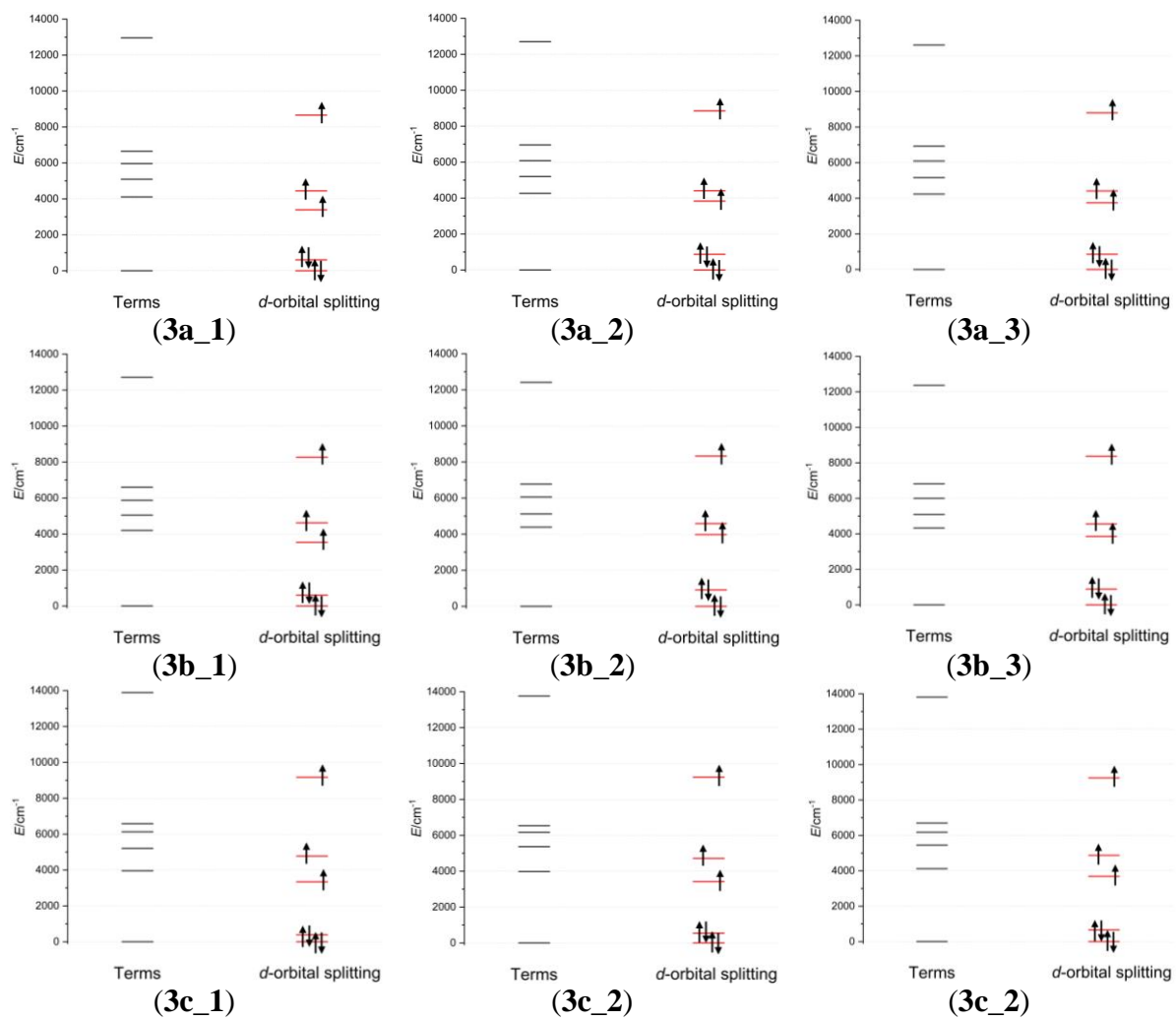
(3c_1)   (3c_2)   (3c_2)

*Figure 68: Terms and d-orbitals splitting of compounds **3a**, **3b** and **3c** considering three different crystal structures.*